Numerical Simulation of Wind – Induced Dispersion of Emissions From Rooftop Stacks

Xiaoguang Wang

A Thesis

in

The Department

of

Building, Civil & Environmental Engineering

Presented in Partial Fulfillment of the Requirements
for the Degree of Master of Applied Science (Building Engineering) at
Concordia University
Montreal, Quebec, Canada

Your file Votre référence
ISBN: 0-494-14243-X
Our file Notre référence
ISBN: 0-494-14243-X

ABSTRACT

Numerical Simulation of Wind – Induced Dispersion of Emissions From Rooftop Stacks

Xiaoguang Wang

The precise prediction of plume concentration distribution on or near buildings is very important for building engineers to design proper exhaust stacks and set proper air intakes to avoid adverse air quality impacts. The present study simulates the dispersion of emissions from stacks in the neutrally stable atmospheric boundary layer (ABL) by FLUENT 6.1, a commercial computational fluid dynamics (CFD) code. Three case studies have been conducted. The first case involves a simulation of plume dispersion from one isolated stack. The second case is concerned with a simulation of plume dispersion from a flush stack located at the roof center of a cubic building. The third case involves a simulation of plume dispersion from a short stack located on the rooftop of a rectangular building with some rooftop structures. Numerical results are compared with some empirical formulae, such as the Gaussian model and ASHRAE model, and validated with some experimental data. The effects of the momentum ratio, the stack height, and the turbulent characteristics caused by the building on the plume behavior are discussed. Some numerical parametric studies have been carried out.

The steady state condition is applied to calculate the mean concentration. Standard $k-\varepsilon$ model, realizable $k-\varepsilon$ model and Reynolds stress model (RSM) are used to close the governing equations. Wall functions and enhanced wall treatment are

used to treat flow field close to the wall. For one isolated stack, numerical simulation agrees well with the Gaussian model. For more complicated cases of emissions from a stack over or on the building roof, the present numerical simulation can predict the pollutant distribution along the plume centerline compared to the experimental data. However, it underestimates the plume spread in the lateral and vertical direction. The reason is the isotropic numerical models used in the present study.

The present study shows the homogenous profiles of velocity and dissipation rate (ε) in the ABL can be simulated by FLUENT 6.1 using an appropriate boundary condition for the turbulent kinetic energy (k). However, the homogenous profile of k could not be kept throughout the whole computational domain. This error could be decreased for cases with dominant turbulence caused by buildings. Previous works showed the turbulent Schmidt number (Sc_t) should take different values to fit the experimental data for different cases, but there has been no parametric study about this number. The effect of Sc_t on the pollutant distribution is demonstrated in the present study.

Future studies are required to solve the inhomogeneous k problem in FLUENT and accurately simulate the turbulent concentration flux with the assumption of the anisotropic diffusivity coefficients.

ACKNOWLEDGEMENTS

My sincere thanks are given to my co-supervisors, Dr. Theodore Stathopoulos and Dr. Patrick John Saathoff, for their financial support and guidance in the course of this work.

Special thanks are given to Dr. Bert Blocken for his many valuable suggestions and assistances on this thesis.

Taking this opportunity, I would like to thank Ms. Jihua Shen, Mr. Bai Zhou and Ms. Guanghan Wang for their unselfish helps throughout my new life in Canada.

Finally, my deepest love and thanks are given to my grandaunt, **Mrs. Ge,** and my parents for their encouragement and boundless love.

TABLE OF CONTENTS

LIST OF FIGURES x

LIST OF TABLES xvii

NOMENCLATURE xix

CHAPTER 1 INTRODUCTION 1

CHAPTER 2 GOVERNING EQUATIONS AND NUMERICAL SOLUTION 5

2.1 Governing Equations 5

2.1.1 Governing Equations for Wind Flow 5

2.1.2 Governing Equation for Pollutant Transportation 5

2.2 Reynolds-Averaged Navier-Stokes Equation and Turbulence Modeling 6

2.2.1 Reynolds-Averaged Navier-Stokes Equation 6

2.2.2 The Standard $k-\varepsilon$ Model 8

2.2.3 The Realizable $k-\varepsilon$ Model 9

2.2.4 The Renormalization Group Theory (RNG) $k-\varepsilon$ Model 10

2.2.5 The Reynolds Stress Model (RSM) 11

2.3 Near Wall Treatment 12

2.3.1 Wall Function Approach 13

2.3.2 Near Wall Modeling Approach 15

2.4 Pollutant Transport Equation 16

2.5 Generalized Discretized Equations 18

2.6 CFD Simulation Procedure 19

2.6.1 Pre-processor 19

2.6.2 Solver 19
2.6.3 Post-processor 22
CHAPTER 3 REVIEW OF STANDARD DISPERSION MODELS 23
3.1 Gaussian Model 23
3.2 Empirical Formula 27
CHAPTER 4 PREVIOUS APPLICATIONS 32
4.1 Introduction 32
4.2 Air Flow around an Isolated Building 33
4.2.1 Wind Tunnel Testing 33
4.2.2 Empirical Model 35
4.2.3 CFD Modeling of Airflow around an Isolated Building 37
4.3 CFD Modeling of Dispersion around an Isolated Building Using Individually Developed Code 44
4.4 FLUENT Applications in Wind-Induced Plume Dispersion 45
4.5 Justification of the Present Study 50
CHAPTER 5 DISPERSION OF EXHAUST FROM AN ISOLATED STACK 51
5.1 Numerical Simulation 51
5.1.1 Pre-processor 51
5.1.2 Solver 56
5.1.3 Post-processor 57
5.2 Results and Discussion 57
CHAPTER 6 DISPERSION AROUND AN ISOLATED CUBIC BUILDING 71
6.1 Introduction 71

6.2 Wind Tunnel Tests 71
6.3 Numerical Simulation 72
6.3.1 Pre-processor 72
6.3.2 Solver 77
6.3.3 Post-processor 78
6.4 Results and Discussion 78
CHAPTER 7 DISPERSION AROUND A RECTANGULAR BUILDING WITH ROOFTOP STRUCTURES 95
7.1 Introduction 95
7.2 Numerical Simulation 96
7.2.1 Pre-processor 96
7.2.2 Solver 100
7.2.3 Post-processor 101
7.3 Results and Discussion 102
7.3.1 Parametric Studies 102
7.3.2 Longitudinal Dispersion Results on the Roof Centerline for Emissions from Stack SL4 110
7.3.3 Lateral and Vertical Dispersion Results for Emissions from Stack SL4 111
CHAPTER 8 CONCLUSIONS, CONTRIBUTIONS AND RECOMMENDATIONS 117
8.1 Conclusions 117
8.2 Contributions 118
8.3 Recommendations for Future Work 119

REFERENCES 120

APPENDIX A 134

A1: Roughness Effects in the Standard Wall Function 134

A2: Nonequilibrium Wall Function 136

APPENDIX B 138

APPENDIX C 141

APPENDIX D 144

APPENDIX E 145

APPENDIX F 148

F1: Velocity Inlet Boundary Condition for an Isolated Stack with Stack Height 2 m and 16 m 148

F2: Velocity Inlet Boundary Condition for Airflow around an Isolated Cubic Building 149

F3: Velocity Inlet Boundary Condition for Airflow around an Isolated Rectangular Building 150

LIST OF FIGURES

Figure 2.1 Flow Chart of Segregated Solver 20

Figure 3.1 Coordinate System Showing Gaussian Distributions in the Horizontal and Vertical Directions (after Turner, 1994) 24

Figure 3.2 Flow Recirculation Regions and Exhaust-to-Intake Stretched-String Distances (after Wilson 1982) 29

Figure 4.1 Flow Patterns and Plume Distribution around a Typical Building (L is the length along the wind, R is the scaling length, H_c is the recirculation region height, after ASHRAE, 2003) 33

Figure 4.2 Mean Velocity Variations (a) at the Top of the Building (x/h = 0, y/h varies and y/h >1, z/h = 0) (b) in the Wake of the Building (x/h = 1, y/h varies, z/h = 0) (U_r is the free stream wind flow and h is the building height, after Castro & Robins, 1977) 34

Figure 4.3 Wind Recirculation Zones on the Flat-Roofed Building (after Wilson (1979)) 36

Figure 4.4 Comparison of k between (a) Wind Tunnel Tests (b) k - ε Model (c) ASM Model (d) LES Model (after Murakami et al., 1992) 39

Figure 4.5 Comparison of Production of k between (a) k - ε Model (b) ASM Model (c) LES Model (after Murakami et al., 1992) 40

Figure 4.6 Comparison of Diagonal Components (a) $\overline{u_1'^2}/2k$ (b) $\overline{u_2'^2}/2k$ (c) $\overline{u_3'^2}/2k$ between Numerical Model Results and Experimental Data (after Murakami et al., 1992) 41

Figure 4.7 Concentration Isopleths ($K = C U_{ref} H^2 / Q_{source}$) on Back Faces of CSU CUBE Model (source location on rooftop 5/6 of the building height from front edge, after Meroney et al., 1999) (a) Experimental Results (b) Numerical Results 49

Figure 5.1 Computational Domain and Boundary Conditions for an Isolated Stack 53

Figure 5.2 Grid Generations for Domain 1000 x 300 x 200 (m) (a) Top View (x - y plane) (b) Side View (x - z plane) (c) Front View (y - z plane) 54

Figure 5.3 Comparison of Velocity Profile between Domain Inlet and Outlet 58

Figure 5.4 Comparisons of (a) Turbulent Kinetic Energy Profile and (b) Turbulent Dissipation Rate between Velocity Inlet and Outlet 59

Figure 5.5 Comparison of Ground Level Concentration on Plume Centerline Directly Downwind of the Stack between the Gaussian Model and FLUENT 6.1 Numerical Models for Stack Height of 2 and 16 m 61

Figure 5.6 Stack Height of 2 m Case (a) Vertical Concentration Distribution 200 m Downwind at Plume Center (b) Crosswind Concentration Distribution 200 m Downwind at Stack Height Level and (c) at Ground Level 63

Figure 5.7 Stack Height of 16 m Case (a) Vertical Concentration Distribution 200 m Downwind at Plume Center (b) Crosswind Concentration Distribution 200 m Downwind at Stack Height Level and (c) at Ground Level 64

Figure 5.8 Influence of Mesh Density on Concentration Distribution for H_s = 2 m (a) Ground Level at Plume Center (b) Vertical Distribution 200 m Downwind at Plume

Center (c) Crosswind Distribution 200 m Downwind at Stack Height Level and (d) at Ground Level 66

Figure 5.9 Influence of Mesh Density on Concentration Distribution for H_s = 16 m (a) Ground Level at Plume Center (b) Vertical Distribution 200 m Downwind at Plume Center (c) Crosswind Distribution 200 m Downwind at Stack Height Level and (d) at Ground Level 67

Figure 5.10 Influences of Turbulent Schmidt Number on Concentration Distribution (a) Vertical Distribution 200 m Downwind at Plume Center for stack height 16 m (b) Crosswind Distribution 200 m Downwind at Ground Level for stack height 16 m (c) Vertical Distribution 200 m Downwind at Plume Center for stack height 2 m (b) Crosswind Distribution 200 m Downwind at Ground Level for stack height 2 m... 68

Figure 5.11 Influences of QUICK and POWER LAW Discretization Scheme on Concentration Distribution for the 16 m stack (a) Ground Level at Plume Center (b) Vertical Distribution 200 m Downwind at Plume Center (c) Crosswind Distribution 200 m Downwind at Stack Height Level (d) at Ground Level 69

Figure 6.1 Sizes and Layout of the Computational Domain and Boundary Conditions (Note: names outside parentheses are for components of the computational domain and inside are for numerical boundary conditions)..... 73

Figure 6.2 Grid Generation for Domain 1.26 x 0.78 x 0.4 (m) (a) Top View (x-y plane) (b) Side View (x-z plane) (c) Front View (y-z plane) 74

Figure 6.3 Variation of Boundary Layer Parameters with Height at the Inlet (a) Wind Velocity Profile (b) Turbulent Kinetic Energy Profile (c) Turbulent Dissipation Rate Profile (d) Turbulence Intensity..... 76

Figure 6.4 Numerical Evaluations of (a) Velocity Magnitude Profile (b) Turbulent Kinetic Energy Profile and (c) Turbulent Dissipation Rate Profile between Velocity Inlet and Outlet 79

Figure 6.5 Surface Pressure Coefficients on the Cube 80

Figure 6.6 Variations of the Mean Longitudinal Velocity with Height on the Center Line (y = 0) 81

Figure 6.7 Variations of Mean Longitudinal Velocity in Lateral Direction on the Center Line at Half the Height of the Building 82

Figure 6.8 Contours of Dimensionless Concentration K on the (a) Top (b) Side (c) Back of the Cubic Building from Wind Tunnel Test 83

Figure 6.9 K Distributions Obtained with RSM1 Numerical Simulation on the (a) Roof (b) Side Wall (c) Back Wall (turbulent Schmidt number 0.3) 84

Figure 6.10 K Distributions Obtained with RSM2 Numerical Simulation on the (a) Roof (b) Side Wall (c) Back Wall (turbulent Schmidt number 0.3) 85

Figure 6.11 K Distributions on Centerline of the Roof and Leeward Wall versus String Distance from Vent Obtained with the RSM1 and RSM2 Model 86

Figure 6.12 K Distributions Obtained with Realizable $k-\varepsilon$ Numerical Simulation on the (a) Roof (b) Side Wall (c) Back Wall (turbulent Schmidt number 0.3) 87

Figure 6.13 Contours of Turbulent Kinetic Energy k Predicted from (a) Reynolds Stress Model with Wall Reflection Effects (b) Realizable $k-\varepsilon$ Model 89

Figure 6.14 K Distributions on Centerline of the Roof and Leeward Wall versus String Distance from Vent Obtained with the RSM1 and Realizable $k-\varepsilon$ Model 90

Figure 6.15 Concentration K versus String Distance from Vent between Numerical Results and Wind Tunnel Test Data 90

Figure 6.16 Distribution of Dimensionless Concentration (K) in a Vertical Plane in the near wake Region ($x/H_b = 1.0$) for a Central Flush Stack (wind direction is normal to the building) (a) Numerical Model (RSM1) (b) Wind Tunnel (Li & Meroney, 1983) 91

Figure 6.17 Distribution of Dimensionless Concentration (K) in a Vertical Plane in the near wake Region ($x/H_b = 4.0$) for a Central Flush Stack (wind direction is normal to the building) (a) Numerical Model (RSM1) (b) Wind Tunnel (Li & Meroney, 1983) 92

Figure 6.18 Contour of Dimensionless Concentration K on the (a) Top (b) Side (c) Back of the Cubic Building Obtained with RSM1 Numerical Model and Turbulent Schmidt number 0.7 94

Figure 7.1 Dimensions of the BE Building (after Stathopoulos et al., 2003) 96

Figure 7.2 Computational Domain and Boundary Conditions for the Stack SL4 Test (θ=120^0) 97

Figure 7.3 Mesh Distributions from (a) Top View (x - y plane) (b) Side View (x - z plane) (c) Front View (y - z plane) 98

Figure 7.4 CFD Boundary Conditions (a) Velocity Profile (b) Turbulent Kinetic Energy Profile (c) Turbulent Dissipation Rate (d) Turbulence Intensity at the Velocity Inlet 100

Figure 7.5 Receptor Locations for Case Study with Stack SL4 101

Figure 7.6 Recirculation Zones around the BE building and the Skylight Structure (L_{cb}, L_{cs} , H_{cb} and H_{cs} are the length and height of recirculation zones induced by roof edges of the BE building and the skylight structure, respectively; L_{rb} and L_{rs} are the length of wake zones behind the BE building and the skylight structure, respectively) 103

Figure 7.7 Minimum Dilution versus Distance from Stack SL4 (a) the Realizable k - ε Model and Standard k - ε Model (b) the Realizable k - ε Model and RNG k - ε Model (turbulent Schmidt number 0.7) 106

Figure 7.8 K Distributions on the Rooftop (a) Without the Skylight Structure (b) With the Skylight Structure Using the Realizable $k-\varepsilon$ Model for M = 10.5 108

Figure 7.9 Effects of Turbulent Schmidt Number on the Dilution Ratio of Emissions from Stack SL4 Using the Realizable $k-\varepsilon$ Model 109

Figure 7.10 Comparisons of Dilution Ratios on the Plume Centerline Using the Realizable $k-\varepsilon$ Model with Enhanced Wall Treatment and Turbulent Schmidt Number 0.7 for M = 5.6, 8.7 and 10.5 110

Figure 7.11 Comparisons of Dilution Ratios on the Plume Centerline between Numerical Model Using the Realizable $k-\varepsilon$ Model with Enhanced Wall Treatment and Turbulent Schmidt Number 0.7 and Empirical Formula for M = 8.7 111

Figure 7.12 Comparison of Concentration Distribution of the Specified Receptors between Field Test (Italic) and Realizable $k-\varepsilon$ Model (Bold) for M = 8.7 112

Figure 7.13 (a) Locations of the Specified Receptors (b) Comparisons of Vertical Concentration Distributions at the Specified Receptors between the Numerical Results and Field Test Data 113

Figure 7.14 (a) Comparisons of Crosswind Concentration Distributions at the Specified Receptors (shown in Fig. 7.5) at the Rooftop Level between Numerical Results and Field Test Data (b) Profiles of Crosswind Concentration Distribution at the Effective Height of 21 m by the Numerical Method 115

Figure 7.15 (a) Locations of Specified Receptors in the Wake of the Building (b) Vertical Concentration Distributions by the Realizable $k-\varepsilon$ Model 116

Figure B.1 Pasquill – Gifford Dispersion Parameters (a) Horizontal (b) Vertical (for neutral stability D condition, after Turner, 1994) 140

Figure C.1 Edge Mesh Grading Parameters for Single-sided Grading (Gambit 2.0) 141

Figure C.2 Edge Mesh Grading Parameters for Double-sided Grading (Gambit 2.0) ... 141

Figure E.1 Photos Showing Upstream Terrain for the BE Building (from southeast view) in the Present Study 145

LIST OF TABLES

Table 5-1 Parametric Study of Plume Dispersion from One Isolated Stack in Open Country Terrain: Standard $k-\varepsilon$ Model and Standard Wall Function for All Cases 65

Table 7-1 Parametric Studies of Dispersion of Emissions from the Stack SL4 (M = 10.5) 102

Table 7-2 Effect of the Realizable k-ε Model with Different Wall Treatments on the Length and Height of the Recirculation Zones (Fig. 7.6) for the Case of Emissions from Stack SL4 104

Table 7-3 Effect of Different Turbulence Models with the Enhanced Wall Treatment on the Length and Height of the Recirculation Zones (Fig. 7.6) for the Case of Emissions from Stack SL4 105

Table B-1 Pasquill Stability Categories (after Pasquill, 1961) 138

Table C-1 Mesh Resolution Distribution for the Computational Domain along the (a) +x (b) +y (c) +z Direction (Stack Height: 16 m; Unit: Meter) 142

Table C-2 Mesh Resolution Distribution for the Computational Domain along the (a) +x (b) +y (c) +z Direction (Stack Height: 2 m; Unit: Meter) 143

Table D-1 Mesh Resolution Distribution for the Computational Domain along the (a) +x (b) +y (c) +z Direction (Unit: Meter) 144

Table E-1 Mesh Resolution Distribution for the Computational Domain along the (a) +x (b) +y (c) +z Direction (Unit: Meter) 146

Table E-2 Receptor Coordinates for Case Study with Stack SL4 (Unit: Meter, Full Scale) 147

NOMENCLATURE

ROMAN SYMBOLS

A	bounding surface of a control volume
A_e	exhaust face area
B_1	distance dilution parameter in Wilson-Lamb model
B_L	larger of upwind building face dimension
B_s	smaller of upwind building face dimension
C	concentration at a receptor
C_1, C_2	constants in realizable $k-\varepsilon$ turbulence model
C_e	concentration at the exit of the exhaust
C_{ks}	roughness constant
$C_\mu, C_{1\varepsilon}, C_{2\varepsilon}$	constants in the standard and RNG $k-\varepsilon$ turbulence model
D	dilution factor
d	stack diameter
D_0	initial dilution in Wilson-Lamb model
D_d	distance dilution in Wilson-Lamb model
D_m	molecular diffusion coefficient for pollutant in the mixture
$D_{m,t}$	total diffusion coefficient for pollutant in the mixture
$D_{\min}$	minimum dilution in Wilson-Lamb model

D_r	minimum concentration at the roof level in ASHRAE (2003)
D_t	turbulent diffusion coefficient
D_v	volume concentration dilution factor
f	volume (molar) fraction at the receptor
f_e	volume (molar) fraction in the exhaust
f_r	roughness function
G_k	generation of turbulent kinetic energy
h	plume height above the roof
H	the effective height of the plume centerline
H_b	building height
H_s	stack height in the Gaussian model
h_d	stack wake downwash
h_r	plume rise
h_s	height of the stack tip above the roof
I_1	the length of the first interval of the grid
I_n	the length of the last interval of the grid
k	turbulent kinetic energy
K	normalized concentration coefficients or dimensionless concentration
k_p	turbulent kinetic energy at point P
k_s	physical roughness height
L	building length

M	momentum ratio
n	normal vector of the bounding surface
p	static pressure
P	mean pressure or the center point of the wall adjacent cell
q	pollutnat emission rate
R	single ratio for the meshing
R_1	double ratio for the meshing
R_{et}	turbulent Reynolds number
S	stretched string distance
Sc	molecular Schmidt number
Sc_t	turbulent Schmidt number
s_{ij}	velocity strain rate tensor
S_{ij}	mean velocity strain rate tensor
S_ϕ	source term in the discretization equation
t	time
t_{avg}	concentration average time
u_{ABL}^*	friction velocity
U_{Hb}	wind speed at the building height
U	mean velocity in x direction
U_i	mean velocity components
u_i	total velocity

u_i'	fluctuating components
u	referred velocity in the Gaussian model
U_p	mean velocity of the fluid at point P
V_e	exhaust speed
W	building width
x	receptor distance or location in Cartesian coordinate system
x_i	space coordinate
y^+, y^*	dimensionless height
y_i	total mass fraction of each pollutant i
Y_i	mean mass fraction of component i in the contaminant
y_i'	fluctuating mass fraction of component i in the contaminant
y_p	height of the center point of the wall-adjacent cells
z_0	roughness length
Z_g	gradient height

GREEK SYMBOLS

ø	general variable in the discretization equation
α	power law
$\alpha_k, \alpha_\varepsilon$	inverse effective Prandtl numbers for k and ε in the RNG $k-\varepsilon$ model
β	stack capping factor

δ	height of the atmospheric boundary layer
δ_{ij}	Kronecker delta
ε	dissipation rate
θ	wind direction
κ	von Karman's constant (= 0.42)
μ	dynamic viscosity of the fluid
μ_{eff}	effective viscosity in the RNG $k-\varepsilon$ model
μ_t	eddy viscosity of the fluid
ν	kinematic viscosity of the fluid
ρ	fluid density
σ_0	initial source size
σ_ε	Prandtl number for turbulent dissipation rate
σ_k	Prandtl number for turbulent kinetic energy
σ_y, σ_z	plume spreads in the crosswind and vertical directions
σ_θ	standard deviation of wind direction fluctuations in degrees
χ	air pollutant concentration in the Gaussian model
Γ_ϕ	diffusion coefficient in the discretization equation

SUBSCRIPTS

i, j, k	the x, y and z direction for a vector

OPERATORS

div	divergence operator
grad	gradient operator

ACRONYMS

ABL	Atmospheric Boundary Layer
CFD	Computational Fluid Dynamics
QUICK	Quadratic Upwind Interpolation for Convective Kinematics
RNG	Renormalization Group theory
RSM	Reynolds Stress Model
SIMPLE	Semi-Implicit Method for Pressure-Linked Equations
ASHRAE	American Society of Heating, Refrigerating and Air-Conditioning Engineers
SIMPLEC	SIMPLE-Consistent
RANS	Reynolds-Averaged Navier-Stokes
ASM	Algebraic Stress Model
LES	Large Eddy Simulation
UDF	User Defined Function

CHAPTER 1 INTRODUCTION

Air pollution can affect the health of human beings in many respects. Emissions from rooftop stacks can affect indoor air quality if the plume impinges on air intakes of the emitting building or surrounding buildings. The requirement of precise prediction of plume concentration distribution on or near buildings has been increasing in recent years because it is very important for building engineers to design proper exhaust stacks and set proper air intakes to avoid adverse air quality impacts.

The prediction of plume concentration is a difficult task, especially in the urban environment. It requires the knowledge of air pollution meteorology and dispersion. It also requires the knowledge of building aerodynamics because structures can strongly affect plume behavior.

The existing methods used to predict pollutant dispersion are field tests, wind tunnel or water tunnel simulations, analytical method, empirical formulae and computational fluid dynamics (CFD) numerical modeling based on the finite difference method, the finite element method or the control volume method.

Field tests are conducted in the real atmospheric boundary layer providing information of the real complexity of the phenomenon. However, they have some limitations, such as large variation of wind and weather conditions. Moreover, it is impossible to measure the resulting pollutant distributions if a new facility or a new building has not been constructed.

Fluid modeling performed in a boundary layer wind tunnel or water channel can accurately predict plume dispersion for complex geometries. However, the disadvantages are high cost, not applicable for light wind conditions, and scaling problems. The "scaled" results from wind tunnel or water channel tests need to be validated with field tests.

The analytical method refers to the Gaussian model, which can be effective when there are no obstacles between the emission source and receptors (Pasquill & Smith, 1983, Huber and Synder, 1982).

Empirical formulae, such as ASHRAE models, are based on the concentration measurements obtained in the wind tunnel simulation or water tunnel simulation. They only evaluate the minimum dilution factor on the plume centerline. They do not apply off the plume centerline. Empirical formulae can be easily used comparing with other methods.

CFD methods have been applied in many industrial fields to simulate complicated fluid flows and scalar transportation problems. CFD methods are less expensive than field tests and wind tunnel tests. Moreover, numerical methods can provide the flow properties at every point simultaneously. The rapid development of computers has increased the number of flows that can be modeled with CFD. For particular applications, the CFD technique has been shown to be fast, economical, and highly accurate (Ferziger & Peric, 1999). However, the numerical results are always approximate. Errors could arise from the approximations in the differential equations, diecretization process and iterative methods.

The commercial CFD code, FLUENT 6.1, is used in the present study. It is a comprehensive, unstructured solver based on the control volume method. It serves a broad range of industrial applications with a variety of turbulence models: Spalart - Allmaras model, various versions of the $k-\varepsilon$ model, $k-\omega$ model, Reynolds stress model (RSM), and large eddy simulation (LES) (Fluent, 2003). Several researchers have tried to model the dispersion of stack emissions in the atmospheric boundary layer using FLUENT. They found that FLUENT gave mixed results in terms of accuracy of predicted concentrations compared to wind tunnel experiments (Leitl et. al, 1997).

The objectives of this work are to apply the CFD method to model the dispersion of stack emissions in the atmospheric boundary layer (ABL). This will be done using different turbulence models, advanced wall treatments and high order discretization methods available in FLUENT 6.1.

Three cases have been studied. The first case involves a simulation of dispersion for an isolated stack in a neutral, open country boundary layer. The simulation results are compared with those from the analytical Gaussian model, recommended by the U. S. Environment Protection Agency (EPA) (U. S. EPA, 2004) as an environmental impact assessment tool.

The second case is concerned with the simulation of dispersion of emissions from a flush stack located at the roof center of a cubic building under a neutral open country condition. The wind direction is normal to the building. The simulation results are compared with wind tunnel test data.

The third case is concerned with the simulation of dispersion of emissions from a rooftop stack under a neutral urban condition. In this work, the results are obtained for a short

stack on a three-story rectangular building located in downtown Montreal. The numerical simulation results are compared with those from ASHRAE models and field tests.

This thesis is structured as following:

Chapter 1 Introduction to the significance of dispersion of emissions around the building, the prediction methods and objectives of this thesis work

Chapter 2 Theoretical backgrounds of the governing equations and their numerical solution

Chapter 3 Standard dispersion models (analytical/empirical)

Chapter 4 Review of past applications on predicting fluid flow and dispersion of emissions from stacks in the atmospheric boundary layer from wind tunnel, field studies and CFD modeling

Chapter 5 Case study of dispersion for an isolated stack under a neutral open country condition

Chapter 6 Case study of dispersion from a rooftop stack around a cubic building

Chapter 7 Case study of dispersion from a rooftop stack around a rectangular building

Chapter 8 Conclusions and recommendations for future work

CHAPTER 2 GOVERNING EQUATIONS AND NUMERICAL SOLUTION

2.1 Governing Equations

2.1.1 Governing Equations for Wind Flow

The dynamics of any kind of fluid flow, such as wind flow in the atmosphere, is governed by the fundamental laws of conservation of mass and momentum (Navier-Stokes Equations):

$$\frac{\partial \rho}{\partial t}+\frac{\partial(\rho u_i)}{\partial x_i}=0 \tag{2-1}$$

$$\frac{\partial}{\partial t}(\rho u_i)+\frac{\partial(\rho u_i u_j)}{\partial x_i}=\frac{\partial}{\partial x_i}(-p+2\mu s_{ij}) \tag{2-2}$$

where $i = 1, 2, 3$, $j = 1, 2, 3$, ρ is the density of fluid, μ the dynamic viscosity, p the static pressure, s_{ij} the velocity strain rate tensor, $s_{ij}=\frac{1}{2}(\frac{\partial u_i}{\partial x_j}+\frac{\partial u_j}{\partial u_i})$

2.1.2 Governing Equation for Pollutant Transportation

The governing equation for pollutant transportation is

$$\frac{\partial}{\partial t}(\rho y_i)+\frac{\partial}{\partial x_i}(\rho u_i y_i)=\rho D_i \frac{\partial^2 y_i}{\partial x_i \partial x_j} \tag{2-3}$$

where y_i is the mass fraction of each pollutant i, D_i is the diffusion coefficient for pollutant i in the mixture, i =1, 2, 3 in the terms of x_i and u_i, j =1, 2, 3. (Fluent, 2003)

2.2 Reynolds-Averaged Navier-Stokes Equation and Turbulence Modeling

2.2.1 Reynolds-Averaged Navier-Stokes Equation

Usually, a complete solution of the time dependent Navier-Stokes equations is too difficult to achieve for arbitrary flows. Two alternative methods can be employed to transform the Navier-Stokes equations in such a way that the small scale turbulent fluctuations do not have to be directly solved: Reynolds-averaged (RANS) and filtering (Large Eddy Simulation (LES)).

The Reynolds-Averaged Navier-Stokes equations represent transport equations for the mean flow quantities only, with all the scales of the turbulence being modeled. Filtering is essentially a manipulation of the exact Navier-Stokes equations, which only removes eddies smaller than the size of the filter, which is usually taken as the mesh size.

The Reynolds averaging approach requires much less computational effort than LES. Therefore, RANS is generally adopted for practical engineering calculations. All case studies examined in this thesis are focused on the RANS approach, which operates as follows:

The solution variables in the instantaneous Navier-Stokes equations are decomposed into the mean and fluctuating components. The total velocity in Cartesian form u_i is decomposed into the mean components U_i and the fluctuating components u_i', i.e. $u_i = U_i + u_i'$ $(i = 1, 2, 3)$

Substituting expressions of this form for each flow variable into the instantaneous continuity and momentum equations and taking an ensemble average yields the RANS equations for the steady state flow:

$$\frac{\partial U_i}{\partial x_i} = 0 \tag{2-4}$$

$$U_j \frac{\partial U_i}{\partial x_j} = \frac{1}{\rho}\frac{\partial}{\partial x_j}(-P\delta_{ij} + 2\mu S_{ij} - \overline{\rho u_i' u_j'}) \tag{2-5}$$

where $i = 1, 2, 3$, $j = 1, 2, 3$, ρ is the density of fluid, μ the dynamic viscosity, P the mean pressure, S_{ij} the velocity strain rate tensor, $S_{ij} = \frac{1}{2}(\frac{\partial U_i}{\partial x_j} + \frac{\partial U_j}{\partial x_i})$, and δ_{ij} is the Kronecker delta.

Through the Reynolds averaging approach, more variables are introduced which make the above equations not closed. To close the above RANS equations, the Reynolds stresses $-\overline{\rho u_i' u_j'}$ should be expressed in terms of the known variables. There are two methods to solve this problem. One is the "eddy viscosity model" which includes various $k-\varepsilon$ models. The other is the "Reynolds stresses transport model" which includes Reynolds Stress Model (RSM) and Algebraic Stress Model (ASM). Note that in this thesis, the RSM was used because there is no ASM available in FLUENT 6.1. Murakami et al. (1992) used the ASM to study time-averaged flow around a cube. The model equations used in his studies were following Rodi (1976) and Gibson & Launder (1978), except for the treatment of the wall reflection term (Murakami et al. 1990).

In the "eddy viscosity model", the Reynolds stresses are modeled using Boussinesq hypothesis (Hinze, 1975). This assumes that the principal axes of the Reynolds-stress tensors are coincident with those of the mean strain-rate tensor at all points in a turbulent flow. In mathematical terms,

$$-\overline{u_i' u_j'} = \frac{\mu_t}{\rho}(\frac{\partial U_i}{\partial x_j} + \frac{\partial U_j}{\partial x_i}) - \frac{2}{3}\delta_{ij} k \tag{2-6}$$

where μ_t $(=\rho C_\mu \frac{k^2}{\varepsilon})$ is the eddy viscosity, ε is the dissipation rate, k $(=\overline{u_i' u_i'}/2)$ is the turbulent kinetic energy and $i = 1, 2, 3$.

Substitution of equation (2-6) into equation (2-5) gives:

$$\rho U_j \frac{\partial U_i}{\partial x_j} = \frac{\partial}{\partial x_i}(-P) + (\mu + \mu_t)\frac{\partial^2 U_i}{\partial x_j{}^2} \tag{2-7}$$

2.2.2 The Standard $k-\varepsilon$ Model

In the standard $k-\varepsilon$ model (Launder & Spalding, 1972), the turbulent kinetic energy k and its dissipation rate ε are obtained from the following transport equations:

$$\rho \frac{Dk}{Dt} = \frac{\partial}{\partial x_i}\left[\left(\mu + \frac{\mu_t}{\sigma_k}\right)\frac{\partial k}{\partial x_i}\right] + G_k - \rho\varepsilon \tag{2-8}$$

$$\rho \frac{D\varepsilon}{Dt} = \frac{\partial}{\partial x_i}\left[\left(\mu + \frac{\mu_t}{\sigma_\varepsilon}\right)\frac{\partial \varepsilon}{\partial x_i}\right] + C_{1\varepsilon}\frac{\varepsilon}{k}G_k - C_{2\varepsilon}\rho\frac{\varepsilon^2}{k} \tag{2-9}$$

where $\mu_t = \rho C_\mu \frac{k^2}{\varepsilon}$

In these equations, G_k represents the generation of turbulent kinetic energy due to the mean velocity gradients, $G_k = -\rho\overline{u_i' u_j'}\frac{\partial U_j}{\partial x_i}$. The model constants proposed by Launder et al. (1974) have the following values: $C_{1\varepsilon} = 1.44$, $C_{2\varepsilon} = 1.92$, $C_\mu = 0.09$, $\sigma_k = 1.0$, and $\sigma_\varepsilon = 1.3$. These constant values have been found to work fairly well for the wide range of wall-bounded and free shear flow (Ferziger & Peric, 1999; Versteeg & Malalasekera, 1995).

Compared with other k- ε models described below, the standard k- ε model needs the least computer resources and is more promising for some engineering applications. The lower cost is due to some simplifying assumptions, such as a turbulent equilibrium assumption near the wall and the use of various constants in the turbulent transportation equations. These assumptions limit the applicability of the standard k- ε model.

To improve the simulation results from the standard $k-\varepsilon$ model for cases in which the flow includes strong streamline curvature, vortices and rotation, modifications have been applied, such as the realizable $k-\varepsilon$ model proposed by Shih et al. (1995) and Re-Normalization Group theory proposed by Yakhot & Orszag (1986) and Choudhury (1993). Both of these models have shown substantial improvements over the standard $k-\varepsilon$ model. The major differences in these models are

1) the method of calculation turbulent viscosity;

2) the turbulent Prandtl numbers governing the turbulent diffusion of k and ε;

3) the generation and destruction terms in the ε equation

2.2.3 The Realizable $k-\varepsilon$ Model

The transport equations in the realizable $k-\varepsilon$ model proposed by Shih et al. (1995) are

$$\rho\frac{Dk}{Dt}=\frac{\partial}{\partial x_i}[(\mu+\frac{\mu_t}{\sigma_k})\frac{\partial k}{\partial x_j}]+G_k-\rho\varepsilon \tag{2-10}$$

and

$$\rho\frac{D\varepsilon}{Dt}=\frac{\partial}{\partial x_j}[(\mu+\frac{\mu_t}{\sigma_\varepsilon})\frac{\partial \varepsilon}{\partial x_j}]+\rho C_1 S\varepsilon-\rho C_2\frac{\varepsilon^2}{k+\sqrt{\nu\varepsilon}} \tag{2-11}$$

where $C_1 = \max[0.43, \frac{\eta}{\eta+5}]$, $\eta = S\frac{k}{\varepsilon}$, $S = \sqrt{2S_{ij}S_{ij}}$, $\mu_t = \rho C_\mu \frac{k^2}{\varepsilon}$, $C_2 = 1.9$, $\sigma_k = 1.0$, $\sigma_\varepsilon = 1.2$

The realizable $k-\varepsilon$ model differs from the standard $k-\varepsilon$ model in the following aspects:

1) Make C_μ variable (Reynolds, 1987) by sensitizing it to the mean flow and the turbulence in order to keep the normal stress $\overline{u'^2}$ always positive and to satisfy the Schwarz inequality of shear stresses ($\overline{u_i' u_j'}^2 \leq \overline{u_i'^2}\,\overline{u_j'^2}$; no summation over i and j; Shih et al, 1995).

2) A new equation for ε based on the dynamic equation of the mean square vorticity fluctuation is used.

The dissipation equation in the realizable $k-\varepsilon$ model represents the spectral energy transfer very well. Meanwhile, the destruction term does not have any singularity even if k vanishes or becomes smaller than zero, which also happens on the wall boundary. It was found that this model performed well for a variety of flows including the backward facing step, while the standard $k-\varepsilon$ model did not (Shih et al, 1995).

2.2.4 The Renormalization Group Theory (RNG) $k-\varepsilon$ Model

The RNG $k-\varepsilon$ model used in FLUENT 6.1 is based on a mathematical technique called "renormalization group". A more detailed description of RNG theory and its application to turbulent flow can be found in the paper by Choudhury (1993). Its transport equations have a similar form as those of the standard $k-\varepsilon$ model

$$\rho\frac{Dk}{Dt}=\frac{\partial}{\partial x_i}(\alpha_k\mu_{eff}\frac{\partial k}{\partial x_j})+G_k-\rho\varepsilon \tag{2-12}$$

$$\rho\frac{D\varepsilon}{Dt}=\frac{\partial}{\partial x_i}(\alpha_\varepsilon\mu_{eff}\frac{\partial \varepsilon}{\partial x_j})+C_{1\varepsilon}\frac{\varepsilon}{k}G_k-C_{2\varepsilon}\rho\frac{\varepsilon^2}{k} \tag{2-13}$$

The constants are $C_{1\varepsilon}=1.42$, $C_{2\varepsilon}=1.68$ and μ_{eff} is the effective viscosity. The quantities α_k and α_ε are the inverse effective Prandtl numbers for k and ε, respectively. For further details about these parameters, the reader is referred to Choudhury (1993).

2.2.5 The Reynolds Stress Model (RSM)

Instead of using Boussinesq's hypothesis to model turbulence terms in Equation (2-2), RSM solves the Reynolds stress terms, $\overline{u_i' u_j'}$, using the following transport equation:

$$\rho\frac{D}{Dt}(\overline{u_k u_i' u_j'})=-\frac{\partial}{\partial x_k}[\overline{\rho u_i' u_j' u_k'}+\overline{p(\delta_{kj}u_i'+\delta_{ik}u_j')}]+\frac{\partial}{\partial x_k}[\mu\frac{\partial}{\partial x_k}(\overline{u_i' u_j'})]$$

$$-\rho(\overline{u_i' u_j'}\frac{\partial u_j}{\partial x_k}+\overline{u_j' u_k'}\frac{\partial u_i}{\partial x_k})+\overline{p(\frac{\partial u_i'}{\partial x_j}+\frac{\partial u_j'}{\partial x_i})}-2\mu\overline{\frac{\partial u_i'}{\partial x_k}\frac{\partial u_j'}{\partial x_k'}} \tag{2-14}$$

where the term on the left hand is the total derivative term; for the right hand of the Equation (2-12), the first term is the turbulent diffusion $D_{T,ij}$; the second term is the molecular diffusion $D_{L,ij}$; the third term is the stress production P_{ij}; the fourth term is the pressure strain ϕ_{ij}; the last term is the dissipation ε_{ij}.

The Reynolds Stress Model (RSM) abandons the isotropic eddy-viscosity hypothesis in the $k-\varepsilon$ model because it closes the Reynolds-averaged Navier-Stokes equations by solving the transport equations for Reynolds stresses in each direction, together with an

equation for the dissipation rate. It has greater potential to represent turbulent flow phenomena more correctly. Generally, it could give more accurate flow field for complex flows with streamline curvature, swirl, rotation and rapid changes in strain rate. The primary focus was on obtaining a good approximation or parameterization of the correlations between pressure and strain fluctuations and modeling dissipation rate terms. For more details, the reader is referred to Gibson & Launder (1978), Fu et al. (1987), Launder (1989) and Sarkar & Balakrishnan (1990). The drawback of the RSM, compared with the $k-\varepsilon$ model, is that it needs more computer resources.

2.3 Near Wall Treatment

In the commercial CFD code used here, there are two methods to model the near-wall region. One method is the "wall function approach", which uses semi-empirical algebraic formulae to solve the velocity and turbulent quantities in the viscosity-affected regions between the wall and the fully turbulent region. It saves the computer resources needed to solve these viscosity-affected regions by using a relatively coarse grid. The wall function method is popular because it is economical, robust, and reasonably accurate in most high Reynolds number flows (Re>20,000).

The other method is called "near wall modeling". In this method, the turbulence models are modified to account for the presence of the wall and are solved all the way from the fully turbulent region to the wall by using a relatively fine grid. If Reynolds number is low or there are severe pressure gradients leading to boundary layer separations, the assumptions in the wall function approach are not valid. In this case, near wall modeling should be used to solve the viscosity-affected regions. To use this near wall modeling

method, a fine grid is required. However, the wall function approach is still used when and where the grid is not fine enough.

2.3.1 Wall Function Approach

There are two kinds of wall function methods used in FLUENT 6.1: standard wall functions and non-equilibrium wall functions.

Standard wall functions are based on the proposal of Launder & Spalding (1974). The law-of-the-wall for mean velocity yields:

$$U^* = \frac{1}{k}\ln(Ey^*) - \Delta B \tag{2-15}$$

where

$$U^* = \frac{U_p C_\mu^{1/4} k_p^{1/2}}{\tau_w / \rho} \qquad y^* \equiv \frac{\rho C_\mu^{1/4} k_p^{1/2} y_p}{\mu} \qquad \Delta B = \frac{1}{\kappa}\ln f_r$$

and U^* is the dimensionless velocity;

y^* is the dimensionless height;

ΔB is the roughness function (Appendix A);

κ is the von Karman's constant (= 0.42);

E is the empirical constant for smooth wall (= 9.81);

P is the center point of the wall adjacent cell;

U_p is the mean velocity of the fluid at point P;

k_p is the turbulent kinetic energy at point P;

y_p is the distance from point P to the wall;

τ_w is the shear stress on the wall;

μ is the dynamic viscosity of the fluid;

f_r is a function of roughness that quantifies the shift of the intercept due to roughness (Appendix A);

The logarithmic law for mean velocity is known to be valid for y^*>30 to 60. In FLUENT 6.1, the log-law is employed when y^*>11.225. When the mesh is such that y^*<11.225 at the wall adjacent cells, FLUENT applies the laminar stress-strain relationship that can be written as $U^* = y^*$.

The boundary condition for k is $\frac{\partial k}{\partial n}=0$ where n is the local coordinate normal to the wall. $\varepsilon = \frac{C\mu^{\frac{3}{4}} k_p}{\kappa y_p}$ and production $G_k \approx \tau_w \frac{\partial U}{\partial y}$.

The velocity profile of the turbulent flow in the recirculation region behind a backward facing step was measured by Adams & Johnston (1998). Zhou (1995) compared the velocity profile measured by Adams with the log-law velocity profile and found that the measured velocity distribution deviates significantly from the logarithmic part of the wall function when $y^+ > 7$ ($y^+ = \frac{u_{ABL}^* y_p}{\nu}$ where u_{ABL}^* is the friction velocity, y_p is the height of the center point of the wall-adjacent cells and ν is the kinematic viscosity, $\frac{\mu}{\rho}$). This indicates that the Launder & Spalding's log-law in the standard wall functions should be used carefully when there is a separation zone in the fluid field.

Non-equilibrium wall functions are based on the proposal of Kim & Choudhury (1995). More details are given in Appendix A. The key differences between the non-equilibrium wall functions and the standard wall functions are:

1) Launder and Spalding's log-law for mean velocity is sensitized to pressure-gradient effects;

2) The two-layer-based concept is adopted to compute the budget of turbulent kinetic energy ($\overline{G_k}$, $\bar{\varepsilon}$) in the wall-neighboring cells.

In the following numerical studies of dispersion from an isolated stack and dispersion around a cubic building under open country condition, the wall function approach is used.

2.3.2 Near Wall Modeling Approach

Enhanced wall treatment (Fluent, 2003) is a near wall modeling method that is available in FLUENT 6.1. It combines a two-layer model with enhanced wall functions, as proposed by Kader (1981). In the fully turbulent region, the k- ε model or RSM is employed. In the viscosity-affected near-wall region, the one-equation model of Wolfstein (1969) is employed. The model possesses the accuracy of the standard two-layer approach for fine near-wall meshes and at the same time, it does not significantly reduce accuracy for wall-function meshes. For more details, the reader is referred to Kader (1981) and Wolfstein (1969). In the following numerical study of dispersion around an actual rectangular building with rooftop structures in urban area, this method is used.

2.4 Pollutant Transport Equation

Given a fluid field with known turbulence parameters, the pollutant transport equation can be solved. Likewise, the mass fraction of each pollutant y_i can be decomposed into the mean component Y_i and the fluctuating component y_i'. Equation (2-3) becomes

$$\rho U_j \frac{\partial Y_i}{\partial x_j} = \rho D_{i,m} \frac{\partial^2 Y_i}{\partial x_j \partial x_j} - \frac{\partial}{\partial x_j} (\overline{y_i' u_j'}) \tag{2-16}$$

where $D_{i,m}$ is the diffusion coefficient for pollutant i in the mixture and $j = 1, 2, 3$.

In laminar flow, the right side of equation (2-16) becomes $(\rho D_{i,m})\nabla^2 Y_i$, where $D_{i,m}$ is the molecular diffusion coefficient for pollutant i in the mixture; In turbulent flow, with the assumption $-\overline{y_i' u_j'} = \frac{\mu_t}{Sc_t}\frac{\partial Y_i}{\partial x_j}$, the right side of equation (2-16) becomes $(\rho D_{i,m} + \frac{\mu_t}{Sc_t})\nabla^2 Y_i$, where Sc_t is the turbulent Schmidt number ($Sc_t = \frac{\mu_t}{\rho D_t}$). The turbulent Schmidt number relates the effective turbulent diffusion coefficient, D_t, with the eddy viscosity, μ_t. In turbulent flow, D_t is much larger than $D_{i,m}$, so by neglecting $D_{i,m}$, equation (2-16) becomes

$$U_j \frac{\partial Y_i}{\partial x_j} = D_t \frac{\partial^2 Y_i}{\partial x_j \partial x_j} \tag{2-17}$$

With some boundary conditions, equation (2-17) can be used to derive the Gaussian dispersion equation, which will be discussed in the following chapter.

FLUENT solves the pollutant transportation equation at the wall as follows:

$$Y^* \equiv \frac{(Y_{i,\omega} - Y_i)\rho C_\mu^{1/4} k_P^{1/2}}{J_{i,\omega}} = \begin{cases} S_c y^* & (y^* < y_c^*) \\ Sc_t[\frac{1}{k} ln(E\, y^*) + P_c] & (y^* > y_c^*) \end{cases} \quad (2\text{-}18)$$

where Y_i is the local pollutant mass fraction;

$Y_{i,w}$ is the local pollutant mass fraction at the wall;

S_c and Sc_t are molecular and turbulent Schmidt numbers;

$J_{i,\omega}$ is the diffusion flux of pollutant i at the wall;

P_c is calculated from Jayatilleke (1969);

y_c^* is the dimensionless height at which the linear and logarithmic concentration profiles intersect;

E is the empirical constant for smooth wall (=9.81);

k_p is the turbulent kinetic energy at point P.

The default turbulent Schmidt number in FLUENT 6.1 is 0.7. This does not fit for all cases (Tang, 2005; Flesch, 2002; Koeltzsch, 2000; He 1999), but it could be changed in order to get the correct turbulent diffusion coefficient in the individual case, which will affect the plume dispersion. In the following chapters, the effects of this number will be examined.

2.5 Generalized Discretized Equations

If we introduce the general variable ϕ, the conservative form of all fluid flow equations under steady state, including equations for the scalar quantities such as k, ε and pollutant concentration, can be written in the following form by using the control volume formulation:

$$div(\rho\phi U_j) = div(\Gamma_\phi \, grad\phi) + S_\phi \tag{2-19}$$

where Γ_ϕ is the diffusion coefficient and S_ϕ is the source term.

The first term is the net flux of ϕ due to convection into the control volume; the second term is the net flux of ϕ due to diffusion into the control volume; and the third term is the net rate of creation of ϕ inside the control volume.

1) For the continuity equation (2-4), $\phi = 1$, $\Gamma_\phi = 0$ and $S_\phi = 0$

2) For the momentum equation (2-7), $\phi = U_i$, $\Gamma_\phi = (\mu + \mu_t)$ and $S_\phi = \frac{\partial}{\partial x_i}(-P)$

3) For the realizable k equation (2-10), $\phi = k$, $\Gamma_\phi = (\mu + \frac{\mu_t}{\sigma_k})$ and $S_\phi = G_k - \rho\varepsilon$

4) For the realizable ε equation (2-11), $\phi = \varepsilon$, $\Gamma_\phi = (\mu + \frac{\mu_t}{\sigma_\varepsilon})$ and

$$S_\phi = \rho C_1 S\varepsilon - \rho C_2 \frac{\varepsilon^2}{k + \sqrt{\nu\varepsilon}}$$

5) For the pollutant transportation equation (2-16), $\phi = Y_i$, $\Gamma_\phi = (\rho D_{i,m} + \frac{\mu_t}{Sc_t})$ and

$$S_\phi = 0$$

2.6 CFD Simulation Procedure

A CFD simulation procedure includes the following parts:

- Pre-processor
- Solver
- Post-processor

2.6.1 Pre-processor

The pre-processor performs the following functions:

1) Selection of the physical phenomena that need to be modeled;
2) Definition of the geometry of the region of interest: the computational domain;
3) Grid generation: sub-division of the domain into a number of smaller, non-overlapping sub-domains: a grid (or mesh) of cells (or control volumes or elements);
4) Specification of appropriate boundary conditions at cells which coincide with or touch the domain boundary.

In this study, pre-processing is done by the commercial software GAMBIT 2.0.

2.6.2 Solver

A solver contains the procedures to get the solution of the equations. FLUENT 6.1 provides two solvers: a segregated solver (Fig. 2.1) and a coupled solver.

The differences between these two solvers are associated with the way that they solve the continuity equation, the momentum equation and the energy equation or pollutant

transportation equation. The segregated solver solves these equations in sequence, while the coupled solver solves these equations simultaneously. The segregated solver is usually used for incompressible and mildly compressible flows, while the coupled solver is usually used for high speed compressible flows (Fluent 2003). In this thesis, the segregated solver is used.

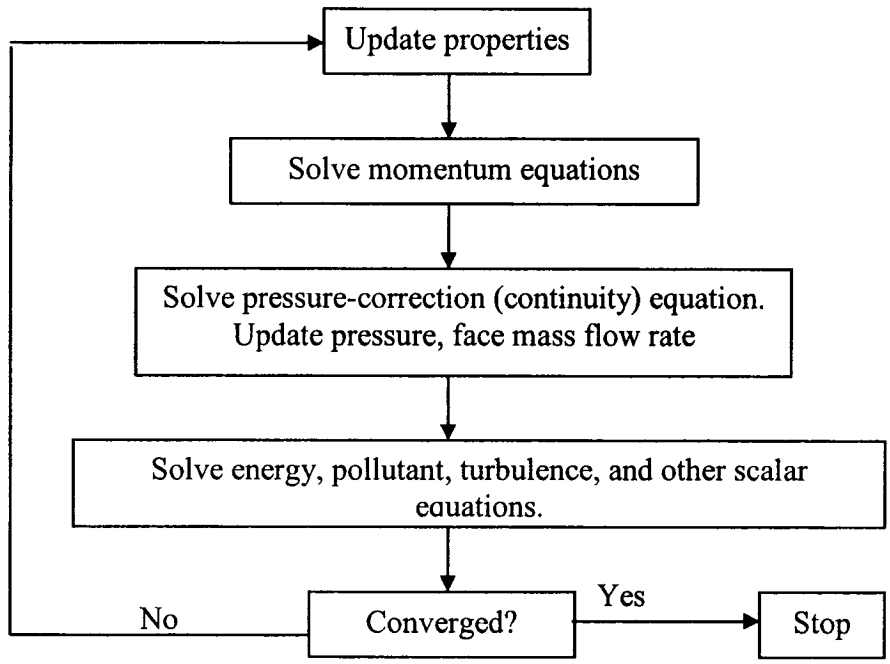

Figure 2.1 Flow Chart of Segregated Solver

FLUENT 6.1 uses a co-located scheme, whereby pressure and velocity are both stored at cell centers. The standard pressure interpolation scheme in this study uses momentum equation coefficients (Rhie, 1983).

The SIMPLE (Semi-Implicit Method for Pressure-Linked Equations) scheme (Patankar, 1980) and SIMPLEC scheme (Vandoormaal & Raithby, 1984) are used for introducing pressure into the continuity equation in this study.

It should be noted that the magnitude of the discretization error decreases as the order of the discretization scheme increases. However, the computational process tends to become more unstable as the order increases. The errors caused by the discretization depend on the mesh type (Ferziger & Peric, 1999).

The transported property ϕ at the grid faces is needed to be solved by using the following schemes in FLUENT 6.1:

1) First order discretization schemes: first order upwind, POWER LAW

2) Second order discretization schemes: second order upwind, QUICK

The first order upwind scheme considers the effects of the upwind cells on the face value by assuming the face values equal to the upwind cell values, while the POWER LAW scheme uses an exact solution of the one dimension convection-diffusion equation. They both have the first order accuracy. If the truncation error from a discretizaion scheme is proportional to $(\Delta x)^n$, the scheme is usually called an nth-order approximation and its accuracy is called an nth-order accuracy.

The second order upwind scheme considers the effects of the gradient of upwind cells on the face values by using Taylor series expansion of cell-centered solutions, while the QUICK scheme considers the effects of more cells around the face on the face values and is based on a weighted average of second order upwind and central interpolation of the variables. These two schemes have second order accuracy.

A multigrid scheme (Fluent 2003) is used to accelerate solving the Gauss-Seidel linear equations for the 3D domain. The "scaled" residuals for each of the conserved variables are computed at the end of the each iteration (Fluent 2003).

2.6.3 Post-processor

Post-processing implies retrieving graphical and numerical information about the variables from the solution. It includes, but is not limited to:

1) Domain geometry and grid display,

2) Vector and contour plots,

3) Line, 2D and 3D surface plots,

4) Quantitative numerical calculations on specified cells,

5) Particle tracking,

6) View manipulation (translation, rotation, scaling etc).

CHAPTER 3 REVIEW OF STANDARD DISPERSION MODELS

The dispersion models studied in this chapter consist of a set of analytical or empirical formulae, such as Gaussian model and ASHRAE (2003), which use emissions from a point source and meteorological information to predict the concentration distribution. The results of using each of these models consist of the estimated concentrations of plumes at specified locations.

3.1 Gaussian Model

The Gaussian model is the basic model used in predicting pollutant concentration distributions from sources releasing continuously under steady state conditions. The most important assumption is that the time averaged concentration profiles at any distance in the crosswind and vertical direction well are represented by a Gaussian distribution.

Considering ground reflection, the most general form of the Gaussian dispersion equation is presented as (Turner, 1994)

$$\frac{\chi(x,y,z;H)u}{q} = \frac{\exp(-y^2/2\sigma_y{}^2)}{2\pi\sigma_y\sigma_z}\{\exp[-\frac{(H-z)^2}{2\sigma_z{}^2}] + \exp[\frac{-(H+z)^2}{2\sigma_z{}^2}]\} \qquad (3\text{-}1)$$

where χ is air pollutant concentration in mass per volume, [g/m^3];

q is pollutant emission rate in mass per time, [g/s];

u is the wind speed at the stack height, [m/s];

σ_y is the standard deviation of the concentration distribution in the crosswind direction at the downwind distance x, [m];

σ_z is the standard deviation of the concentration distribution in the vertical direction at the downwind distance x, [m];.

H is the effective height of the centerline of the plume, [m].

This equation estimates the concentration at the receptor located at x downwind, y crosswind, and at a height, z, above the ground that results from an emission that has an effective height, H, above the ground (Fig. 3.1).

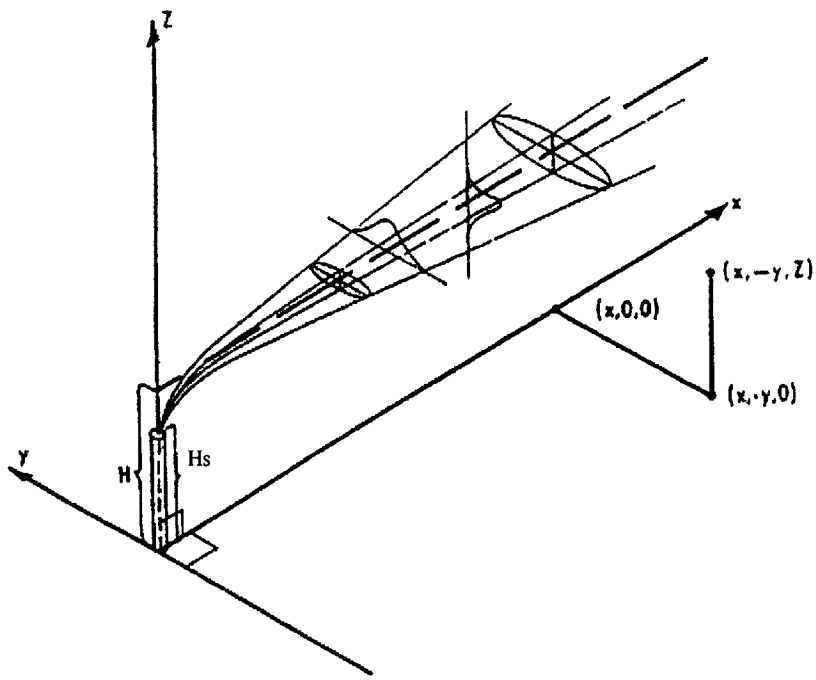

Figure 3.1 Coordinate System Showing Gaussian Distributions in the Horizontal and Vertical Directions (after Turner, 1994)

In order to estimate concentrations directly beneath the plume centerline, $y = 0$, at ground level $z = 0$, the general Gaussian formula (equation (3-1)) further reduces to:

$$\frac{\chi(x,y,z;H)}{q} = \frac{\exp(-H^2 / 2\sigma_z{}^2)}{\pi\sigma_y\sigma_z u} \tag{3-2}$$

To avoid repetitious computations, Turner (1994) has plotted maximum ground level concentration $\chi u / q$ as a function of downwind distance, x, for different emission heights and stability class (see Appendix B)

For other receptor locations, equation (3-1) can be simplified. For example,

1) The crosswind concentration distribution at ground level at downwind distance, x, is given by:

$$\frac{\chi(x,y,0;H)u}{q} = \frac{\exp(-\frac{H^2}{2\sigma_z{}^2})}{\pi\sigma_y\sigma_z}\exp(-\frac{y^2}{2\sigma_y{}^2}) \tag{3-3}$$

2) The crosswind concentration distribution at height H, is given by:

$$\frac{\chi(x,y,H;H)u}{q} = \frac{1+\exp(-2\frac{H^2}{\sigma_z{}^2})}{2\pi\sigma_y\sigma_z}\exp(-\frac{y^2}{2\sigma_y{}^2}) \tag{3-4}$$

3) The vertical concentration distribution along the plume centerline at downwind x, is given by:

$$\frac{\chi(x,0,z;H)u}{q} = \frac{\exp(-\frac{(H-z)^2}{2\sigma_z{}^2}) + \exp(-\frac{(H+z)^2}{2\sigma_z{}^2})}{2\pi\sigma_y\sigma_z} \tag{3-5}$$

The effective height of a plume is defined as:

$$H = H_s + h_r - h_d \tag{3-6}$$

where H_s is the physical stack height, h_r is the plume rise, and h_d is the stack wake downwash. $h_d = A_1 d\,(1.5 - \beta V_e / u)$ where the constant $A_1 = 1.0$ for $V_e / u \leq 1.5$ and $A_1 = 0$ for $V_e / u > 1.5$. V_e / u is the ratio of exhaust velocity to wind speed at the stack height, and d is the stack internal diameter. The parameter, β, is set equal to 1.0 for uncapped stacks.

Plume rise, h_r, is produced by the exhaust momentum and buoyancy. In the present study, the stack exhaust has the same density as ambient air. Therefore, the buoyancy component of h_r is zero. The maximum plume rise due to exhaust momentum for a bent-over jet under Pasquill's neutral stability is (Briggs, 1984)

$$\Delta h_{\max} = 3\beta d\, V_e / u \tag{3-7}$$

A few important empirical parameters (such as plume spread factors σ_z, σ_y) in the Gaussian model strongly affect plume dispersion. Originally, these empirical parameters were calculated from field test results because they are dependent on many factors, such as atmospheric stability, wind speed, downwind distance, stack height, and sampling time (Arya, 1999). Here, these factors are evaluated according to Pasquill stability classes (Appendix B, Turner 1994).

The Gaussian model is used by the U.S. EPA as a regulatory model and its accuracy is sufficient for many applications. However, it only works well in situations having

uncomplicated transport and diffusion between sources and receptors (Pasquill and Smith, 1983, Huber and Synder, 1982).

In many cases, the main interest is the concentration level close to a building or even on the building wall where fresh air intakes are often located. The complexity of building wakes and resulting downwash problems severely limit the use of the Gaussian plume model. Suggested conditions for adjusting dispersion equations to the basic Gaussian model were given by Huber and Snyder (1982), who found that the receptor in the Gaussian model was limited to be not very close to the buildings (e.g., within three building heights) and the wind direction was assumed to be approximately normal to the front face of the building.

3.2 Empirical Formula

The first attempt to predict the pollutant concentration on building surfaces was made by Halitsky (1963). Using Gaussian diffusion theory, he developed a minimum dilution model for block-shaped buildings with a short roof-top stack based on wind tunnel experiments.

A number of models for estimating the minimum dilution on building surfaces have been recommended by ASHRAE. Minimum dilution is defined as the ratio of contaminant concentration at the exit point of the exhaust to the maximum concentration on the plume centerline at the roof level.

ASHRAE (1999) recommended the minimum dilution model formulated by Wilson and Lamb (1994). In this model, minimum dilution along the plume centerline is given by:

$$D_{\min} = (D_0{}^{0.5} + D_d{}^{0.5})^2 \tag{3-8}$$

where D_0 is the initial dilution at the location and D_d is the distance dilution which is produced by atmospheric and building-generated turbulence.

The formulas for D_0 and D_d are:

$$D_0 = 1 + 13M \tag{3-9}$$

$$D_d = B_1 S^2 / MA_e \tag{3-10}$$

where A_e $(=\frac{1}{4}\pi d^2)$ is the exhaust area; B_1 is the distance dilution parameter; S is determined by measuring the length of a string stretched between the stack and the receptor and M is the ratio of exhaust gas velocity to the undisturbed mean wind speed taken at the building height.

Dilution data obtained in a field study (Wilson and Lamb, 1994) and a wind tunnel study (Wilson & Chui, 1987) indicated that the parameter, B_1, in this model was strongly affected by the level of atmospheric turbulence in the approaching flow. The effect of upstream turbulence on the distance dilution parameter is approximated by the following formula for rooftop receptors:

$$B_1 = 0.027 + 0.0021\sigma_\theta \tag{3-11}$$

where σ_θ is the standard deviation of the horizontal wind-direction fluctuations in degrees and varies between 0^0 and 30^0. For an urban environment, ASHRAE (1997) recommended a typical value of $\sigma_\theta = 15^0$, which gives a value of 0.032 for the atmospheric component of the distance dilution parameter, yielding $B_1 = 0.059$.

The $D_{\min}$ model above is applicable for flush vents or cases where the stack is lower than the maximum roof elevation.

ASHRAE (2003) recommended a Gaussian-based model for predicting the worst-case dilution at roof level from a vertical stack. Fig. 3.2 shows the flow recirculation regions and exhaust-to-intake stretched-string distances, recommended by ASHRAE (2003).

The roof-level dilution for a plume at height, H, at a receptor distance, x, from the stack is given as:

$$D_r = 4 \frac{U_{Hb}}{V_e} \frac{\sigma_y}{d} \frac{\sigma_z}{d} exp\left(\frac{H^2}{2\sigma_z{}^2}\right) \tag{3-12}$$

where U_{Hb} is the undisturbed wind speed at the building height, d is the internal stack diameter, V_e is the exhaust speed, σ_y and σ_z are the plume spreads in the horizontal and vertical directions, respectively, H is the effective plume height (Fig. 3.2) and $h_d = A_1 d\,(3.0 - \beta V_e / u)$ where the constant A_1 = 1.0 for $V_e / u \leq 3.0$ and A_1 = 0 for $V_e / u > 3.0$.

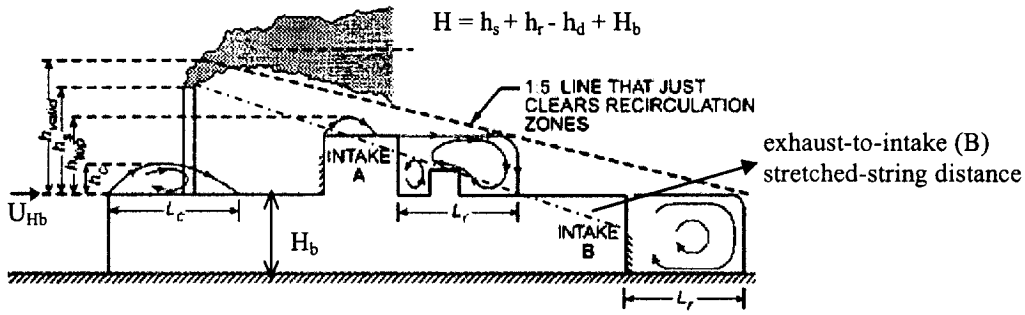

Figure 3.2 Flow Recirculation Regions and Exhaust-to-Intake Stretched-String Distances (after Wilson 1982)

As for plume spread parameters, ASHRAE (2003) recommended equations based on full-scale atmospheric measurements by McElroy & Pooler (1968) in an urban area, as used in the EPA (1995) model ISCST. The urban ISCST equations are adjusted here from the 60 min measured averaging time to 2 min averages with the 0.2 power law applied to both vertical and cross-wind spreads. Then, the vertical spread over a building roof is assumed to remain constant at the 2 min averaging time value for longer averaging times.

The plume equations are:

$$\frac{\sigma_y}{d}=0.071(\frac{t_{avg}}{2.0})^{0.2}\times\frac{x}{d}+\frac{\sigma_0}{d} \tag{3-13}$$

$$\frac{\sigma_z}{d}=0.071\times\frac{x}{d}+\frac{\sigma_0}{d} \tag{3-14}$$

where t_{avg} is the concentration averaging time in minutes, x is the distance downwind from the stack, and σ_0 is the initial source size that accounts for stack diameter and for dilution jet entrainment of ambient air during plume rise.

The dependence of initial spread σ_0 on exit velocity to wind speed ratio $\frac{V_e}{U_{Hb}}$ is

$$\frac{\sigma_0}{d}=[0.125\beta\frac{V_e}{U_{Hb}}+0.911\beta(\frac{V_e}{U_{Hb}})^2+0.250]^{0.5} \tag{3-15}$$

where β is the rain cap factor: $\beta = 1$ for no rain cap, and $\beta = 0$ if there is a rain cap.

For exhaust grills and louvers on the roof or walls of a building or penthouse, exhaust height $H = 0$, equation (3-12) becomes

$$D_s=4\frac{U_{Hb}}{V_e}(0.071(\frac{t_{avg}}{2.0})^2\frac{S}{d}+\frac{\sigma_0}{d})(0.071\frac{S}{d}+\frac{\sigma_0}{d}) \tag{3-16}$$

where the stretched string distance S between the nearest edges of the exhaust to the nearest edge of the intake replaces the horizontal distance x in the cross wind and vertical plume spreads in equation (3-13) and (3-14).

CHAPTER 4 PREVIOUS APPLICATIONS

4.1 Introduction

Fig. 4.1 shows the complexity of the flow pattern around a typical building and its effect on the plume distribution. The flow impinges on the upwind wall and separates at the sharp edges to generate recirculation flow zones that cover the downwind surfaces of the building (roof, sides, and leeward walls) and extend for some distance into the wake. The stagnation point is generated on the windward surface at one half to two thirds height of the building. Depending on the building length, L, and turbulent characteristics of the approaching flow, the flow may or may not reattach to the building roof and side wall. If a stack is located at the center of the roof, the emissions from the stack could be carried into the wake of the building and on the leeward wall by the circulating zone. This could affect the quality of air inhaled by the pedestrians and indoor air quality from the fresh air intakes on the leeward wall.

A vortex generated in front of the building causes high wind speed close to the ground. This upwind vortex is carried around the sides of the building in a U shape and is responsible for the suspension of dust and debris that can contaminate air intakes close to the ground level.

This chapter will review the literature on the following applications:

1) Predicting air flow around buildings;

2) Predicting plume dispersion from sources on or above the roof;

3) FLUENT software applications in the wind-induced dispersion of pollutants.

4) Justification of the present study

Note that the review is focused on previous works using CFD numerical simulation for the wind flow field and dispersion around a building. Although many wind tunnel and field studies were conducted and many empirical models have been proposed, only those used as the validation or comparisons to the present CFD works are reviewed here.

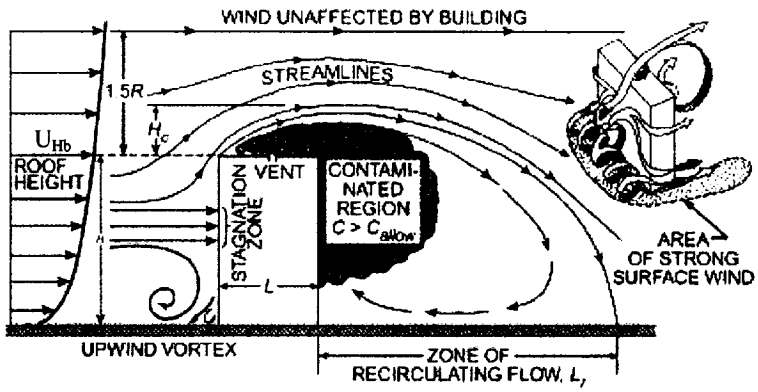

Figure 4.1 Flow Patterns and Plume Distribution around a Typical Building (L is the length along the wind, R is the scaling length, H_c is the recirculation region height, after ASHRAE, 2003)

4.2 Air Flow around an Isolated Building

4.2.1 Wind Tunnel Testing

An experimental investigation of the flow around a cube in both uniform and sheared, turbulent flows was described by Castro & Robins (1977). The shear flow was a simulated atmospheric boundary layer that was ten times the height of the building (h is 200 mm). The clear effect of upstream turbulence and shear on the flow around the building is described in Fig. 4.2. For the uniform upwind flow, there was no attachment

to the roof surface and side walls. However, for the sheared upstream wind, the flow re-attached to the roof surface. The wake flow was also strongly affected by upstream turbulent characteristics. The greater turbulence intensity in the sheared approaching flow also increased the recovery rate of the wake flow to the upstream condition.

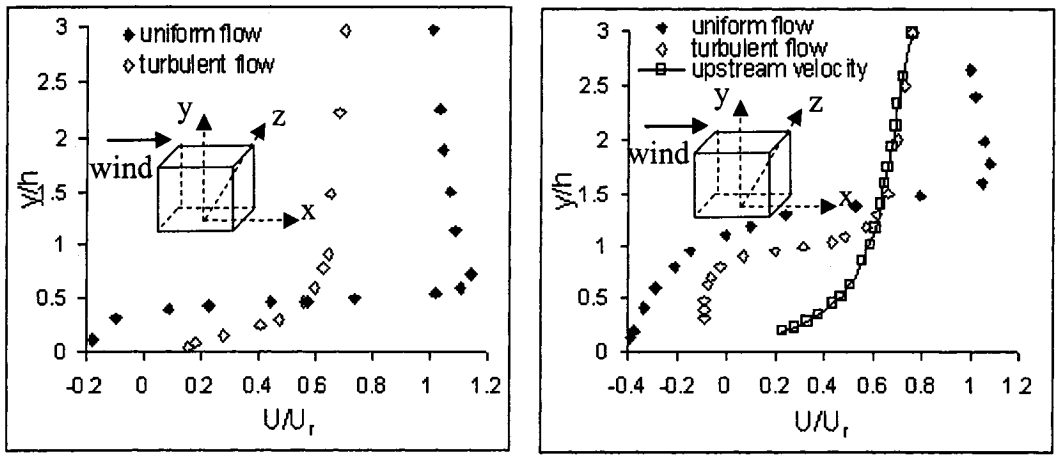

Figure 4.2 Mean Velocity Variations (a) at the Top of the Building (x/h = 0, y/h varies and y/h >1, z/h = 0) (b) in the Wake of the Building (x/h = 1, y/h varies, z/h = 0) (U_r is the free stream wind flow and h is the building height, after Castro & Robins, 1977)

Snyder & Lawson (1994) simulated flow fields around the rectangular-shaped blocks in the EPA meteorological wind tunnel. They used a cubical building with dimensions of 200 mm immersed in a simulated 2-m deep atmospheric boundary layer as a basic case study. The wind direction is normal to the building. Then four series experimental tests were conducted to see the flow field reactions with various building dimensions. In the first series, they increased the crosswind dimension of the building to 2, 4, and 10 times that of the cube. In the second series, they increased the along-wind lengths of the building to 0.015, 0.5, 1, 2 and 4 times that of the cube. In the third series, the height of the building was increased to 2 and 3 times that of the cube. Finally, wind direction was

rotated 45^0 for the cubical building. It was found that the location of the stagnation point on the upwind wall of the building was independent of the crosswind width or along-wind length of the building. The flow reattached on the roof when the along-wind length is equal or larger than the height of the building. Thus the cavity length and height behind the building is smaller in both cross wind and stream wise directions as the building length in the stream wise direction increased. The cavity length and height grew as the crosswind width of the building increased.

Snyder (2005) continued to test the flow patterns around the building with more various building dimensions and more various wind oblique directions. These data give more detailed flow structure around the building and are very useful to the prediction of dispersion of plumes released in the vicinity of buildings.

4.2.2 Empirical Model

Wilson (1979) found that for a flat-roofed building, the upwind roof edge recirculation region height, H_c, at location, X_c, and recirculation length, L_c, are given by the following equations (Fig. 4.3):

$$H_C = 0.22R,\ X_C = 0.5R,\ L_C = 0.9R,\ L_r = R \tag{4-1}$$

where the scaling length R is:

$$R = B_S^{0.67} B_L^{0.33} \tag{4-2}$$

where B_S is the smaller of upwind building face dimensions H_b and W and B_L is the larger of upwind building face dimensions H_b and W.

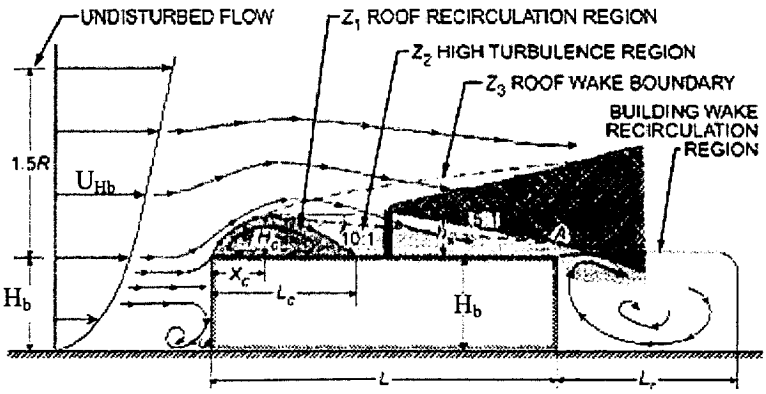

Figure 4.3 Wind Recirculation Zones on the Flat-Roofed Building (after Wilson (1979))

The boundary of the high-turbulence region Z_2 is approximated by a straight line sloping at 10:1 which begins from the top of the maximum cavity height, and it is given by

$$\frac{Z_2}{R} \approx 0.27 - 0.1\frac{x}{R} \tag{4-3}$$

The roof wake boundary Z_3 is given by

$$\frac{Z_3}{R} \approx 0.28\left(\frac{x}{R}\right)^{\frac{1}{3}} \tag{4-4}$$

Hosker (1979, 1980) has developed the following empirical formulae for wake cavity length (L_r):

$$\frac{L_r}{H_b} = \frac{A(W/H_b)}{1 + B(W/H_b)} \tag{4-5}$$

where, for $L/H_b < 1$, $A = -2.0 + 3.7\left(\frac{L}{H_b}\right)^{-\frac{1}{3}}$, $B = -0.15 + 0.305\left(\frac{L}{H_b}\right)^{-\frac{1}{3}}$

and for $L/H_b \geq 1$, A = 1.75, B = 0.25

The dimensions of the recirculation zones are somewhat sensitive to the intensity and scale of turbulence in the approaching wind. High levels of turbulence from upwind

obstacles can decrease the coefficients in the above equation. For several applications, the empirical model is easy to use, but it is only a guide for predicting the air flow field around buildings. It is not suitable for predicting the dimensions of the air flow field around buildings for more complex cases and it is applicable only for winds that are approximately normal to the building.

4.2.3 CFD Modeling of Airflow around an Isolated Building

Over the last two decades, computational wind engineering, as a branch of computational fluid dynamics, has been developed rapidly to simulate the airflow around buildings. Various researchers have obtained relatively good results in regions where flow is attached to a building surface. For the calculations of recirculation zones around the building and the shear layer separating from the front sharp edge, the good agreements with experimental data are difficult to be achieved.

Murakami & Mochida (1989) simulated three-dimensional air flow around a cubic model and building complex using the standard $k-\varepsilon$ model. They concluded that the mesh resolution and the boundary conditions of ε at the solid wall had a significant influence on the flow field in the separation region above the roof and on the flow near the side walls at windward corners. They also concluded that the $k-\varepsilon$ model with a fine mesh can reproduce more accurate mean velocity field and mean pressure field than a coarse mesh compared with wind tunnel tests. However, significant differences were observed in the distribution of the turbulent energy (k) around the windward corner and in the wake.

Stathopoulos & Baskaran (1990) evaluated wind effects around buildings through the individually developed code, TWIST. The validity of the standard $k-\varepsilon$ models was

judged questionable in recirculation and separation regions. To improve the results, two simple modifications of the standard $k-\varepsilon$ turbulence models were applied in the calculations, namely, a streamline-curvature correction and preferential-dissipation correction. A new zonal-treatment procedure was developed to bridge the solid boundary nodes with the computational domain for the turbulence variables (k and ε).

More detailed time averaged flow fields around a cube within a surface boundary layer using three types of well known turbulence models, namely the $k-\varepsilon$ eddy viscosity model, the algebraic stress model (ASM), and the LES model, were given by Murakami et al. (1992). The model equations used for ASM were based on the methods of Rodi (1976) and Gibson & Launder (1978), except for the treatment of the wall reflection term (Murakami et al. 1990). The accuracy of these simulations was assessed by comparison with results from wind tunnel tests. The results of LES showed the best agreement with the experimental data. Detailed comparisons with experimental data were provided for the following parameters: k, G_k (production of kinetic energy) and diagonal component of strain rate (Fig. 4.4, 4.5 and 4.6).

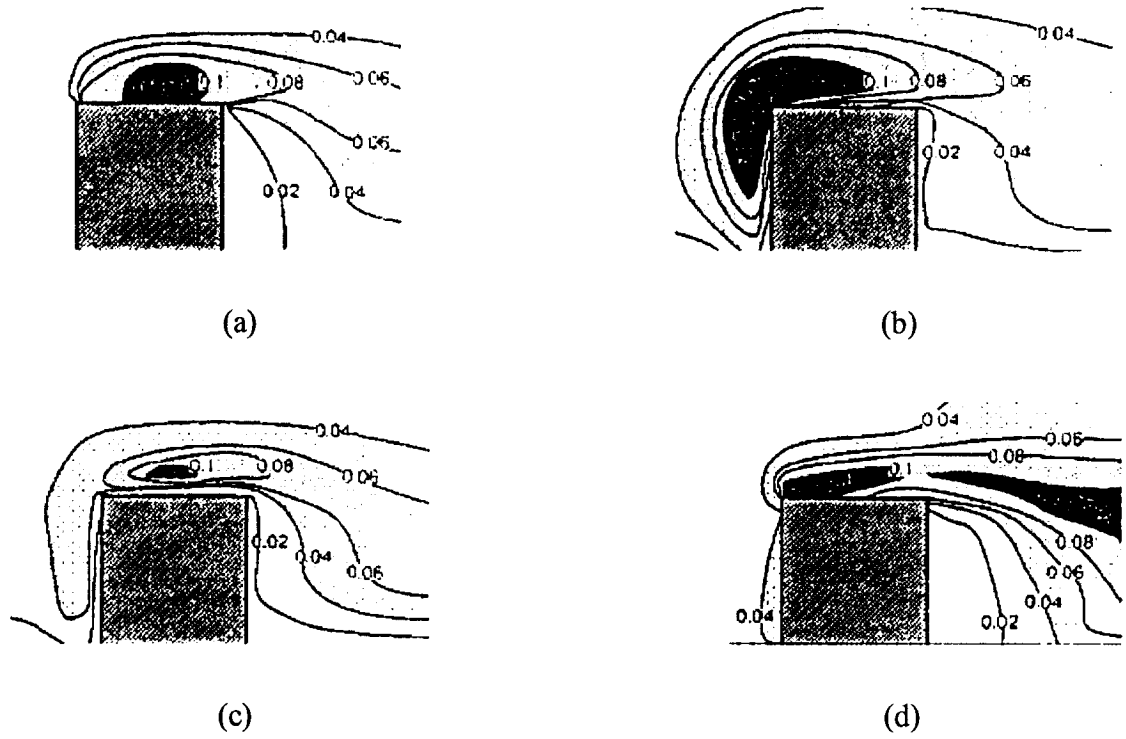

Figure 4.4 Comparison of k between (a) Wind Tunnel Tests (b) k - ε Model (c) ASM Model (d) LES Model (after Murakami et al., 1992)

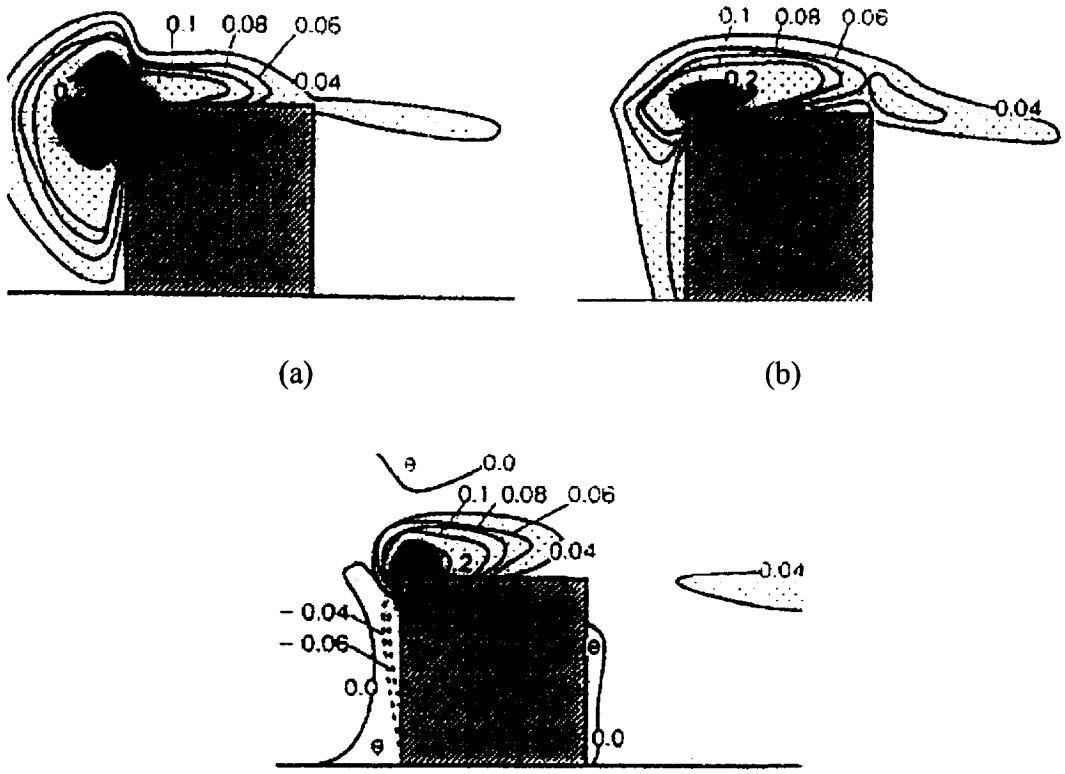

Figure 4.5 Comparison of Production of k between (a) k - ε Model (b) ASM Model (c) LES Model (after Murakami et al., 1992)

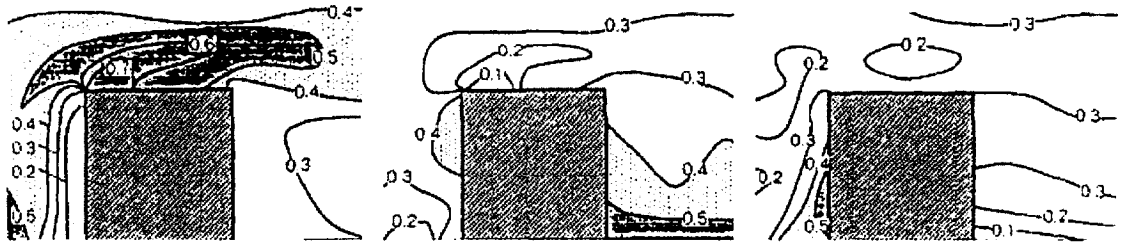

(1) Experiment

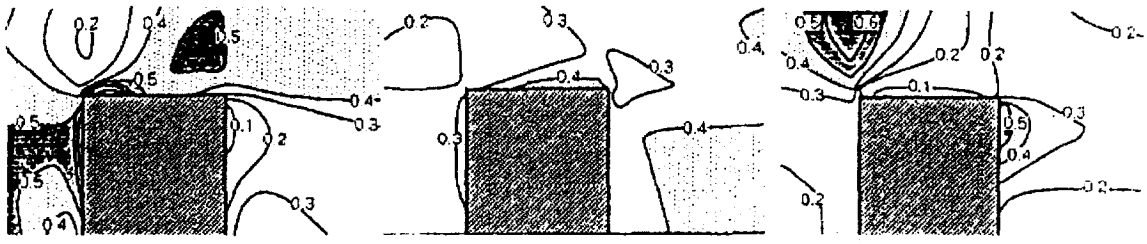

(2) ASM

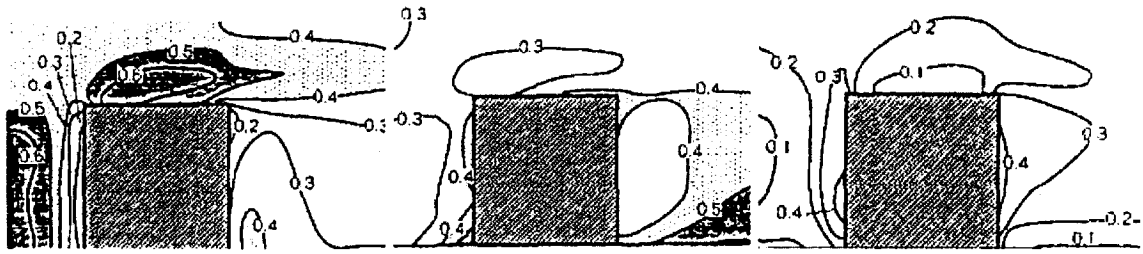

(3)LES

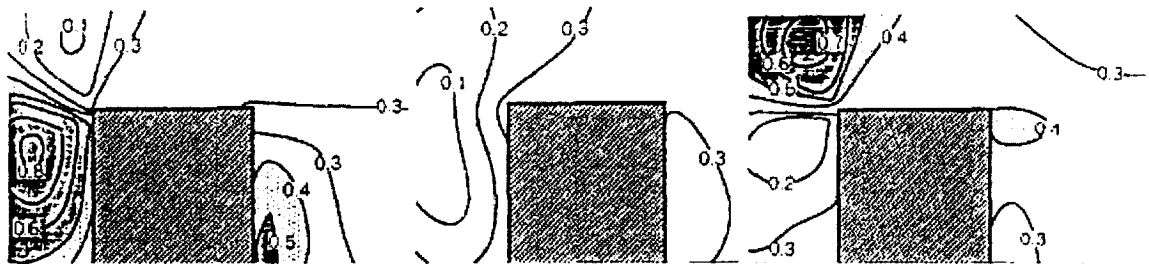

(4) k-ε Model

(a) (b) (c)

Figure 4.6 Comparison of Diagonal Components (a) $\overline{u_1'^2}/2k$ (b) $\overline{u_2'^2}/2k$ (c) $\overline{u_3'^2}/2k$ between Numerical Model Results and Experimental Data (after Murakami et al., 1992)

Stathopoulos & Zhou (1993) proposed a two-layer methodology combining the $k-\varepsilon$ model in the external flow region with either a one-equation model (Norris & Reynolds, 1975), or a modified $k-\varepsilon$ model (Lam & Bremhorst, 1981), in the near wall area. This two layer method based on the one equation model had been found effective in predicting the separation above the roof surface and near the side walls of a cubic building.

Lakehal & Rodi (1997) also proposed a two-layer approach with a one-equation model and calculated the flow past a surface mounted cube. The various predictions were compared with the measurements of Martinuzzi and Tropea (1993). It was found that the one-equation model, due to Norris and Reynolds, with two-layer approach was much more effective than the modified $k-\varepsilon$ models by Kato–Launder (1993), which aimed to reduce a high production of k in the stagnation regions occurring in the impinging flows.

The overestimated kinetic energy around the leading edge of the building is mainly caused by linear viscosity model in Bossenique's assumption. Non-linear viscosity model was tested by Ehrhard et al. (2000). They found that the model proposed by Lien et al. (1996) showed better results than those from standard $k-\varepsilon$ model in comparison to experimental tests by Martinuzzi and Tropea (1993). The CPU time effort is 15% to 20% larger than that for the linear viscosity model. However, there is still large discrepancy between the numerical results by the non-linear viscosity model and experimental data in the wake region.

As mentioned in Chapter 2, Reynolds stress model includes the anisotropy character of fluid flow by solving additional exact stresses transportation equations. Meroney et al. (1999) compared recirculation zones around several building shapes using standard $k-\varepsilon$ model, RNG $k-\varepsilon$ model and Reynolds stress model in FLUENT 4.2.8. All constants in

these turbulence models are default values in FLUENT. They found that the Reynolds stress model provides a more accurate flow field than other models. Also, their results showed that pressure coefficients on the front, back and rooftop can be predicted very well compared with experimental data even though without accurate recirculation zones around the building. However, no explanations can be found in their paper for this good agreement of pressure coefficients and bad agreement of flow field with experimental data.

In order to improve the overestimated kinetic energy around the leading edge of the building by the standard $k-\varepsilon$ model, Gao & Chow, (2005) proposed a method to change the speed distributions around the sharp corner of the building. By limiting the longitudinal velocities in the first cell adjacent to the sharp edge of the cube and making good use of the wall functions at the intersection cells of the velocity components, the positions of maximum turbulent kinetic energy and the flow separation and reattachment could be predicted by the standard $k-\varepsilon$ model.

In summary, the standard $k-\varepsilon$ model overestimates the kinetic energy around the leading edge of the building and thus it underestimates both the length and height of the recirculation zone on the top of the building. Some modified $k-\varepsilon$ models can overcome this drawback. Because theoretically non-linear models and Reynolds stress model (RSM) are more accurate than linear models ($k-\varepsilon$ models), these models are recommended, although these still require improvements. Moreover, compared with the LES model, RSM and non-linear models need much less computational resources.

4.3 CFD Modeling of Dispersion around an Isolated Building Using Individually Developed Code

Although many wind tunnel and field tests of effluent plumes emitted from the rooftop of the building were conducted (Meroney, 2004), only previous CFD applications are focused on in this section.

Zhang et al. (1996) examined the flow field and dispersion patterns around a cubical building under neutral and stably stratified atmospheric boundary layer flow using a $k-\varepsilon$ model (TEMPEST). They studied the effect of turbulent diffusivity to the concentration field and found anisotropic turbulent mass diffusivity with $K_{xx} = 0$ and $K_{yy} = 1.4\ K_{zz}$ gave a better estimation of the dispersion around a building in neutral atmospheric boundary layer flow. However, in strongly stable flow around a building, turbulent mass diffusion becomes less important. In their study, turbulent Schmidt number is set to 0.77.

Castro & Apsley (1997) computed flow and dispersion over two-dimensional hills with various slopes under neutrally stable atmospheric boundary layer. The modified $k-\varepsilon$ model showed good agreements for the mean flow, but produced lower values for the turbulent kinetic energy and the lateral plume spread. The resulting "terrain amplification factors" were in good agreements with the experimental data. In their study, turbulent Schmidt number was set to 0.9.

Li and Stathopoulos (1997) evaluated air pollutant distribution around a building by using an individually developed CFD code based on the TWIST code. The basic pollutant transport equation is the same as equation (2-16) with turbulent Schmidt number 0.7.

Numerical results agreed well with experimental data for positions far downwind of the building, but agreed less satisfactorily for positions close to the wall and within the wake zone.

Hanna et al. (2004) estimated the flow and dispersion around an L-shaped building using FLACS CFD air quality model. Neutral atmospheric boundary layer was assumed and steady state solution was achieved. Predicted cross wind and vertical concentration profiles downwind of the lee edge of the building (at a distance of the height of the building) were compared with the wind tunnel test data. In general, 72% of the predictions are within a factor of two of the wind tunnel data. The median value of the ratio of experimental data over numerical data is 1.55, implying about a 35% under prediction.

4.4 FLUENT Applications in Wind-Induced Plume Dispersion

Today, a number of commercial CFD packages are available on the market. These packages have more powerful functions compared with individually developed CFD codes for several applications. FLUENT 6.1 was chosen for the present study. With unstructured and structured mesh generations, many turbulence models, enhanced wall treatment and an advanced solver for 2D and 3D problems, FLUENT 6.1 can solve complicated fluid problems in wind engineering and industrial aerodynamics. However, the results should be carefully validated by field tests or wind tunnel measurements (Franke, 2005).

As a first step, homogenous atmospheric boundary layer should be checked using FLUENT. Riddle et al. (2004) found that FLUENT can give homogenous mean velocity profiles, but underestimated the turbulent kinetic energy and dissipation rate using the $k-\varepsilon$ model. However, Reynolds stress model can improve the prediction of turbulent kinetic energy and dissipation rate. On average, the turbulent kinetic energy was within 80% of the expected values for heights greater than 100 m, but reduced to 50% of the expected values at the ground level.

Blocken (2004) concluded that the discrepancy is due to the incompatibility of the ABL velocity profile and the log law wall function in FLUENT. He recommended two methods to solve this problem. One is to match the wall function modified for the roughness and the ABL-wind-speed profile; the other is to systematically reduce the turbulent kinetic energy in the inlet profile. Using these methods, he can provide horizontal homogeneity for the wind speed profile but not for the turbulence profiles.

Tang et al. (2005) examined FLUENT capability to predicting the homogenous atmospheric boundary layer. Firstly, the periodic boundary condition was utilized at the inlet to simulate the 2D fully developed horizontal homogenous atmospheric boundary layer, and secondly, they used this generated boundary layer profile as the inlet profile for the dispersion simulation in 3D computational domain. However, they did not compare the produced turbulent kinetic energy and dissipation rate profiles with experimental data. Moreover, this method is very mesh sensitive (Blocken, personal communication).

Dispersion from an isolated stack under neutral open country atmospheric boundary layer was studied by Flowe (1997), Riddle et al. (2004) and Tang et al. (2005). Flowe (1997) simulates the buoyant plume from a power plant and compared her data with Snyder

(1992). She claimed FLUENT gave ground level concentrations 5 times larger than experimental data. Riddle et al (2004) compared pollutant dispersion estimates obtained from FLUENT 6.1 with results obtained from ADMS, the European Gaussian-based dispersion model. In FLUENT, he solved the Euler scalar transportation equation (AD model) with turbulent Schmidt number 0.3 and Lagrangian trajectory equations (LP model) for passive plume concentrations. It was found that the LP model compared better with ADMS data than the AD model, but it needs much larger running times. Therefore, it could not be considered as an appropriate alternative to a model such as ADMS in this case. They suggested that CFD method could be used in the more complex geometry, which could not be simulated by ADMS.

Tang et al. (2005) used FLUENT 6.2 to simulate short range dispersion of a plume from a ground level source in an open field. Results were compared with field data obtained in Project Prairie Grass (Barad, 1958). They simulated the steady state plume dispersion by the CFD model firstly and then smoothed the steady solution over the spectrum of wind direction fluctuations. The numerical results performed well compared with the field-test results from Project Prairie Grass for centerline concentrations and arc concentrations. They also did a parametric study of turbulent Schmidt number from 0.7, 1.0 to 1.3 and found that the value of 1.0 had the best agreement with the measurements for distances further than 50 meters arc. However, at 50 meters arc, a turbulent Schmidt number of 1.3 performed best. They recommended further work should modify σ_y and σ_θ so that one turbulent Schmidt number can produce good agreements with experimental data at all arc distances. Turbulent Schmidt number is very important for dispersion studies because it characterizes the relative diffusion of momentum and plume mass due to turbulence.

For urban or suburban field, flow patterns around the structure affect the pollutant distribution around it or in its wake. Leitl et al. (1997) studied the flow and dispersion of gases emitted by several point sources located near a U-shape building using the RNG $k-\varepsilon$ model in FLUENT 4.3. It was found that FLUENT gave a mixed image in terms of accuracy of predicted maximum concentrations compared to the wind tunnel experiments. Under the same boundary conditions, for some calculations, numerical results varied mainly in the range of 5 times bigger and 5 times smaller than the corresponding wind tunnel data. However, for some calculations, numerical results were close to one tenth of wind tunnel data.

Meroney et al. (1999) studied flow and dispersion of gases emitted by sources located near different building shapes by using the standard $k-\varepsilon$ model, the RNG $k-\varepsilon$ model, and the RSM in FLUENT 4.4.8. Calculations were compared with wind tunnel measurements. For the airflow field around the building, the RSM turbulence model produced somewhat more realistic results than the standard $k-\varepsilon$ model or the RNG model. However, on the leeward wall, concentrations were consistently over-predicted by more than one order magnitude in comparison with those obtained from experimental tests (as shown in Fig. 4.7.) if conventional Reynolds-averaged type turbulence models were used.

Flowe (1997) also found FLUENT 4.3 overestimated concentrations in the wake of the building. She thought this could be due to underestimated turbulent kinetic energy and mass diffusivity in all directions in the wake of the building. She concluded that although FLUENT is less than a perfect match for all measured parameters in the whole flow field,

it does reveal the treads of variables in the interested areas and will be useful for developing and confirming some future models.

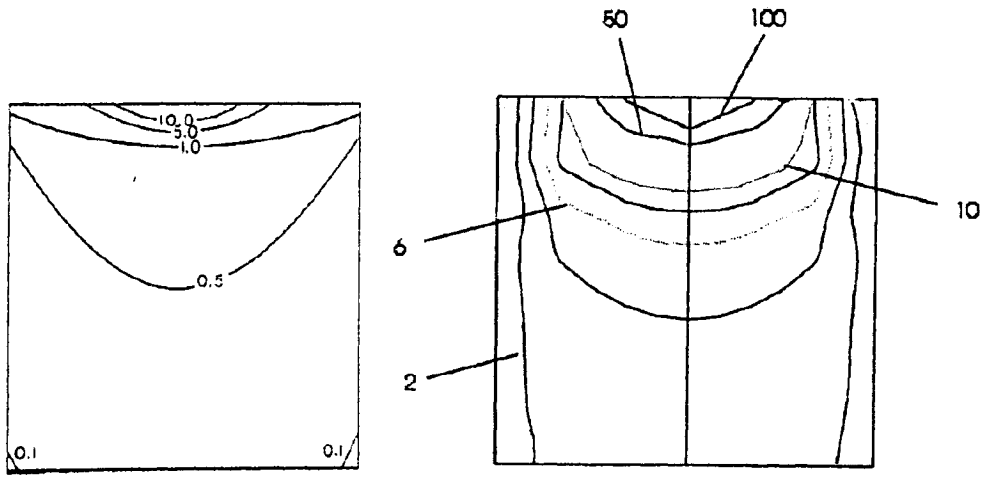

(a) (b)

Figure 4.7 Concentration Isopleths ($K = C U_{ref} H^2 / Q_{source}$) on Back Faces of CSU CUBE Model (source location on rooftop 5/6 of the building height from front edge, after Meroney et al., 1999) (a) Experimental Results (b) Numerical Results

Banks et al. (2003) simulated dispersion of exhaust from a short stack on the rectangular building roof using standard $k-\varepsilon$ model in FLUENT. They compared longitudinal concentration profiles along the plume centerline with experimental data and US EPA SCREEN 3 model. They found CFD calculations overestimated the peak concentration downstream of the stack on the roof and near the top of the rear wall for all cases. The overestimated factors varied from 5 to 10. However, downstream ground level concentrations were predicted well by numerical calculations.

Goricsan et al. (2004) simulated flow fields by using FLUENT 6.1 and pollutant dispersions by using other individually developed code. It was found that numerical simulation results differed significantly from the experimental data, while their trends

remained the same. It was concluded that numerical simulation is a promising method and the properly modeling pollutant emissions is required for accurate results.

4.5 Justification of the Present Study

Computational fluid dynamics (CFD) has been used in wind engineering to simulate flow and dispersion around buildings for several decades. Although results have been unsatisfactory in some cases, CFD shows promising results for a variety of flow situations and is now widely used in some industrial fields.

In the present study, the steady state Reynolds averaged Navier-Stokes equations and several turbulence models, such as standard $k-\varepsilon$ model, realizable $k-\varepsilon$ model, RNG $k-\varepsilon$ model and Reynolds stress model, with several different wall treatments were tested in FLUENT 6.1. A systematic examination of wind-induced dispersion includes dispersion of plumes from an isolated stack under open country condition, from a flush stack located on the roof surface of a cubic building, and from a short stack over the roof surface of a rectangular building with several rooftop structures under urban condition.

CHAPTER 5 DISPERSION OF EXHAUST FROM AN ISOLATED STACK

In this chapter, plume dispersion from an isolated stack, as shown in Fig. 3.1, will be calculated under neutral open country conditions using the Gaussian model and FLUENT 6.1 numerical models. Results were obtained for 2 stack heights, 2 m and 16 m. The numerical results will be compared with the Gaussian models using the spread factors from Pasquill–Gifford (Turner, 1994).

5.1 Numerical Simulation

The general steps during numerical simulation include pre-processor, choosing solver and post-processor. Their definition can be referred to section 2.6.

5.1.1 Pre-processor

Pre-processor is the prepared work for numerical calculation. It includes selection of the related physical phenomena that need to be numerical solved, setting up the computational domain and then appropriate mesh generations for this domain, and setting up the boundary conditions for the governing equations.

1) Selection of the physical phenomena that need to be modeled:

   The physical phenomenon studied here is the pollutant transportation in the atmospheric boundary layer. Equation (2-16) shows that the mean air velocity and the character of turbulence in the ambient air have an effect upon plume dispersion. Under steady state conditions, the convection term on the left of the equation (2-16) is

affected by mean wind speed. The turbulent diffusion term on the right is affected by the turbulent eddy viscosity and the pollutant diffusion coefficient. Therefore the mean air velocity field and turbulent eddy viscosity need to be solved first.

2) Definition of the geometry of the region of interest: computational domain

The layout of the computational domain with stack is shown in Fig. 5.1. The domain size for the 16 m stack height is 1000 x 300 x 200 (m) along the x, y, z directions. Normalizing with respect to stack height, H_s, the domain size is 62.5 H_s x 18.75 H_s x 12.5 H_s. The calculation domain size for the 2 m stack height is 1000 x 200 x 50 (m), or 500 H_s x 100 H_s x 25 H_s. The distance downwind of the stack should be long enough, so that errors caused by the artificial outflow boundary condition imposed on the outlet of the domain will be decreased to a minimum level. For the same reason, the two sides and top of the domain should be far enough from the stack to keep the artificial symmetry boundary conditions. To ensure that the flow at the inlet is not affected by the stack downwind, the inlet should be at least 5 H_s upwind of the stack (Hall, 1997). Following this criterion, the stack position is at least 100 m away from the inlet of the computational domain.

3) Grid generation (Fig. 5.2):

Considering a cylindrical stack in the computational domain, the Hex/Wedge Cooper mesh type was adopted (Riddle et al., 2004). This mesh is composed primarily of hexahedral elements but includes wedge elements where appropriate. The typical elements used are also shown in Fig. 5.2. The number of cells in the domain for the stack height of 16 m was 444,000 and for the stack height of 2 m, it was 467,400. The detailed mesh resolution in x, y, z direction is listed in Appendix C.

FLUENT 6.1 has the ADAPTION function to modify a generated mesh in Gambit. In this study, the adapted function is used around the emission point. After ADAPTION, the total mesh size for a 16 m stack is 758,327, for a 2 m stack it is 591,690.

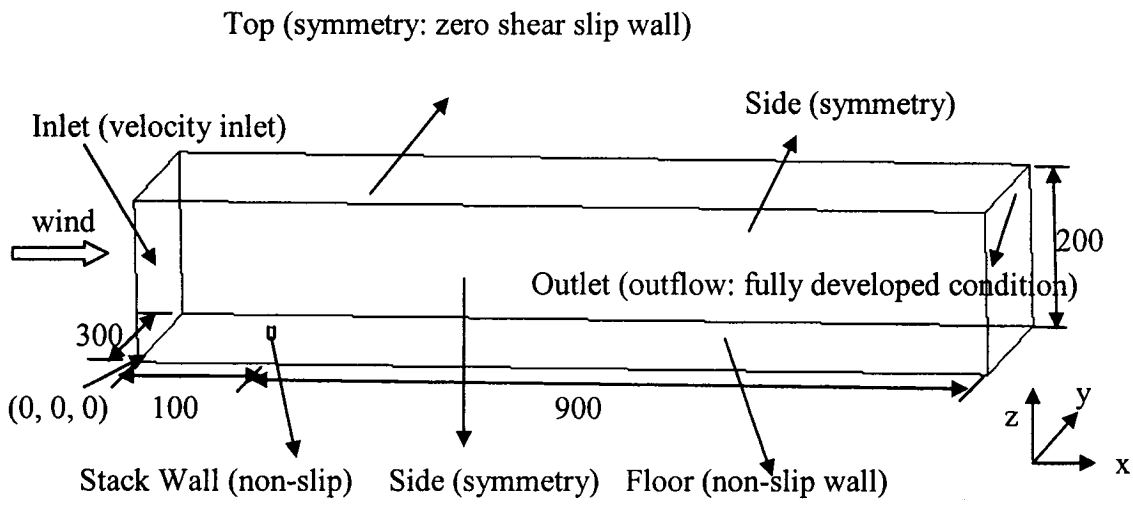

Figure 5.1 Computational Domain and Boundary Conditions for an Isolated Stack

(Note: names outside parentheses are for components of the computational domain and inside are for numerical boundary conditions)

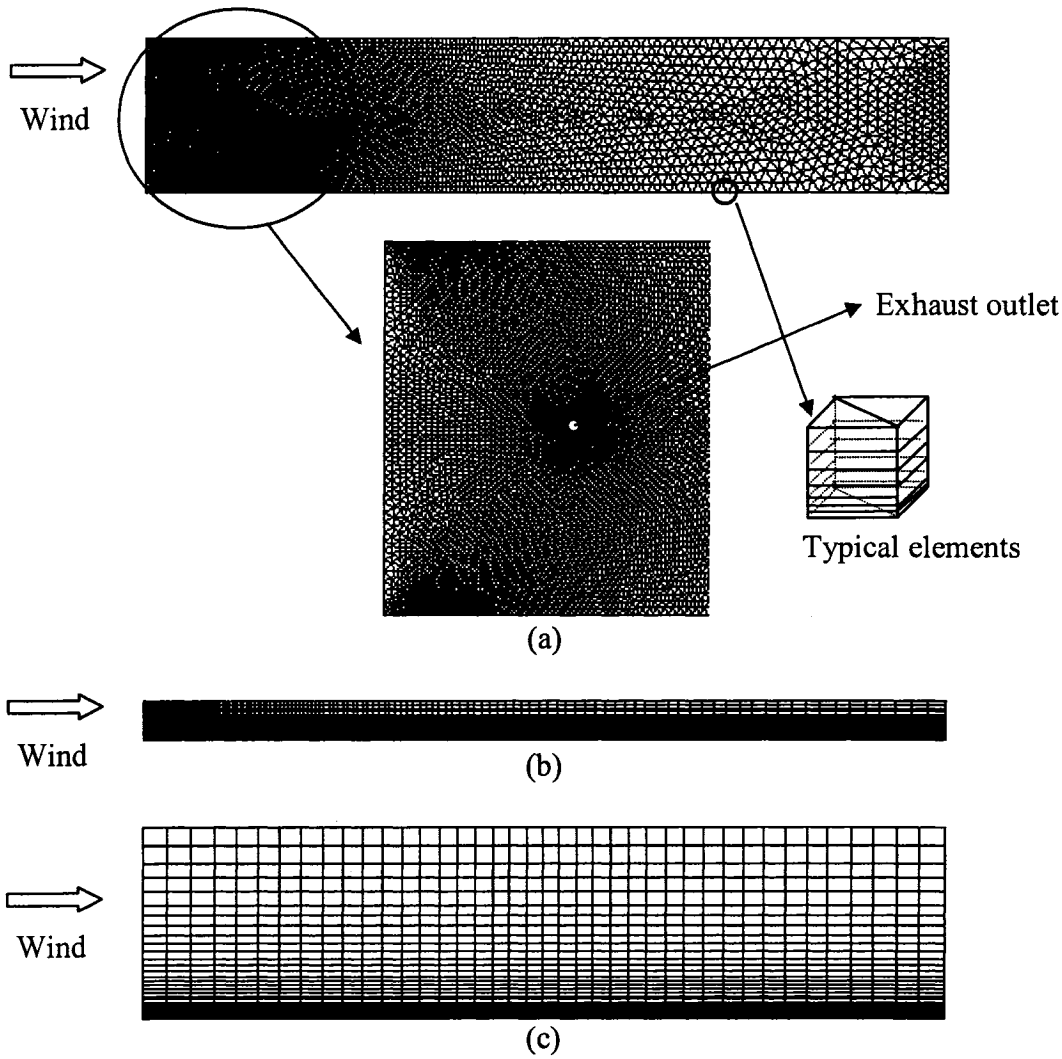

Figure 5.2 Grid Generations for Domain 1000 x 300 x 200 (m) (a) Top View (x - y plane) (b) Side View (x - z plane) (c) Front View (y - z plane)

4) Specification of boundary conditions: (Fig. 5.1)

a) An open country velocity profile $\frac{U(z)}{U(\delta)} = (\frac{z}{\delta})^{\alpha}$ (where $\alpha = 0.14$; $\delta = 270$ m, $U(\delta) = 5$ m/s) was specified at the inlet for the stack heights of 2 m and 16 m. This gives wind speeds of 3.4 m/s and 2.5 m/s at the stack height of 16 m and 2 m respectively.

b) Specified turbulence parameters (k and ε) at the inlet:

The inlet profile by Richards & Hoxey (1993) was used: $k = U^{*2}/\sqrt{C_\mu}$ and $\varepsilon = U^{*3}/(\kappa z)$ (where $U^* = \kappa U(\delta)/ln(\delta/z_0)$) Note that the above constant kinetic energy value is not realistic because in the real atmospheric boundary layer, kinetic energy decreases with height.

There is an incompatibility between the atmospheric boundary layer and the log law wall function in FLUENT 6.1, as mentioned by Blocken (2004) and Blocken et al. (2005). This can lead to horizontal inhomogeneity of the vertical wind speed and turbulence profiles. Blocken (2004) recommended two methods to solve this problem. One is to match the wall function modified for the roughness and the ABL-wind-speed profile; the other is to reduce the turbulent kinetic energy in the inlet profile. In FLUENT 6.1, there is no way to change the wall roughness constant required in the first method. Therefore, the second method of decreasing kinetic energy value from $3.33U^{*2}$ to $1.5U^{*2}$ is used here. Note that this is an imperfect solution. It provides horizontal homogeneity for the wind speed profile but not for the turbulence profiles.

c) The above specified velocity profile and epsilon profile were input into FLUENT 6.1 as a UDF (user defined function) (Fluent, 2003). The detailed programs are listed in Appendix F.

d) The computations simulated a release of SF_6 (sulfur hexafluoride) was released from the position of (100 m, 150 m, 16 m) for the 16 m stack and (100 m, 100 m, 2 m) for the 2 m stack. The exhaust outlet concentration was 10 ppm. The stack

diameter of 0.6 m for the 16 m stack case and 0.2 m for the 2 m stack were arbitrarily chosen.

e) Symmetry was set at the sides and the top of the computational domain, which means no flux passes through these surfaces (the gradient of every parameter is zero).

f) The floor was set to a no-slip wall condition. The physical roughness height k_s is set to 0.03 m and the roughness constant C_{ks} is set to 0.5.

g) Outflow was set at the end of the computational domain.

All the above pre-processing work was done in the commercial software GAMBIT 2.0.

5.1.2 Solver

The segregated solver (Fig. 2.1) was adopted in this case study. Some important parameters are listed here:

1) The standard $k-\varepsilon$ turbulence model was used in all case studies

2) The standard wall function was used to calculate the fluid field near the wall

3) The SIMPLE scheme was used for corrections to the pressure and velocity fields and face mass fluxes

4) QUICK and POWER LAW were used to discretize the convection fluxes and the standard and second order scheme were used to calculate the pressure at each cell face

5) The pollutant transportation equation (2-17) was solved by artificially changing the turbulent Schmidt number to get better agreements with the Gaussian model

5.1.3 Post-processor

Concentration results are expressed in $\chi u/q$ (m^{-2}), where u is the wind speed at release height. The exhaust mass flow rate for the 16 m stack is $q = \rho \times A \times V_e \times C_e = 118.91$ (g/s), for the 2 m stack, $q = 18.9$ (g/s).

$\chi u/q$ is expressed by the Customs Field Functions option in FLUENT 6.1:

Molar concentration of SF6 ($kmol/m^3$) x 1000 x molecular weight of exhaust gas (g/mol) x u (m/s) / q (g/s)

5.2 Results and Discussion

Fig. 5.3 shows comparisons of the mean velocity profile between inlet and outlet. The numerical method can accurately simulate the horizontally homogeneous specified mean velocity boundary layer profile under open country conditions by using the second method proposed by Blocken (2004). These mean velocity profiles are very important for accurately predicting the convection term in Equation (2-17). However, Fig. 5.4 shows that the numerical models could not accurately simulate the specified kinetic energy and dissipation rate under open country conditions as previously discussed (Blocken et al., 2005).

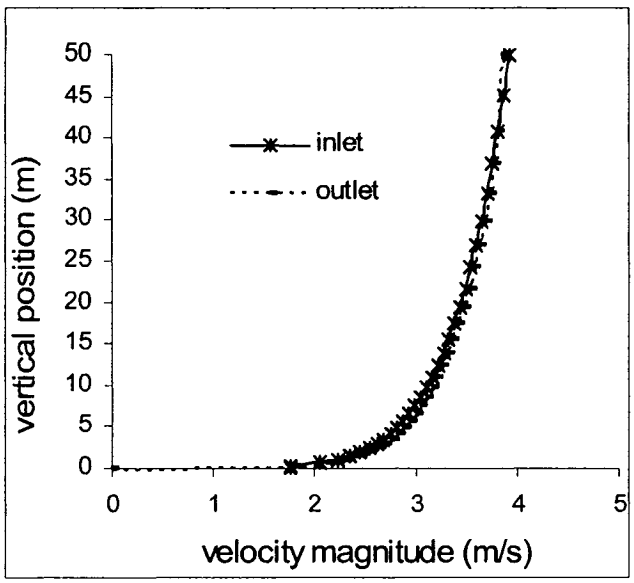

Figure 5.3 Comparison of Velocity Profile between Domain Inlet and Outlet

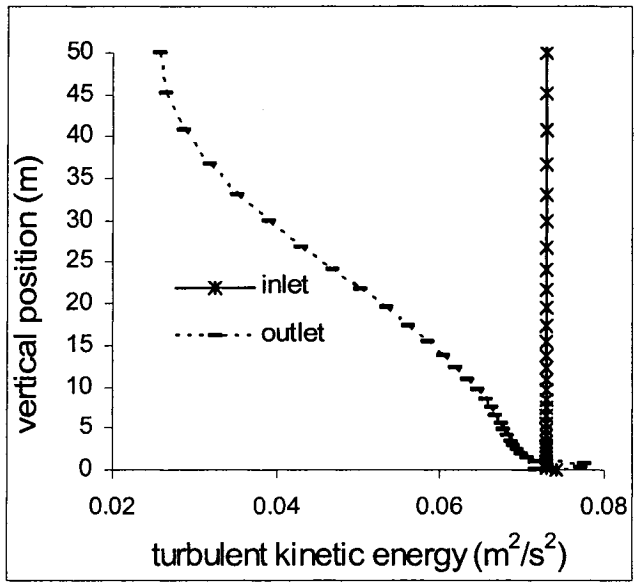

(a)

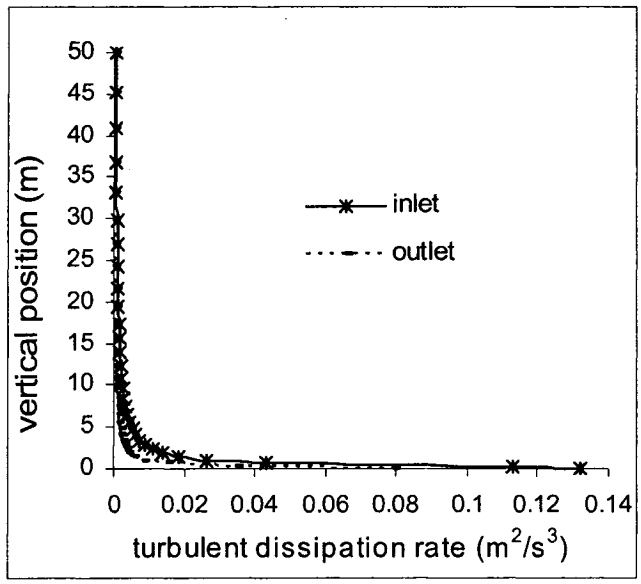

(b)

Figure 5.4 Comparisons of (a) Turbulent Kinetic Energy Profile and (b) Turbulent Dissipation Rate between Velocity Inlet and Outlet

Fig. 5.5 shows ground level concentration directly downwind of the stack for both stack cases and compares the numerical results with the Gaussian model data. Note that the concentration calculations in the Gaussian model start from 100 m away from the stack,

considering it's inaccuracy for points within 100 m from the stack. Numerical results show that these concentration values for the stack height of 2 m are larger than those for the stack height of 16 m within 300 m downwind distance, because the plumes from a 2 m stack take shorter time to reach the ground level than those from a 16 m stack. After 300 m distance, the stack height differences do not affect the concentration at ground level and the concentration decreases logarithmically along downwind distance. The concentration values from the numerical model are very close to those from the Gaussian model for positions away from the stack, including the maximum concentration values and their positions at the ground level.

In the 16 m stack case study, the concentration value obtained with the Gaussian and numerical model do not compare well for distance less than 130 m from the stack. The Gaussian model underestimates concentration values compared with the CFD results. The discrepancies may be due to the assumptions of constant wind speed in vertical direction adopted in the Gaussian model or the application range of Pasquill-Gifford spread factors (Appendix B). Also, Boussinesq hypothesis in the numerical method is based on the mixing length theory. For points close to the emission sources, this theory is not valid if the mesh size is larger than the scale of turbulent eddies. However, increasing the resolution of the model will need more computational resources, but this may not be necessary for several applications.

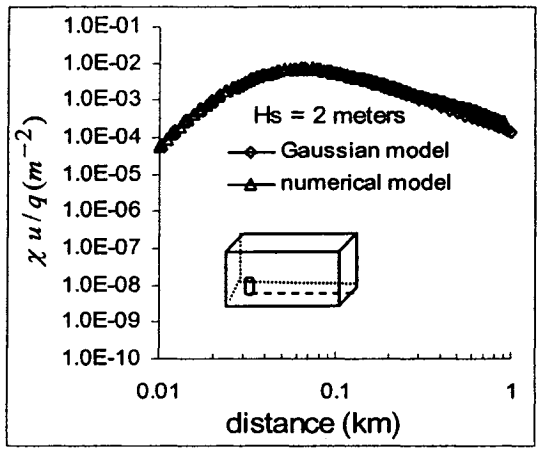

(a)

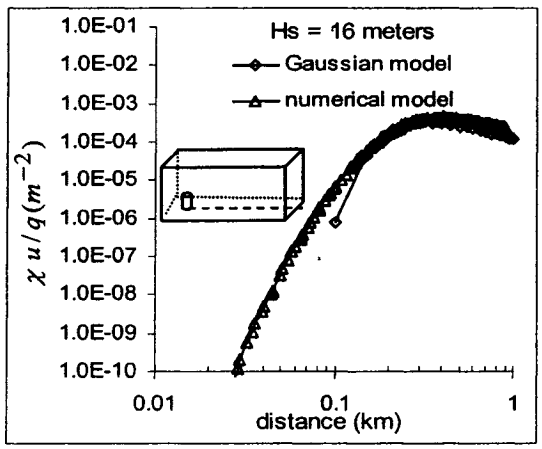

(b)

Figure 5.5 Comparison of Ground Level Concentration on Plume Centerline Directly Downwind of the Stack between the Gaussian Model and FLUENT 6.1 Numerical Models for Stack Height of 2 and 16 m

Lateral and vertical concentration distributions at 200 m downwind from the emission source are shown in Fig. 5.6 and Fig. 5.7 for the 2 m and 16 m stacks. The lateral and vertical concentration distributions show there are not very large differences between the Gaussian model and CFD simulation. For the 2 m stack case, CFD gives the same plume spread except for the vertical direction. This could be due to the stronger shear flow near

the ground level, which breaks assumptions in the Gaussian model, especially for the 2 m stack case. For the 16 m stack case, CFD gives higher maximum concentration in the vertical direction and less plume spread at the stack height level than the Gaussian model does.

The effective plume height is underestimated by the numerical model compared with the plume rise formula used in the Gaussian model for both cases, as shown in Fig. 5.6 (a) and Fig. 5.7 (a). For the 16 m stack case, the effective stack height of 19.6 m calculated by the equation (3-6) is larger than 15.7 m predicted by the numerical model. The possible reason is that k profile could not be kept homogeneous throughout the computational domain.

Fig. 5.6 (b) and (c) show that the plume mass flux through the crosswind plane at the stack height level are the same as those at the ground level for the 2 m stack. The effective stack height is not high enough and the plume dispersion is speeded up by the strong shear flow near to the ground. However, for the 16 m stack, the plume mass fluxes through the crosswind plane at the stack height level are almost one order larger than those at the ground level, as shown in Fig. 5.7 (b) and (c). The effective stack height is high enough so that only small parts of plume reach the ground level.

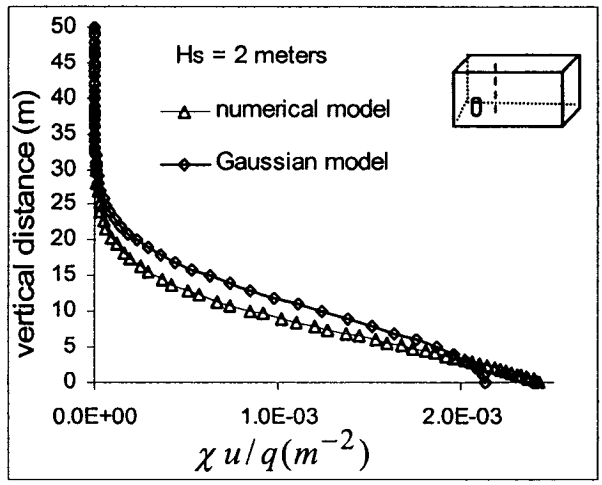

(a)

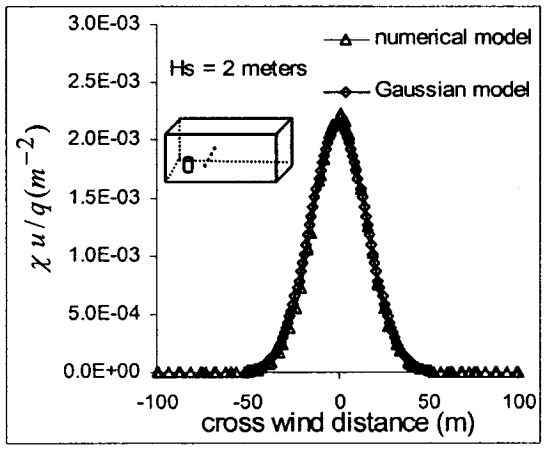

(b)

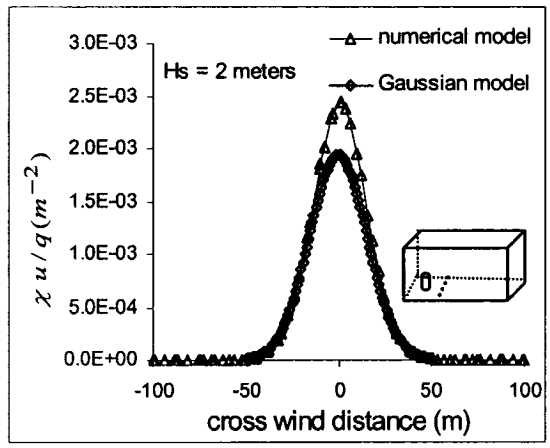

(c)

Figure 5.6 Stack Height of 2 m Case (a) Vertical Concentration Distribution 200 m Downwind at Plume Center (b) Crosswind Concentration Distribution 200 m Downwind at Stack Height Level and (c) at Ground Level (M = 4 and d = 0.2 m)

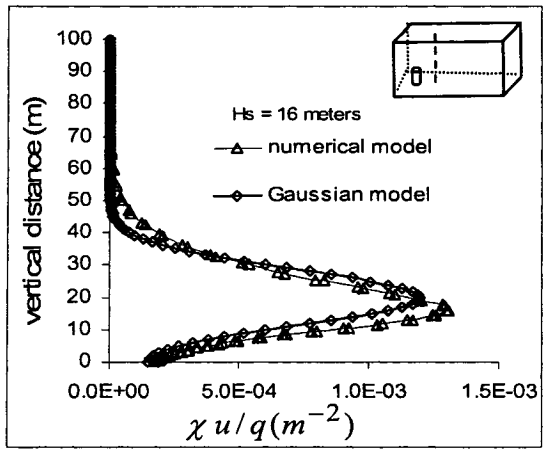

(a)

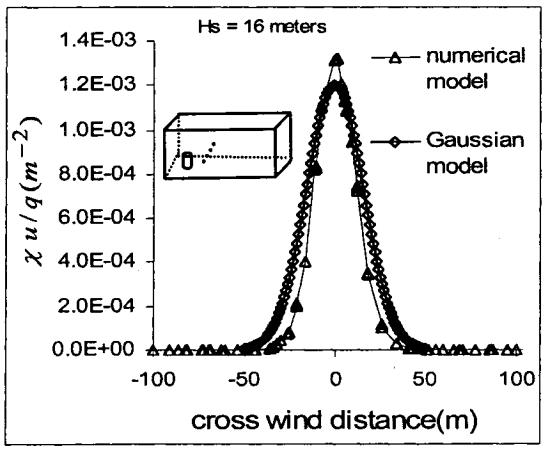

(b)

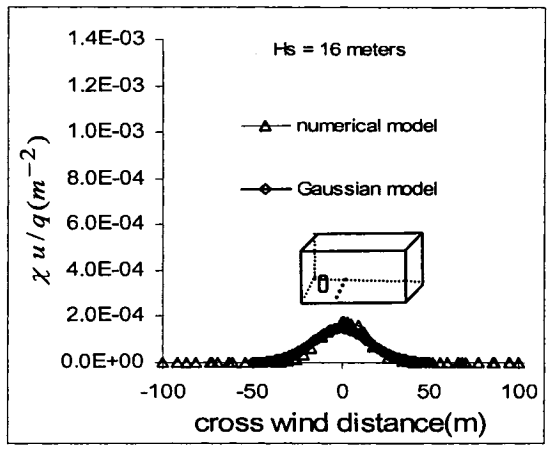

(c)

Figure 5.7 Stack Height of 16 m Case (a) Vertical Concentration Distribution 200 m Downwind at Plume Center (b) Crosswind Concentration Distribution 200 m Downwind at Stack Height Level and (c) at Ground Level ($M = 2$, $d = 0.6$ m)

The influence of various factors on the CFD results was investigated for the case of the isolated stack. These factors include turbulent Schmidt number, mesh size, and the discretization scheme. Table 5-1 shows 8 series that were tested. Based on the stack height, the proper computational domain size was chosen, as mentioned before. Different mesh densities were tried to obtain mesh independent results. Turbulent Schmidt numbers

in the range between 0.3 and 0.9 were examined. Variable numerical discretizations (QUICK and POWER LAW) were tested in this parametric study. Standard $k-\varepsilon$ model with the standard wall function were used for every case study. Computational time and the residual level for concentration are also listed in Table 5-1. The residual level for concentration was obtained after no further convergence could be obtained.

Fig. 5.8 and Fig. 5.9 show the influence of mesh density on the concentration distribution for the stack height of 2 m and 16 m respectively. For both cases, slightly improved concentration predictions were found using fine meshes. However, models with fine meshes need more calculation time than those with coarse meshes (as shown in Table 5-1). It is not necessary for several applications.

Test series	Computational domain size (m)	Node number	Stack height (m)	Stack diameter (m)	Turbulent Schmidt number	Moment Ratio (M)	Discretization scheme	Residual level for concentration	Running time (hours)
1	1000x300x200	738,327	16	0.6	0.3	2	Second order for pressure and QUICK for others	10^{-5}	24
2	1000x200x50	591,690	2	0.2	0.5	4	Standard for pressure and Power law for others	10^{-3}	12
3	1000x200x50	591,690	2	0.2	0.5	4	Second order for pressure and QUICK for others	Diverge	4
4	1000x300x200	444,000	16	0.6	0.3	2	Second order for pressure and QUICK for others	10^{-3}	5
5	1000x200x50	467,400	2	0.2	0.5	4	Standard for pressure and Power Law for others	10^{-3}	4
6	1000x200x50	591,690	2	0.2	0.9	4	Standard for pressure and Power Law for others	10^{-3}	12
7	1000x300x200	738,327	16	0.6	0.9	2	Second order for pressure and QUICK for others	10^{-5}	24
8	1000x300x200	738,327	16	0.6	0.3	2	Second order for pressure and Power Law for others	10^{-5}	24

Table 5-1 Parametric Study of Plume Dispersion from One Isolated Stack in Open Country Terrain: Standard $k-\varepsilon$ Model and Standard Wall Function for All Cases

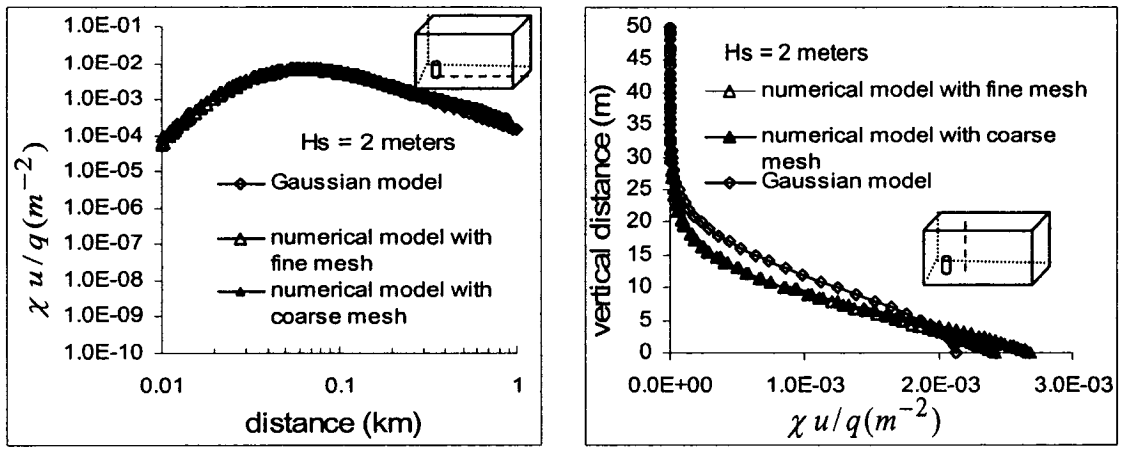

Figure 5.8 Influence of Mesh Density on Concentration Distribution for H_s = 2 m (a) Ground Level at Plume Center (b) Vertical Distribution 200 m Downwind at Plume Center (c) Crosswind Distribution 200 m Downwind at Stack Height Level and (d) at Ground Level

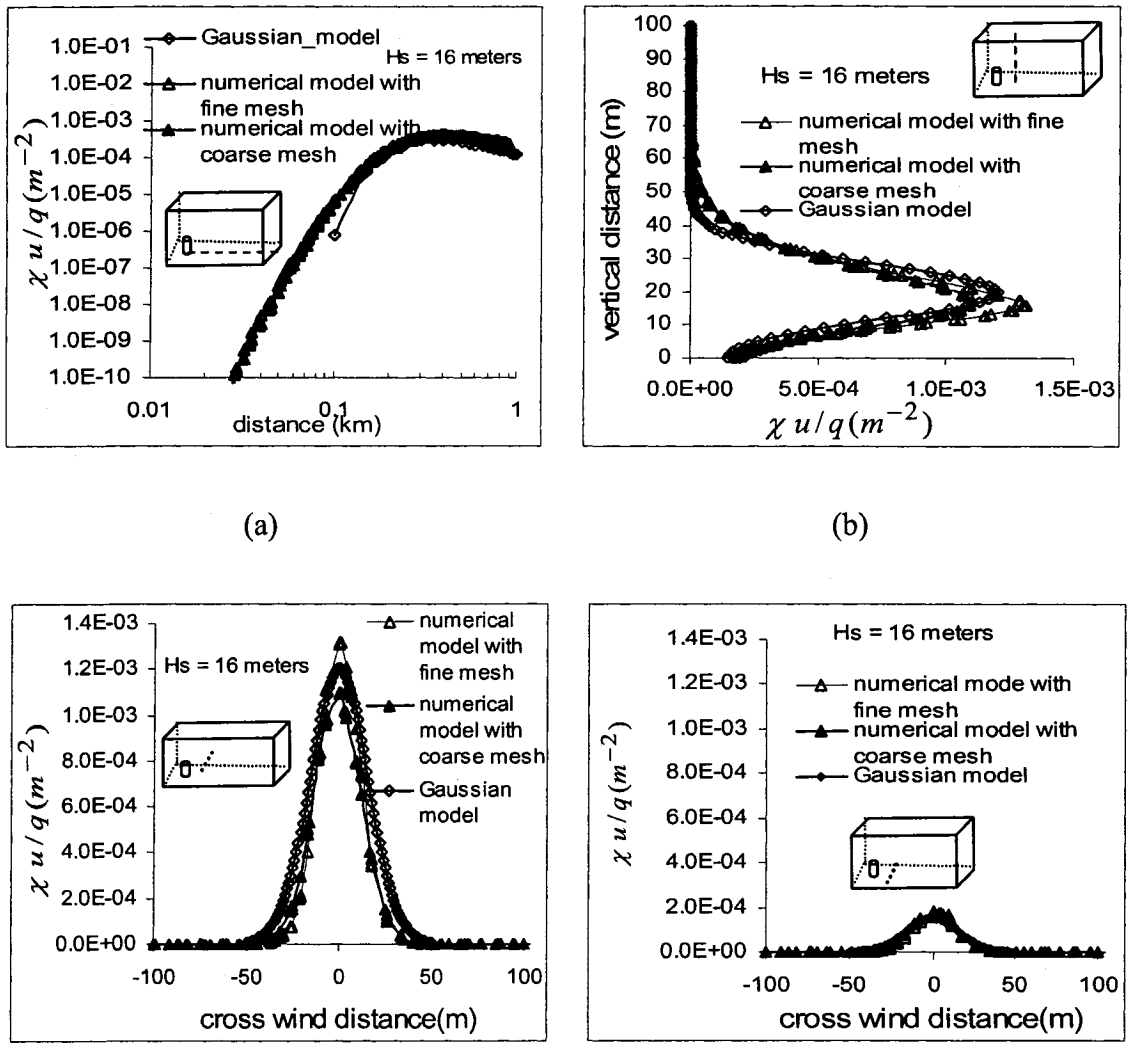

Figure 5.9 Influence of Mesh Density on Concentration Distribution for H_s = 16 m (a) Ground Level at Plume Center (b) Vertical Distribution 200 m Downwind at Plume Center (c) Crosswind Distribution 200 m Downwind at Stack Height Level and (d) at Ground Level

Fig. 5.10 shows the effects of turbulent Schmidt number on the plume trajectories for the 2 m and 16 m stacks. Decreasing this number increases turbulent diffusivity. In this case study, this number was artificially changed to improve the agreement between numerical

results and Gaussian model. Compared numerical results with the Gaussian model, the turbulent Schmidt numbers 0.3 and 0.5 give better agreements for plume dispersion from a stack height of 16 m and 2 m respectively.

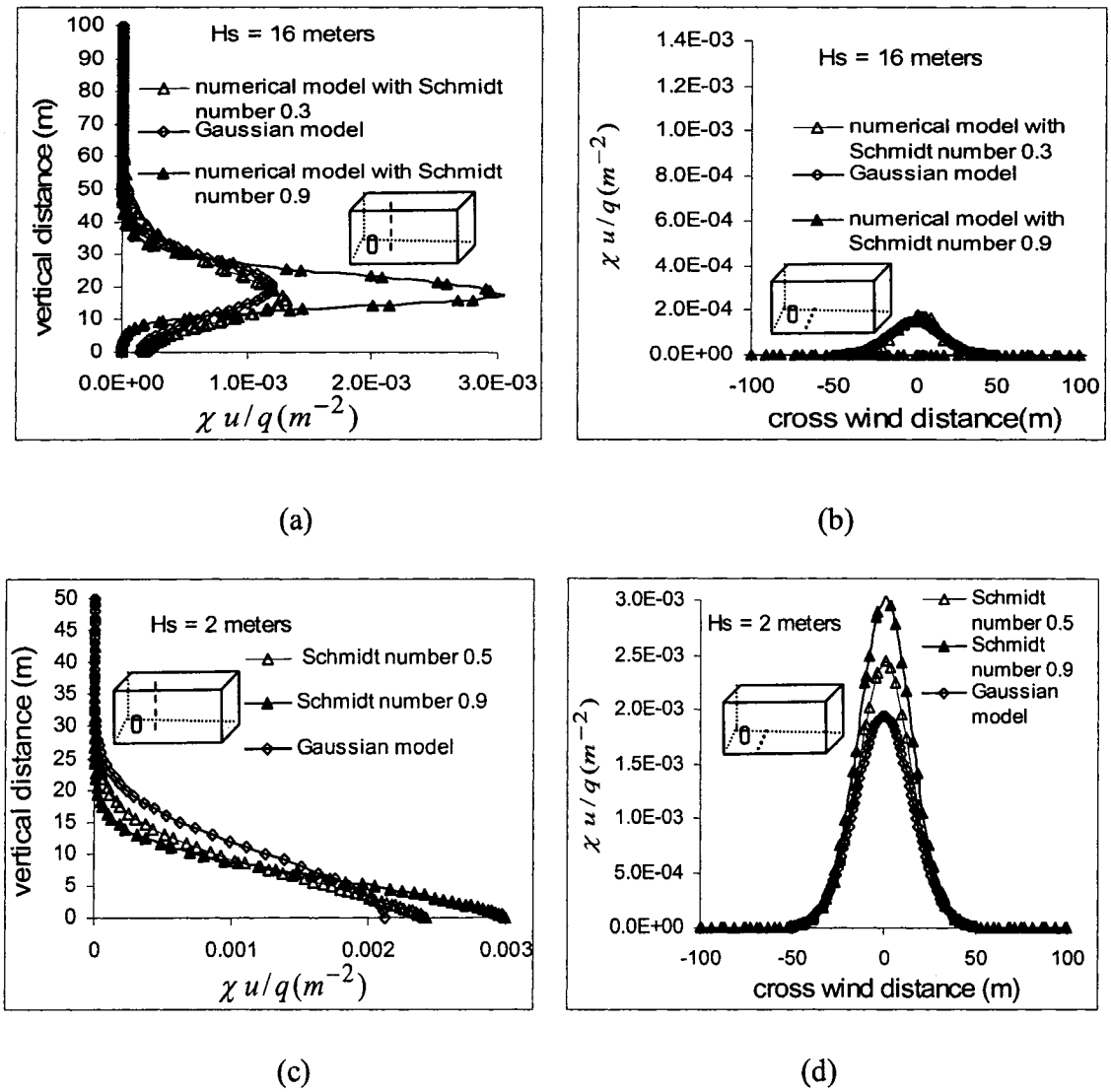

Figure 5.10 Influences of Turbulent Schmidt Number on Concentration Distribution (a) Vertical Distribution 200 m Downwind at Plume Center for stack height 16 m (b) Crosswind Distribution 200 m Downwind at Ground Level for stack height 16 m (c) Vertical Distribution 200 m Downwind at Plume Center for stack height 2 m (b) Crosswind Distribution 200 m Downwind at Ground Level for stack height 2 m

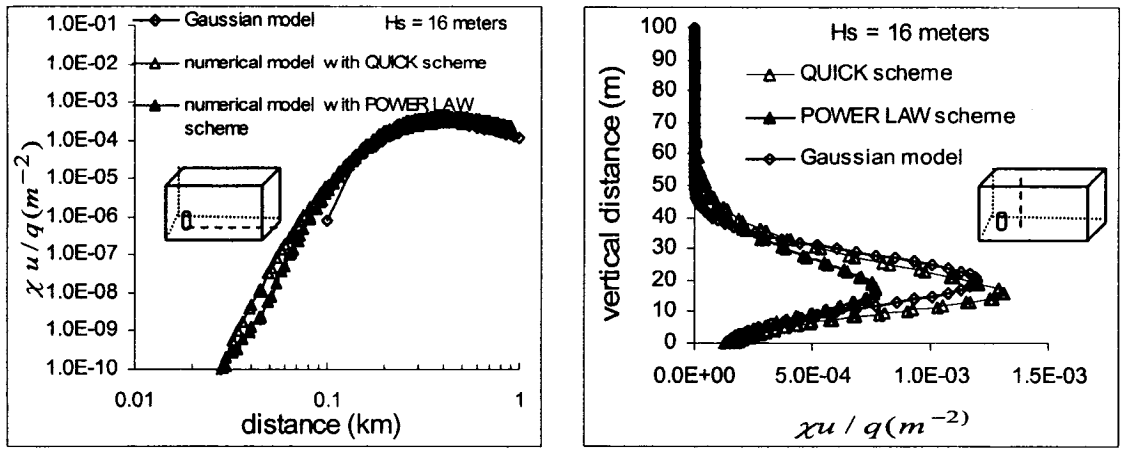

(a) (b)

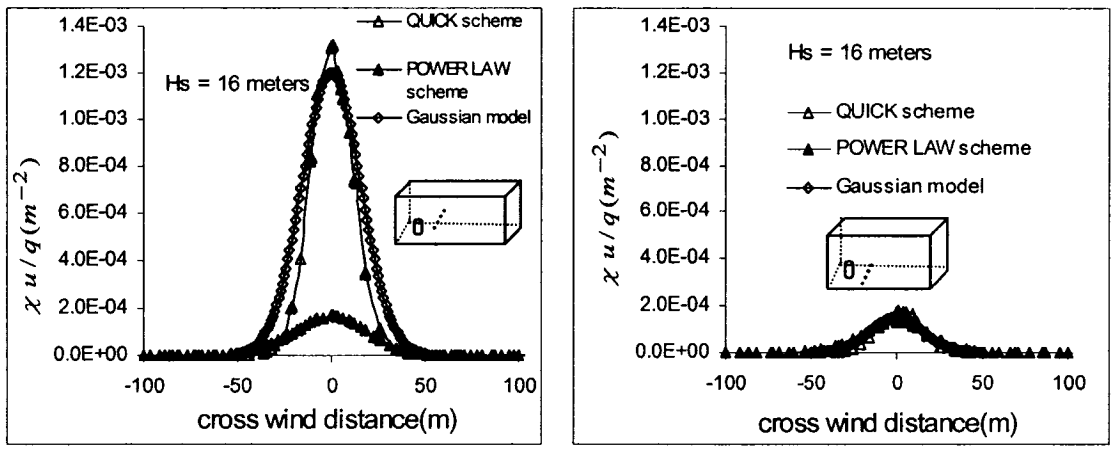

(c) (d)

Figure 5.11 Influences of QUICK and POWER LAW Discretization Scheme on Concentration Distribution for the 16 m stack (a) Ground Level at Plume Center (b) Vertical Distribution 200 m Downwind at Plume Center (c) Crosswind Distribution 200 m Downwind at Stack Height Level (d) at Ground Level

Fig. 5.11 shows the influence of discretization schemes on the concentration distribution for the stack height of 16 m. The second order discretization scheme QUICK and the first order discretization scheme POWER LAW were examined in this case. QUICK scheme

is based on a weighted average of second-order-upwind and central interpolations of the variable. POWER LAW interpolates the variable using the exact solution to a one-dimensional convection-diffusion equation. Fundamentally high order schemes, such as QUICK, can decrease the discretizaiton errors more than lower order schemes, such as POWER LAW. Here, the discretization schemes significantly affect concentration distributions for all sampling points except for those at ground level.

In summary, the standard $k-\varepsilon$ model with the standard wall function can simulate the dispersion of emissions from one isolated stack generally well in the present case study. The numerical model underestimated the plume rise compared with that from the Gaussian model. The possible reason is the inhomogeneous turbulent kinetic energy predicted by the numerical model. The parametric study shows the turbulent Schmidt number has a great effect on the plume dispersion, as well as the discretization scheme. In this study, turbulent Schmidt number was artificially changed to fit the data from the Gaussian model.

CHAPTER 6 DISPERSION AROUND AN ISOLATED CUBIC BUILDING

6.1 Introduction

In this chapter, the flow field and dispersion around a cubic building are examined using the realizable $k-\varepsilon$ model and Reynolds stress model in FLUENT 6.1. The exhaust source is a flush stack located at the rooftop center. Numerical results were obtained from several turbulence models considered. Numerical results were compared with wind tunnel data.

6.2 Wind Tunnel Tests

Dobrescu (1994) measured the dispersion of passive effluent plumes emitted from a flush stack mounted on a wind tunnel model. In his study, the size of the cube was 6 cm. The wind profile $U(z)=4.73(z)^{0.14}$ had the power law formation with $\alpha = 0.14$ and 4.2 m/s free stream wind speed. The wind direction is perpendicular to the cube face. SF6 and nitrogen was injected from the center of the roof with upward velocity 0.24 m/s and momentum ratio 0.7. The diameter of the stack was 6 mm. The mean concentrations of SF_6 were measured at different tappings using a Varian gas chromatograph.

In Dobrescu's (1994) study, the dimensionless concentration K was used to evaluate the concentration on the plume centerline and was defined as:

$$K = \frac{CL^2 U_{H_b}}{A_e V_e C_e} \tag{6-1}$$

where L is the length or width of the building and U_{H_b} is the velocity at the roof height. Some characteristic parameters, such as the low momentum ratio, turbulent intensity of atmospheric boundary layer at the roof level, stack height, and the stack diameter, used in his wind tunnel test are very close to those used in Li & Meroney (1983). Therefore, the following numerical simulation will be validated with the wind tunnel tests from both Dobrescu (1994) and Li & Meroney (1983).

6.3 Numerical Simulation

6.3.1 Pre-processor

1) Defining the geometry of the region of interest: computational domain (Fig. 6.1)

The distance upwind of the building is 0.30 m (5 H_b); the length of the downwind fetch is 0.90 m (15 H_b). The lateral distance between the side walls of the building and the computational domain is 0.36 m (6 H_b)

2) Grid generation: Due to the circular exhaust outlet, a Hex /Wedge Cooper mesh type was used on the roof of the building. Around the building, the Hex Map mesh type was used. Considering the larger gradient of velocity near the wall, denser meshes were used near the ground and the building surfaces. Because the wall function was used for the near wall treatment, y^* varied from 11.25 to 100. The mesh resolution in x, y, z direction is listed in Appendix D. The total mesh size is 327,384.

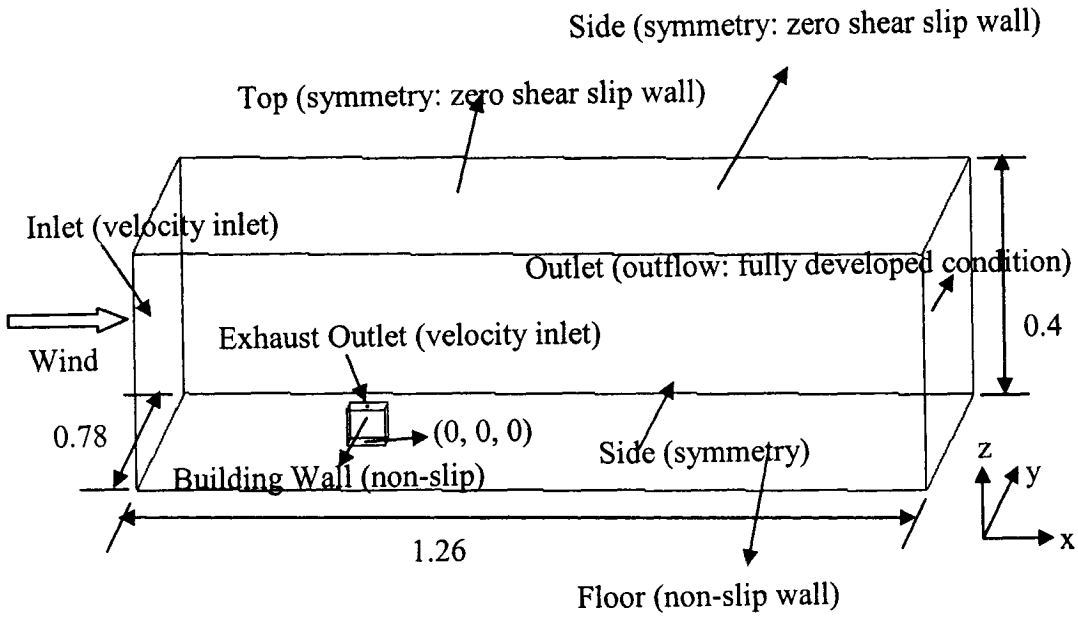

Unit: m

Figure 6.1 Sizes and Layout of the Computational Domain and Boundary Conditions (Note: names outside parentheses are for components of the computational domain and inside are for numerical boundary conditions)

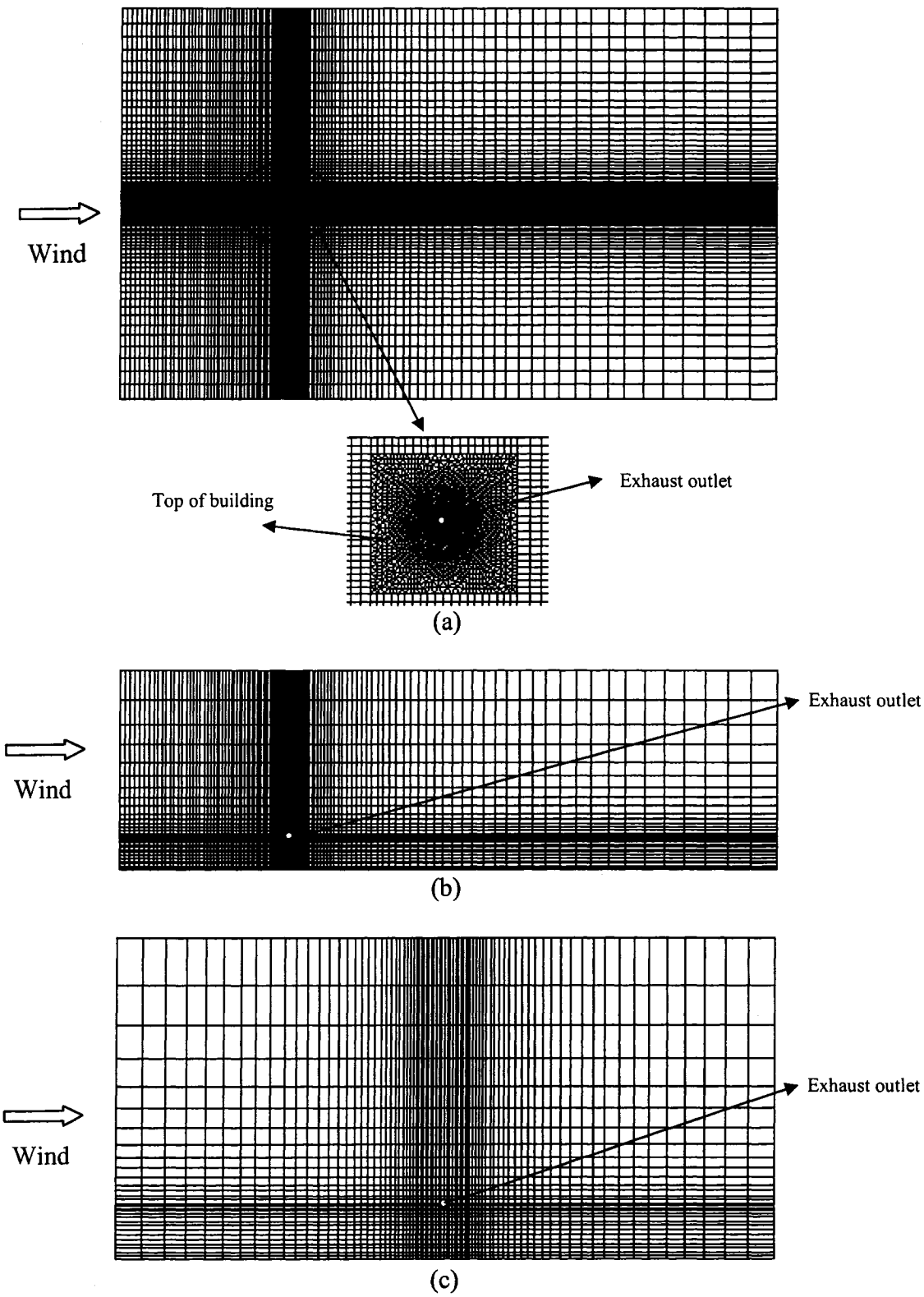

Figure 6.2 Grid Generation for Domain 1.26 x 0.78 x 0.4 (m) (a) Top View (x-y plane) (b) Side View (x-z plane) (c) Front View (y-z plane)

3) Specification of boundary conditions (Fig. 6.1)

a) An open country velocity profile $U(z)=4.73\ (z)^{0.14}$ was specified at the inlet. The wind direction is along +x direction. Profiles of turbulent kinetic energy $k=\frac{3}{2}(U(z)\times I(z))^2$ (where $I(z)$ was referred to wind tunnel data from Dobrescu (1994) and shown in Fig. 6.3 (d)) and dissipation rate $\varepsilon=\frac{U^{*3}}{\kappa\times z}$ (where $U^*=\frac{\kappa\times U(\delta)}{ln(\delta/z_0)}=0.22$, δ = 0.4 m, and z_0 = 0.013 cm), were also specified at the inlet as a User Defined Function (UDF) in FLUENT 6.1. These profiles are shown in Fig. 6.3. The detailed program is listed in Appendix F;

b) SF_6 with nitrogen was released from the exhaust outlet along the +z direction with the momentum ratio of 0.07;

c) Symmetry is set at the sides and top of the calculated domain;

d) The no-slip condition is applied to each surface (floor, building walls and the roof);

e) The physical roughness height of the floor is set to 0.0019 m and the roughness constant is set to 0.5. The roughness height of the building sides and rooftop are set to 0 m and roughness constants of these are set to 0.5;

f) Outflow boundary condition was set at the exit of the computational domain.

All of the above pre-processing work was done by the commercial software GAMBIT 2.0.

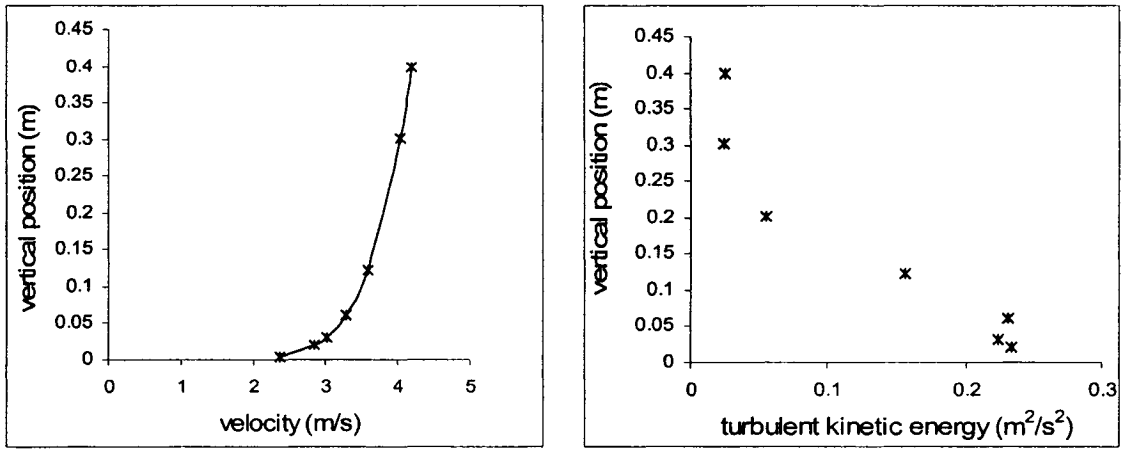

(a) (b)

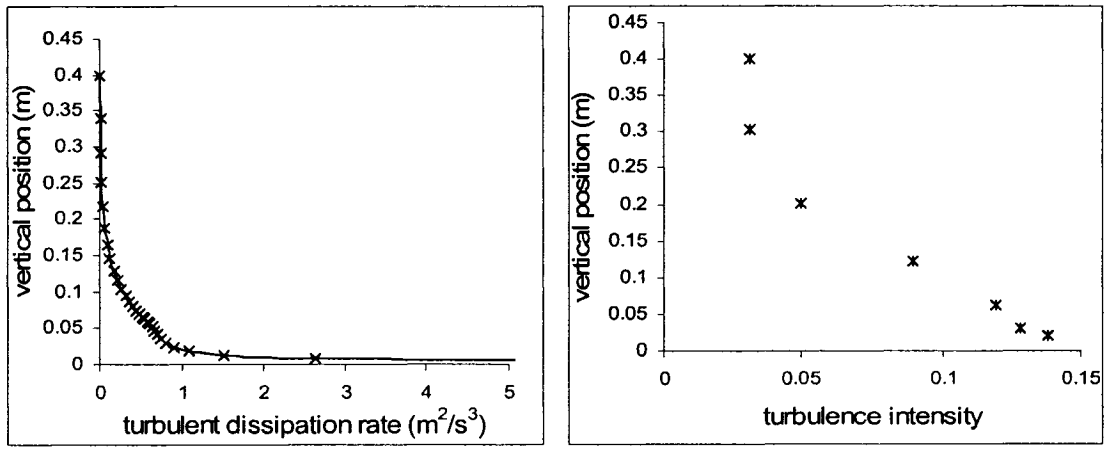

(c) (d)

Figure 6.3 Variation of Boundary Layer Parameters with Height at the Inlet (a) Wind Velocity Profile (b) Turbulent Kinetic Energy Profile (c) Turbulent Dissipation Rate Profile (d) Turbulence Intensity

6.3.2 Solver

A segregated solver is used in this case study. Its definition can be referred to the section 2.6.2. Some important parameters are mentioned here

1. Because the standard $k-\varepsilon$ model can not predict accurately recirculation zones around the building, the realizable $k-\varepsilon$ model and the Reynolds stress model are used here;
2. The effects of turbulent Schmidt number (Sc_t = 0.3, Sc_t = 0.7) on the concentration distribution is examined;
3. The standard wall function is used for near wall treatment and y^* varies from 11.25 to 100;
4. QUICK is used for discretizing momentum and exhaust concentration equations;
5. The SIMPLE method is used for coupling pressure and velocity in the realizable $k-\varepsilon$ model and the SIMPLEC method is used for coupling pressure and velocity in the Reynolds stress model to accelerate the convergence;
6. For the fluid field, the "scaled" residual of 1×10^{-5} was obtained. For the pollutant concentration, the "scaled" residual of 1×10^{-6} was obtained. These residuals were obtained after no further convergence could be obtained.

6.3.3 Post-processor

Accurate simulation of the wind field around the building is necessary to calculate the correct plume behavior. Velocity distributions around the building from Wilson (1979), Hosker (1980) and Castro & Robins (1977) and pressure coefficients from Dumitrescu-Brulotte (1987) and Stathopoulos (1981) were used as references to the present numerical model. Wind tunnel data from Dobrescu (1994) and Li & Meroney (1983) were used for validating the concentration distribution obtained with the numerical model.

6.4 Results and Discussion

The turbulent atmospheric boundary layer was first examined to see if it is horizontally homogenous or not for an empty computational domain, i.e. without building effects.

Predicted profiles of mean velocity, kinetic energy and dissipation rate obtained with the Reynolds stress model (RSM) are shown in Fig. 6.4. It is found that the numerical model predicted the profile of the mean velocity and dissipation rate accurately using the Reynolds stress model. The k-ε models could not accomplish this, as already discussed in Chapter 5. However, RSM still could not predict the profile of the kinetic energy accurately at the outlet due to the inconsistent parameters used to describe the log-law profile near the wall, as mentioned in Chapter 5.

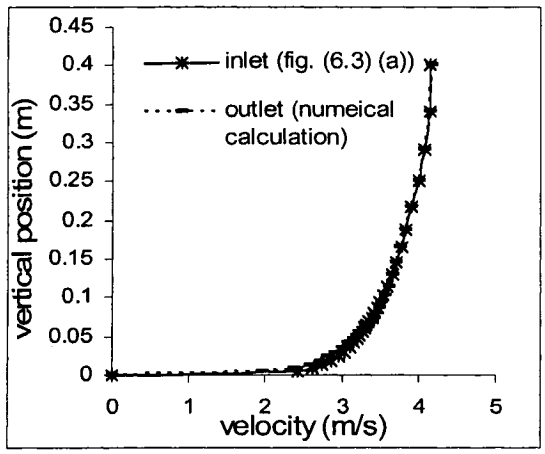

(a)

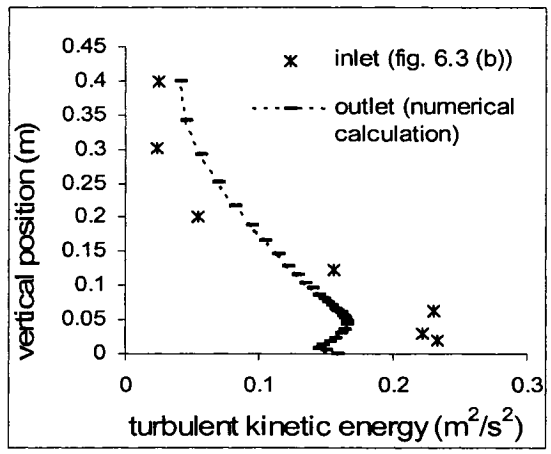

(b)

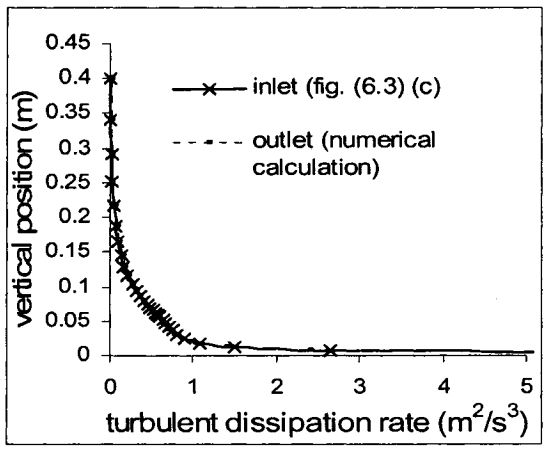

(c)

Figure 6.4 Numerical Evaluations of (a) Velocity Magnitude Profile (b) Turbulent Kinetic Energy Profile and (c) Turbulent Dissipation Rate Profile between Velocity Inlet and Outlet

Profiles of mean surface pressure coefficients for the centerlines on the front face (A), top (B), leeward wall (C) and side wall (D) of a cube are shown in Fig.6.5. Along with the numerical results, experimental results from Dumitrescu-Brulotte (1987) and Stathopoulos (1981) are shown for comparisons. The RSM1 model (RSM with wall reflection effect) predicts a maximum positive pressure coefficient of 0.77 at 0.63 H_b,

which is the stagnation point on the upwind wall. This compares well with results of Dumitrescu-Brulotte (1987). On the roof surface, the RSM1 model predicts Cp of - 0.6 at the windward edge and reduces to - 0.85 at x = - 0.3 H_b before recovering to - 0.25 at the leeward edge. The negative pressure coefficient does not change much on the leeward wall and the side wall. It is seen that numerical simulation using RSM1 model predicts the pressure coefficient well on the upwind wall and leeward wall. It agrees well with results of Stathopoulos (1981) on the roof surface. However, it underestimates the maximum suction compared to Dumitrescu-Brulotte (1987). A large difference exists on the side wall. Numerical results are about 0.7 times of those from the experimental test (Dumitrescu-Brulotte, 1987).

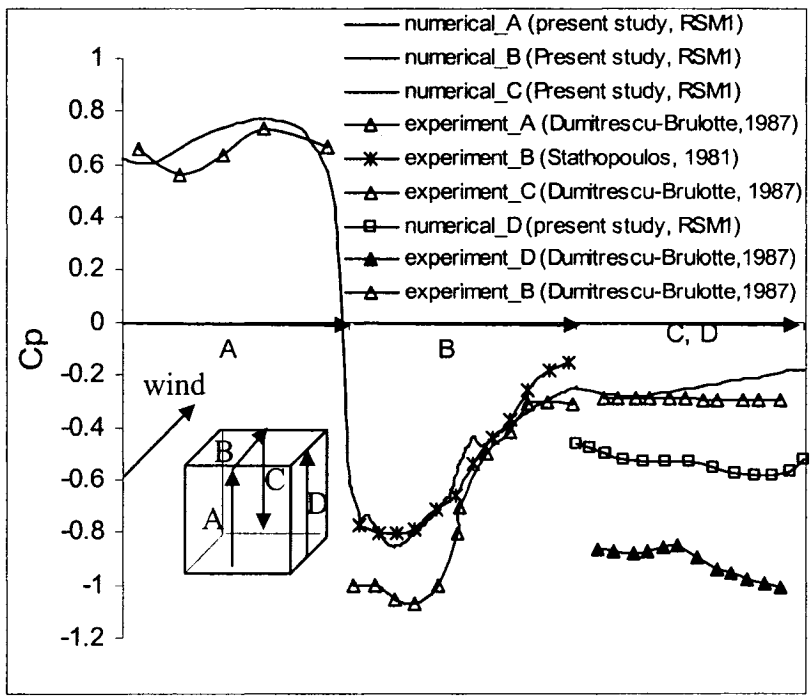

Figure 6.5 Surface Pressure Coefficients on the Cube

The variation of the mean longitudinal velocity with height on the centre line (y = 0) for $0 \leqslant x / H_b \leqslant 10$ (x is the distance from the cube center) is shown in Fig. 6.6. The data

have been normalized with the wind speed at gradient height, U_r. It is found that a large recirculation zone extends over almost the entire roof (90%, at $x/H_b = 0.4$ in Fig. 6.6), which agrees with the recirculation length 0.9 H_b predicted by Wilson (1979). At the roof center $x/H_b = 0$, the height of the recirculation zone is 1.12 H_b, which is less than 1.22 H_b predicted by Wilson (1979). The wake cavity extends to the length of 2.3 H_b away from the back of the building (at $x/H_b = 2.8$), which is larger than 1.0 H_b predicted by Wilson (1979) and larger than 1.5 H_b predicted by Hosker (1980). After $x/H_b = 10$, the mean velocity profile was close to that in the approaching flow.

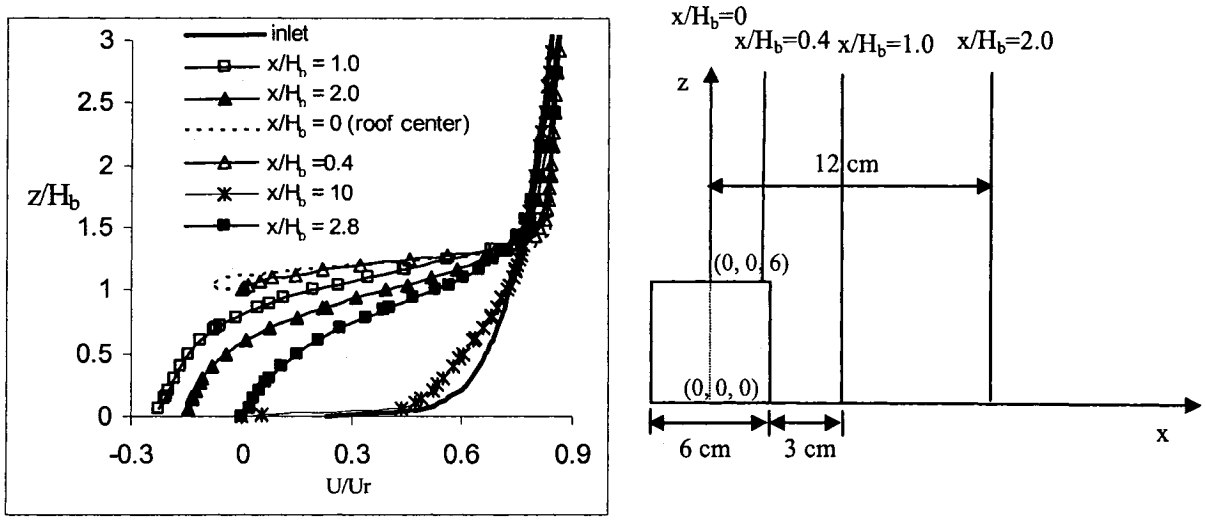

Figure 6.6 Variations of the Mean Longitudinal Velocity with Height on the Center Line (y = 0)

Fig. 6.7 shows the lateral variation of U at the half height of the building. Both present numerical simulation with RSM1 model and experimental data from Castro & Robins (1977) show the similar lateral circulation zones deflected to 1.5 H_b away from the building sides. The differences between numerical and experimental data are caused by

the different mean approaching velocity profiles used in the present study and Castro & Robins (1977), as shown in Fig. 4.2.

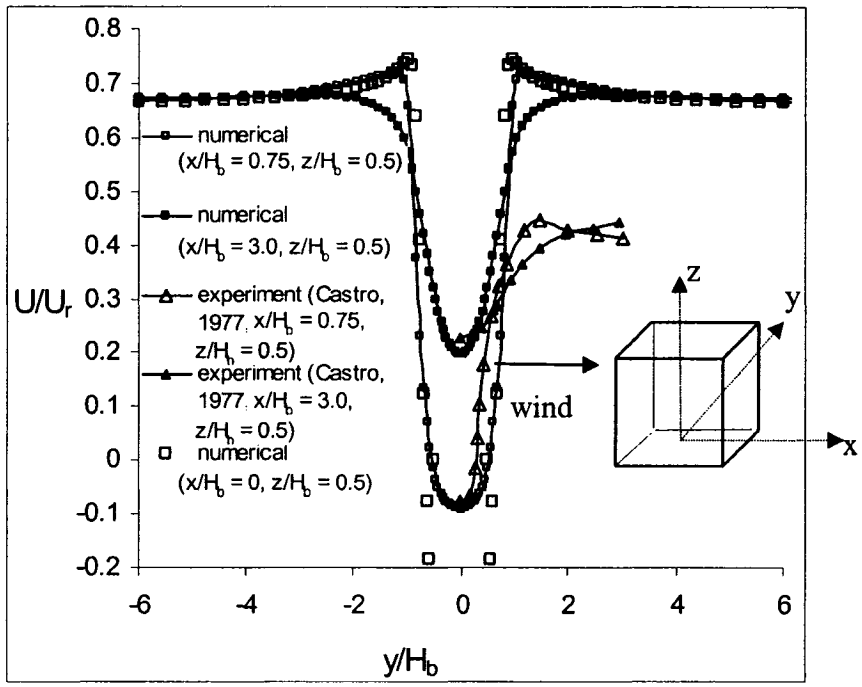

Figure 6.7 Variations of Mean Longitudinal Velocity in Lateral Direction on the Center Line at Half the Height of the Building

Fig. 6.8 shows contours of the dimensionless concentration, K, on the surface of the building obtained in the wind tunnel tests of Dobrescu (1994) and Li & Meroney (1983). A significant characteristic of the plume dispersion around an isolated cubic building is that the maximum concentration on the roof occurs upwind of the stack. Due to the low exhaust momentum and low stack height, the plume is trapped in the recirculation zone above the roof.

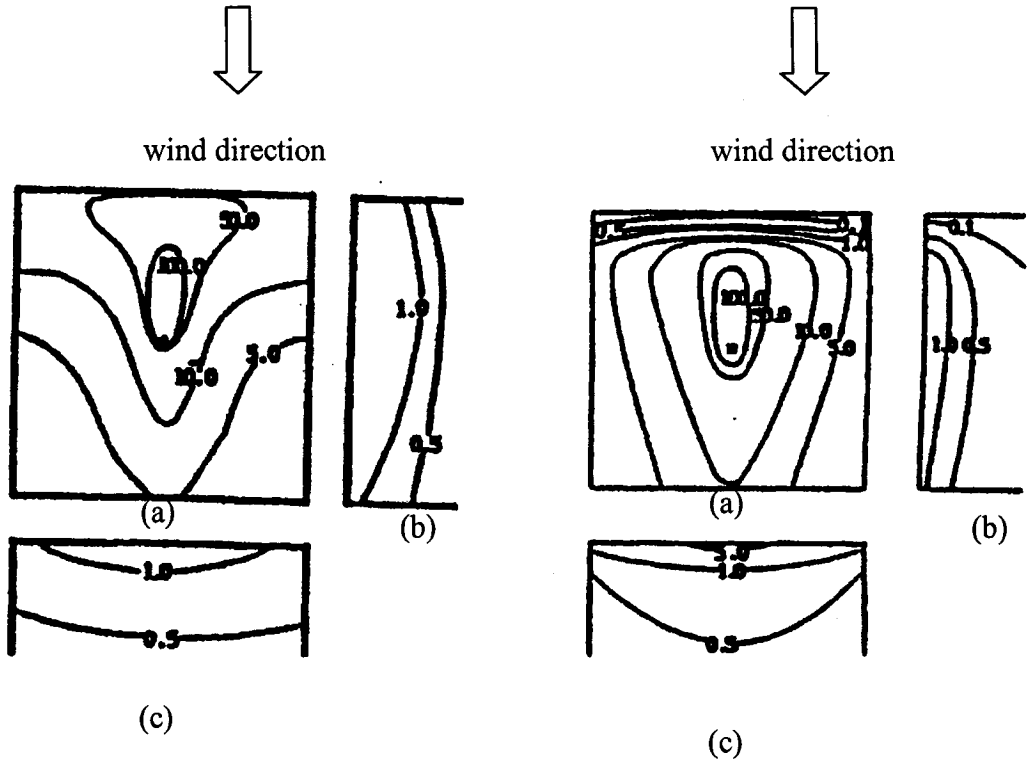

Figure 6.8 Contours of Dimensionless Concentration K on the (a) Top (b) Side (c) Back of the Cubic Building from Wind Tunnel Test

Results from Dobrescu (1994) indicate greater dispersion near the leading edge than those from Li & Meroney (1983) except for the contour of K = 100. Referring to Dobrescu's error analysis, the sampling positions may have contributed to this difference. In Dobrescu's study, he used the tapping system (0 mm up from the roof surface). However, in Meroney's study, he used the movable vertical probes 0.03 mm up from the roof surface.

Distributions of K on the building walls and roof were estimated numerically using three different methods: RSM1 (RSM with wall reflection effects), RSM2 (RSM with quadratic pressure strain model) and the realizable $k-\varepsilon$ model (Fluent, 2003). Fig. 6.9 shows contours of K around the building using the RSM1 model. It gives results which

are consistent with wind tunnel test data. For example, Maximum concentrations on the roof occur upwind of the source.

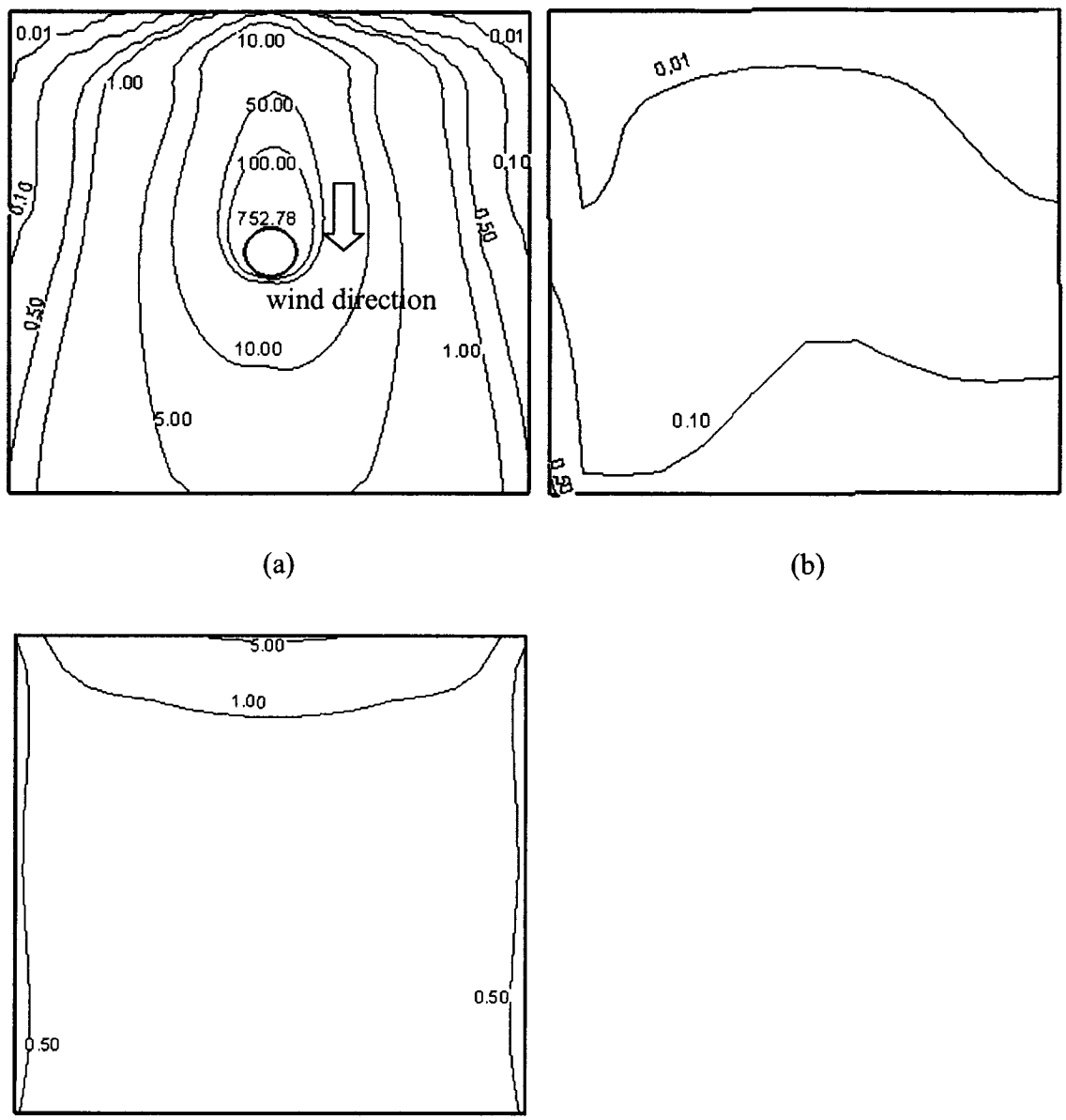

Figure 6.9 K Distributions Obtained with RSM1 Numerical Simulation on the (a) Roof (b) Side Wall (c) Back Wall (turbulent Schmidt number 0.3)

Fig. 6.10 shows K distributions on the building surfaces obtained with the RSM2 model with quadratic pressure-strain. Compared with RSM1 model, the RSM2 model produces a wider plume.

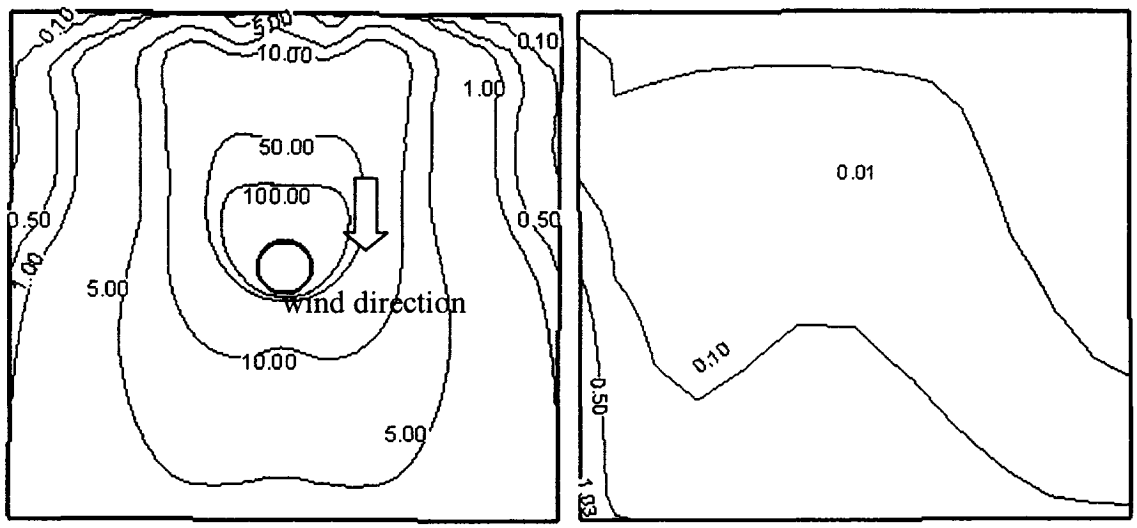

(a) (b)

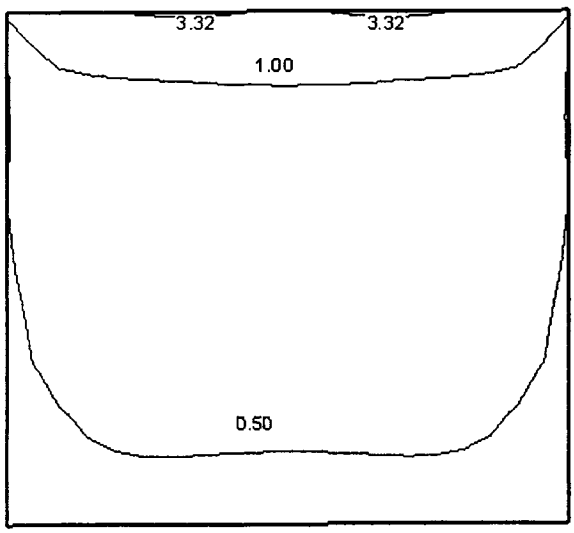

(c)

Figure 6.10 K Distributions Obtained with RSM2 Numerical Simulation on the (a) Roof (b) Side Wall (c) Back Wall (turbulent Schmidt number 0.3)

The contour of $K = 100$ obtained from RSM2 model extends upwind to 1/6 of the length of the building, while the same contour obtained from RSM1 and wind tunnel data extend upwind to 1/4 of the length of the building. With respect to the magnitude and location of K on each surface, RSM1 agrees better with the experimental data than RSM2 does, as shown in Fig. 6.11.

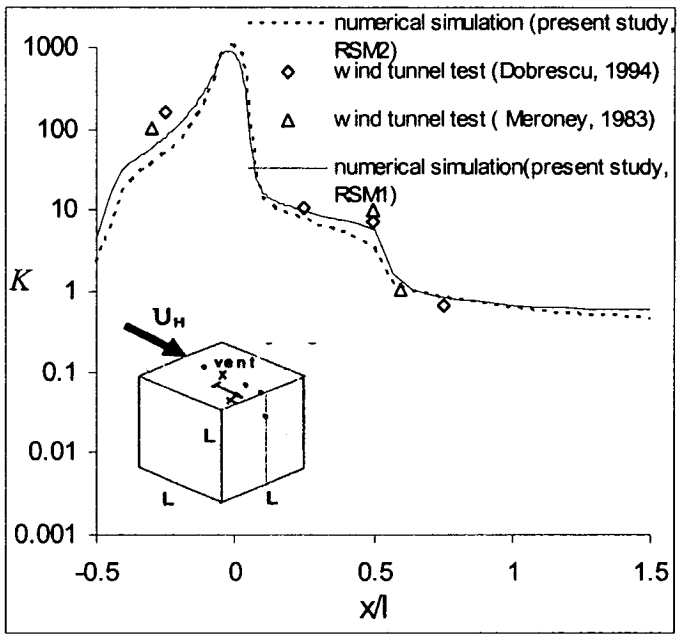

Figure 6.11 K Distributions on Centerline of the Roof and Leeward Wall versus String Distance from Vent Obtained with the RSM1 and RSM2 Model

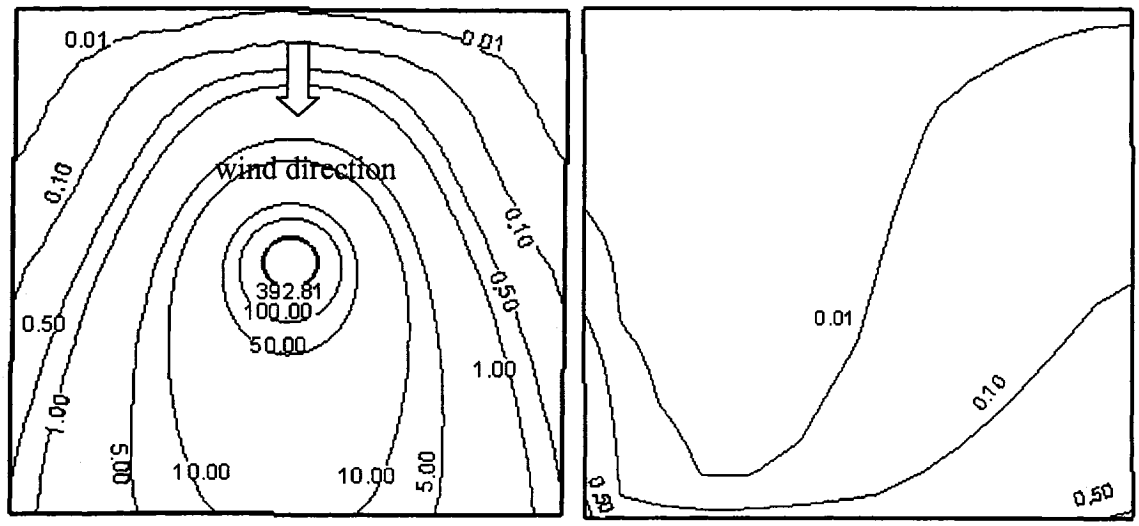

(a) (b)

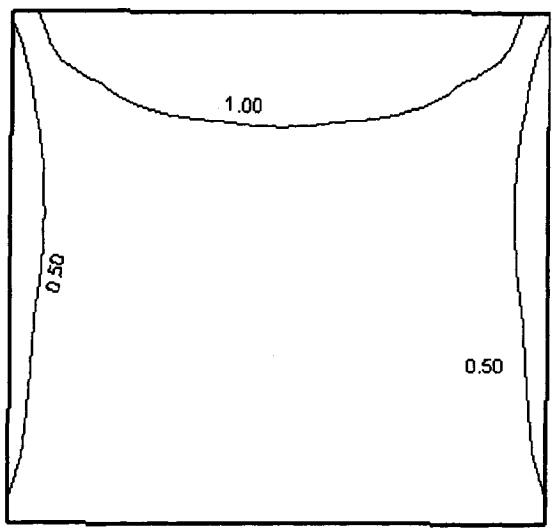

(c)

Figure 6.12 K Distributions Obtained with Realizable $k-\varepsilon$ Numerical Simulation on the (a) Roof (b) Side Wall (c) Back Wall (turbulent Schmidt number 0.3)

Fig. 6.12 shows the contours of K on the building surface obtained with the realizable $k-\varepsilon$ model. Contrary to the distributions in Fig. 6.9 and Fig. 6.10, the major portion of the plume deposits downwind of the stack rather than upwind of the stack. Comparing

Fig. 6.9, Fig. 6.10 and Fig. 6.12 with Fig. 6.8, it is found that dispersion results from both Reynolds stress models are closer to the wind tunnel data than those from the realizable $k-\varepsilon$ model. One possible reason is that Reynolds stress model can predict the turbulent fluxes (including Reynolds stress and pollutant transported mass flux) more accurately than the realizable $k-\varepsilon$ model. The other possible reason for this is that less turbulent kinetic energy is predicted on the rooftop of the building by the realizable $k-\varepsilon$ model than the Reynolds stress models, as shown in Fig. 6.13. The effect of turbulence models on the magnitude and location of K on centerline of the roof and back wall is in Fig. 6.14. The realizable $k-\varepsilon$ model underestimates the concentration upwind of the stack, while it overestimates the concentration downwind of the stack. However, on the back wall, similar distributions of K were predicted by the three turbulence models.

For plume distributions on the sides of the building, the Reynolds stress model predicts more dispersive results than the realizable $k-\varepsilon$ model does, as shown in Fig. 6.15. It can be seen that concentration distributions on the sides obtained from the Reynolds stress model are much closer to the experimental data than those obtained from the realizable $k-\varepsilon$ model. Thus, the following discussion will consider only the results of the Reynolds stress model with wall reflection effects (RSM1).

The RSM1 model accurately predicted the maximum concentration values on the rooftop and leeward wall of the building. It was also found that the plume concentration on the rooftop of the building was much larger than that on the leeward wall because high concentration is quickly diluted by the vortex in the wake of the building. The numerical model underestimated the plume concentration on the sides of the building, as shown in Fig. 6.15. The differences between numerical results and wind tunnel test data increase

when sampling points are further away from the emission source. Very low K was predicted by numerical models near the roof edge. This may be due to the isotropic characteristic of $D_t = \mu_t / (\rho Sc_t)$ in the pollutant transport equation (2-17).

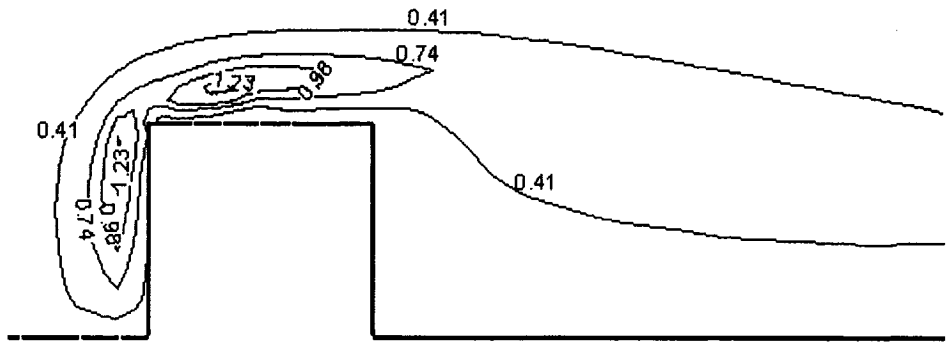

(a)

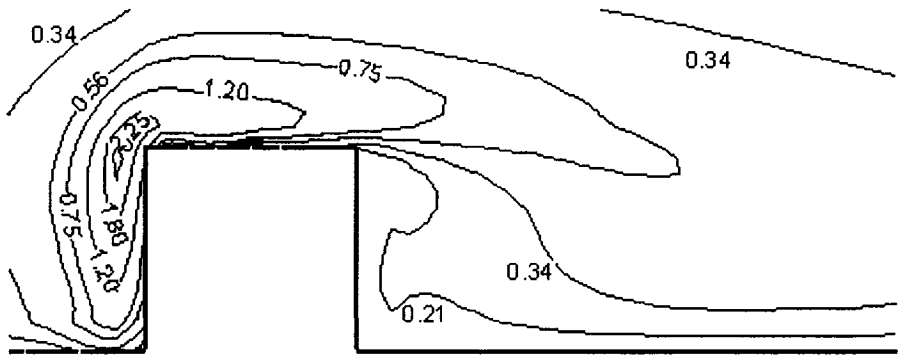

(b)

Figure 6.13 Contours of Turbulent Kinetic Energy k Predicted from (a) Reynolds Stress Model with Wall Reflection Effects (b) Realizable $k-\varepsilon$ Model

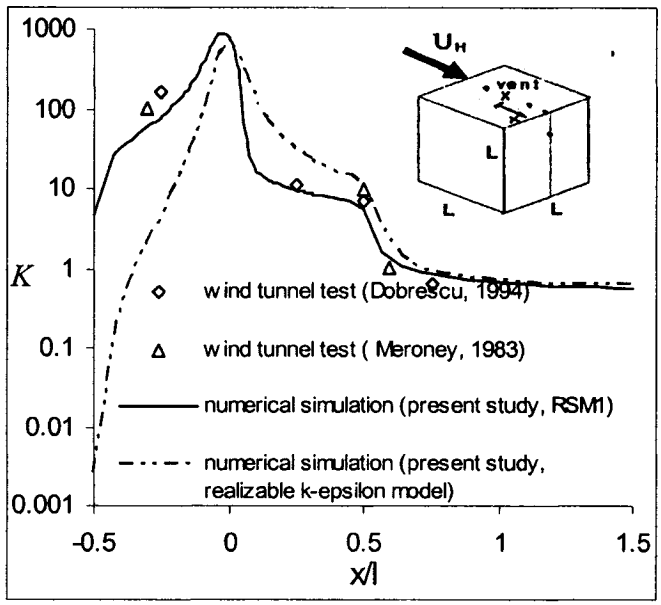

Figure 6.14 K Distributions on Centerline of the Roof and Leeward Wall versus String Distance from Vent Obtained with the RSM1 and Realizable $k-\varepsilon$ Model

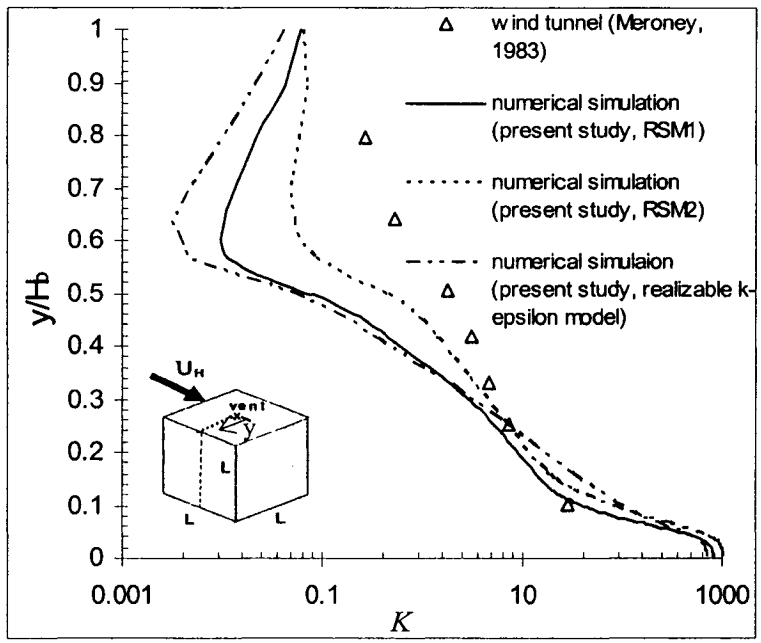

Figure 6.15 Concentration K versus String Distance from Vent between Numerical Results and Wind Tunnel Test Data

The accuracy of the RSM1 model was also evaluated in the near wake of a cubic building using wind tunnel data of Li & Meroney (1983). Fig. 6.16 and Fig. 6.17 show the contours of plume concentration value K in the near wake region of the building (at $x/H_b = 1.0$ and $x/H_b = 4.0$ respectively). The numerical simulation and wind tunnel produces similar maximum concentration values. However, the lateral dispersion was underestimated by the numerical model.

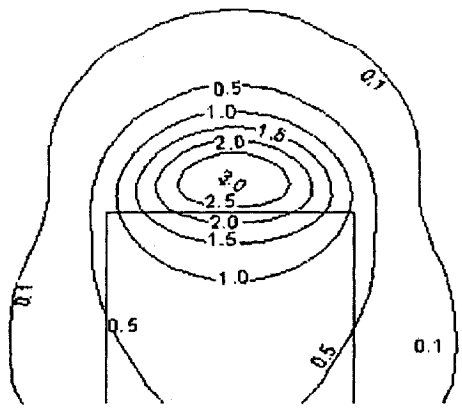

(a)

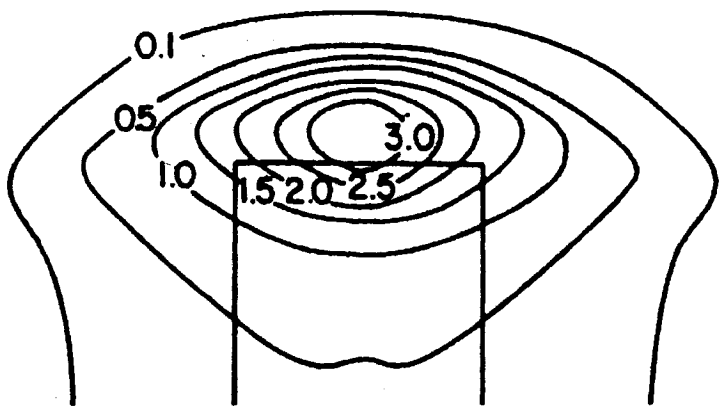

(b)

Figure 6.16 Distribution of Dimensionless Concentration (K) in a Vertical Plane in the near wake Region ($x/H_b = 1.0$) for a Central Flush Stack (wind direction is normal to the building) (a) Numerical Model (RSM1) (b) Wind Tunnel (Li & Meroney, 1983)

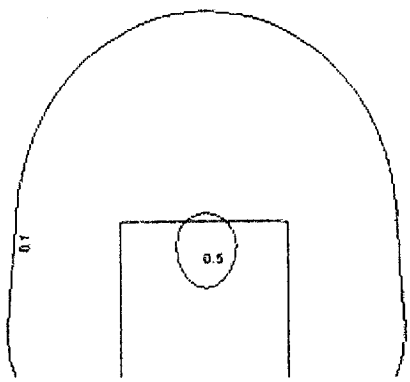

(a)

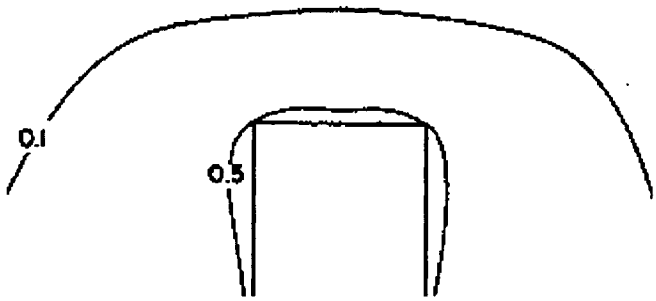

(b)

Figure 6.17 Distribution of Dimensionless Concentration (K) in a Vertical Plane in the near wake Region ($x/H_b = 4.0$) for a Central Flush Stack (wind direction is normal to the building) (a) Numerical Model (RSM1) (b) Wind Tunnel (Li & Meroney, 1983)

The effect of turbulent Schmidt number on the lateral diffusion of the plume was evaluated. As mentioned in chapter 2, previous studies have shown that the value of Sc affects the numerical results. According to Koeltzsch (2000), this number is height dependent in the atmospheric boundary layer and varies from 0.3 to 1.0 based on previous experimental data. However, only constant value can be used for this parameter in FLUENT 6.1. In Tang's (2005) numerical study of atmospheric dispersion over an open field, the value of 1.0 was used. On the other hand, Riddle (2004) found that turbulent Schmidt number 0.3 gave better agreement with experimental data. In the

present study, the influence of this parameter was investigated. If Sc_t decreases, the value of the mass diffusivity term in the pollutant transport equation (2-17) will increase. Comparing Fig. 6.9 and Fig. 6.18 with Fig. 6.8, it is found that results using turbulent Schmidt number 0.3 give better agreements with the wind tunnel data than those using turbulent Schmidt number 0.7. For example, turbulent Schmidt number 0.7 gives much a much thinner shape of the contours of K values on the roof than using turbulent Schmidt number of 0.3. The contour of $K=100$ extends upwind to 1/8 of the length of the building using turbulent Schmidt number 0.7, while the same contour extends upwind to 1/4 of the length of the building for wind tunnel test and the model with turbulent Schmidt number 0.3. The higher value of Sc_t appears to reduce the lateral spread of the plume. Consequently, higher concentrations were observed on the back wall of the building.

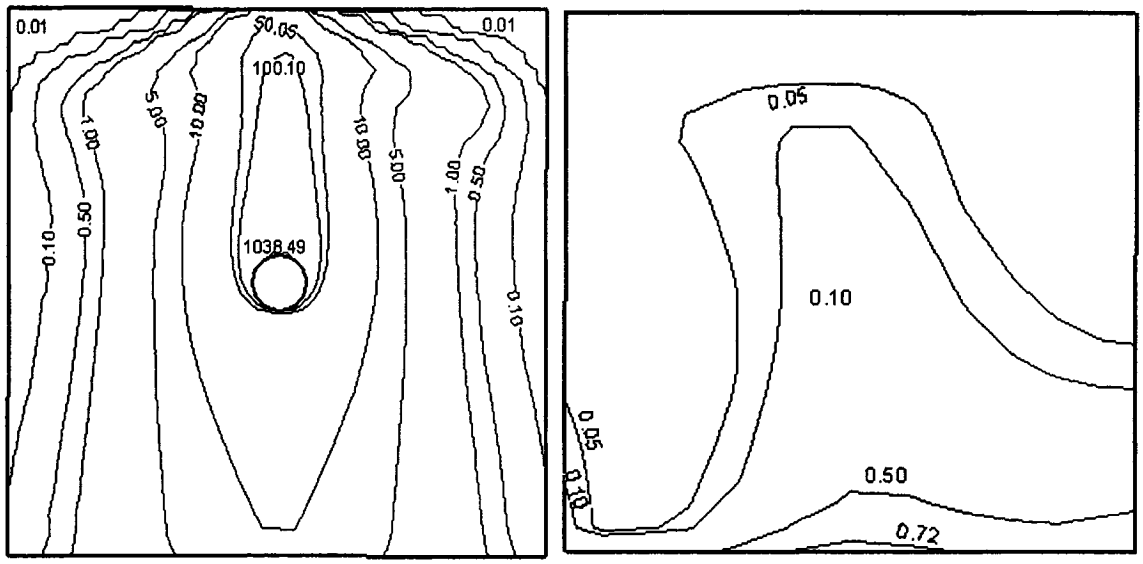

(a) (b)

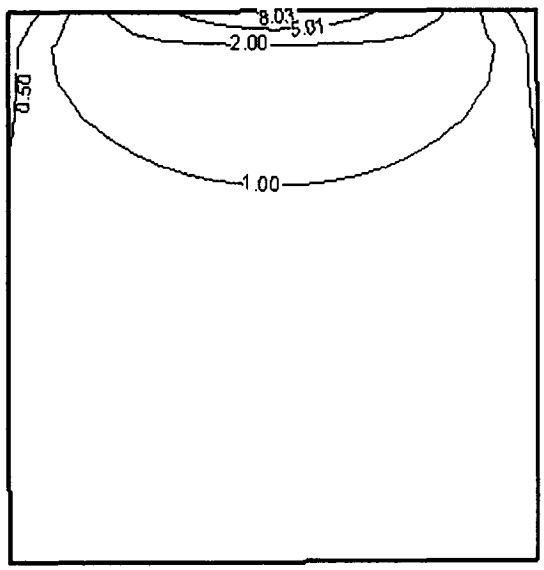

(c)

Figure 6.18 Contour of Dimensionless Concentration K on the (a) Top (b) Side (c) Back of the Cubic Building Obtained with RSM1 Numerical Model and Turbulent Schmidt number 0.7

CHAPTER 7 DISPERSION AROUND A RECTANGULAR BUILDING WITH ROOFTOP STRUCTURES

7.1 Introduction

In a previous study, Stathopoulos et al. (2003) investigated the dispersion of exhaust from rooftop stacks on a low–rise building in an urban environment. Field and wind tunnel experiments were carried out to determine the influence of exhaust momentum ratio, stack height and upstream fetch on plume behavior.

In the present study, CFD simulations of some of the experiments of Stathopoulos et al. (2003) were performed using a simplified configuration. Due to the difficulties in upwind structures in the computational domain, numerical modeling of the flow over an isolated building was carried out. Thus, it is assumed that upwind structures did not significantly affect plume behavior.

Dispersion of emissions from a stack SL4 was studied. A 3-D diagram showing dimensions of the BE building and location of the stack is provided in Figure 7.1. The location of the building and upwind conditions are shown in Appendix E.

Minimum dilution factors predicted by empirical models recommended by ASHRAE (2003) and Wilson-Lamb (1994) will be compared with the numerical results. Field tests and wind tunnel test data of Stathopoulos et al. (2003) will be used to evaluate the numerical predictions.

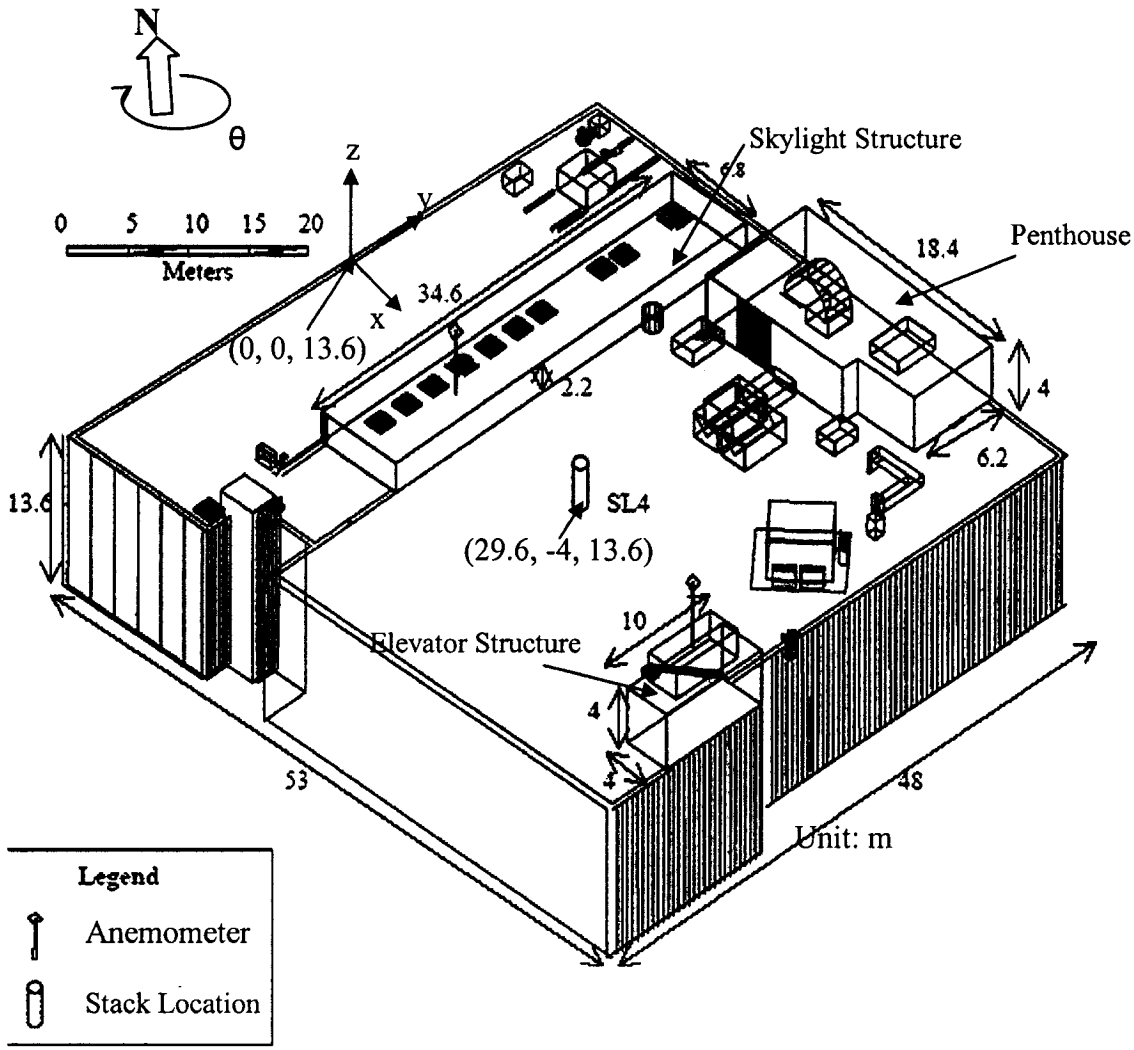

Figure 7.1 Dimensions of the BE Building (after Stathopoulos et al., 2003)

7.2 Numerical Simulation

7.2.1 Pre-processor

1) The computational domain (Fig. 7.2)

In the numerical simulation, the BE building is simplified by ignoring all the small-sized rooftop structures. Only the three largest rooftop structures: skylight structure, penthouse and elevator structure were considered. The scale used in the numerical simulation is 1:200. For the computational domain, the distance upwind of the

building was 0.435 m (6.4 H_b); the distance downwind of the BE building was 1.000 m (14.7 H_b); the lateral distance between the side walls of the building and the computational domain was 0.51 m (7.5 H_b). The height of computational domain was 0.65 m (9.5 H_b).

2) Grid generation

For areas around the BE building, the Hex/Map mesh type was used. For the roof and rooftop structures, the Hex/Wedge Copper mesh type was used. In order to accurately monitor viscous effect near the wall, denser meshes are used near the floor, building walls and areas around the exhaust outlet. The various mesh resolutions are listed in Appendix E. The meshes from the top, side and front views are shown in Fig. 7.3.

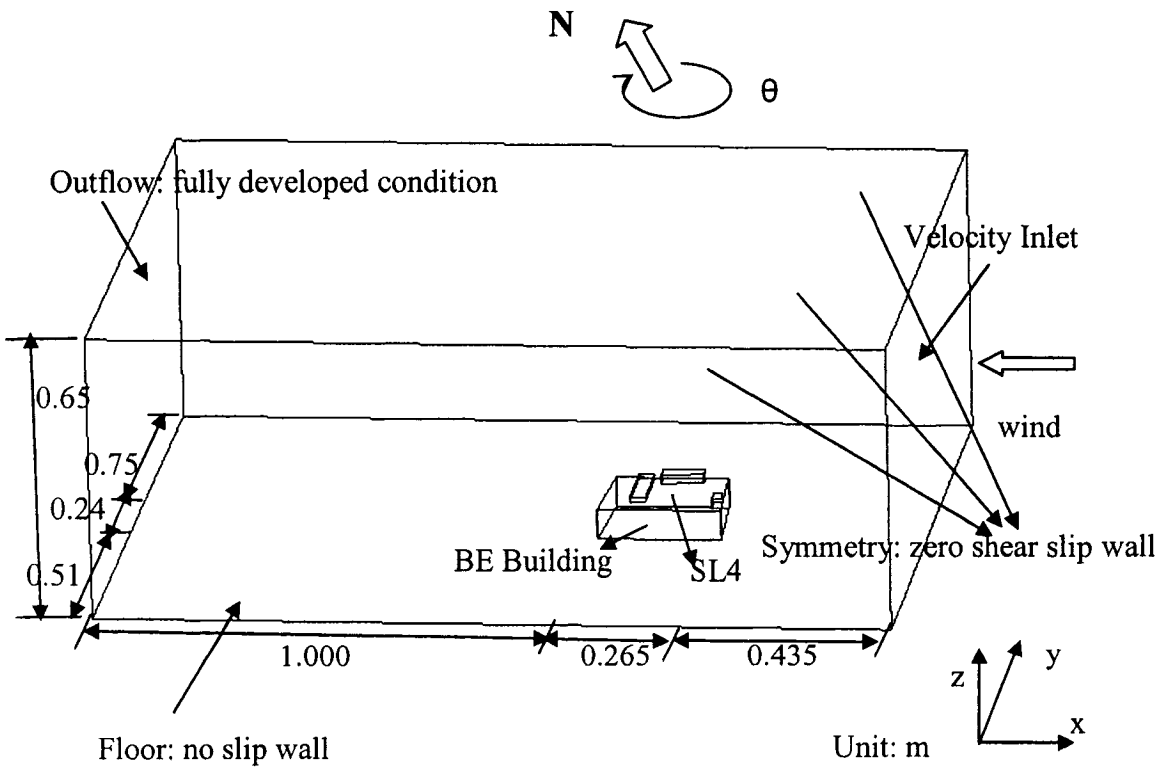

Figure 7.2 Computational Domain and Boundary Conditions for the Stack SL4 Test (θ=120^0)

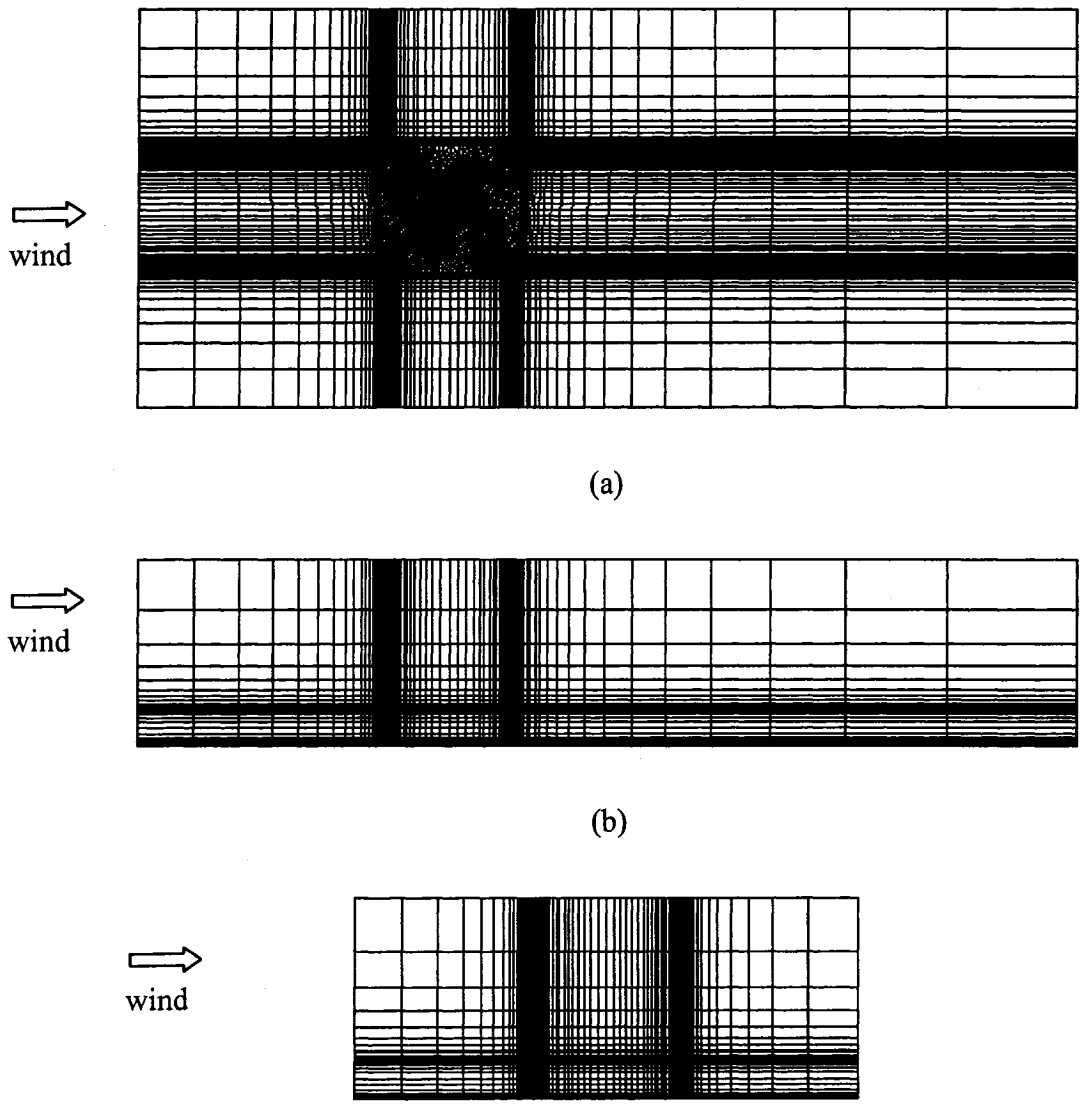

Figure 7.3 Mesh Distributions from (a) Top View (x - y plane) (b) Side View (x - z plane) (c) Front View (y - z plane)

3) Specifications of boundary conditions (Fig. 7.2)

a) The turbulent boundary layer profile from the wind tunnel test was specified at the velocity inlet and shown in Fig. 7.4. An urban area wind profile $U(z) = 15.13\,(z)^{0.32}$ was used. Profiles of turbulent kinetic energy

$k = \frac{3}{2}(U(z) \cdot I(z))^2$ (where $I(z)$ was from the wind tunnel tests, as shown in Fig. 7.4) and dissipation rate $\varepsilon = C_\mu^{\frac{3}{4}} k^{\frac{3}{2}} / l$ (where l is the length scale from the wind tunnel test) were also specified at the inlet as a User Defined Function (UDF) in FLUENT 6.1. The detailed program is listed in Appendix F

b) The wind direction is southeast (θ = 120^0) for stack SL4

c) The diameter for exhaust source SL4 is 0.4 m; The height of the stack SL4 is 1 m

d) The momentum ratios of 5.6, 8.7 and 10.5 are tested for stack SL4

e) Symmetry was set at the sides and top of the calculated domain, which means no flux through these surfaces

f) No-slip condition was applied to the floor and building walls

g) Outflow was set at the exit

h) Initial exhaust molar fraction at the exhaust outlet was 10 ppm (i.e.1e-05)

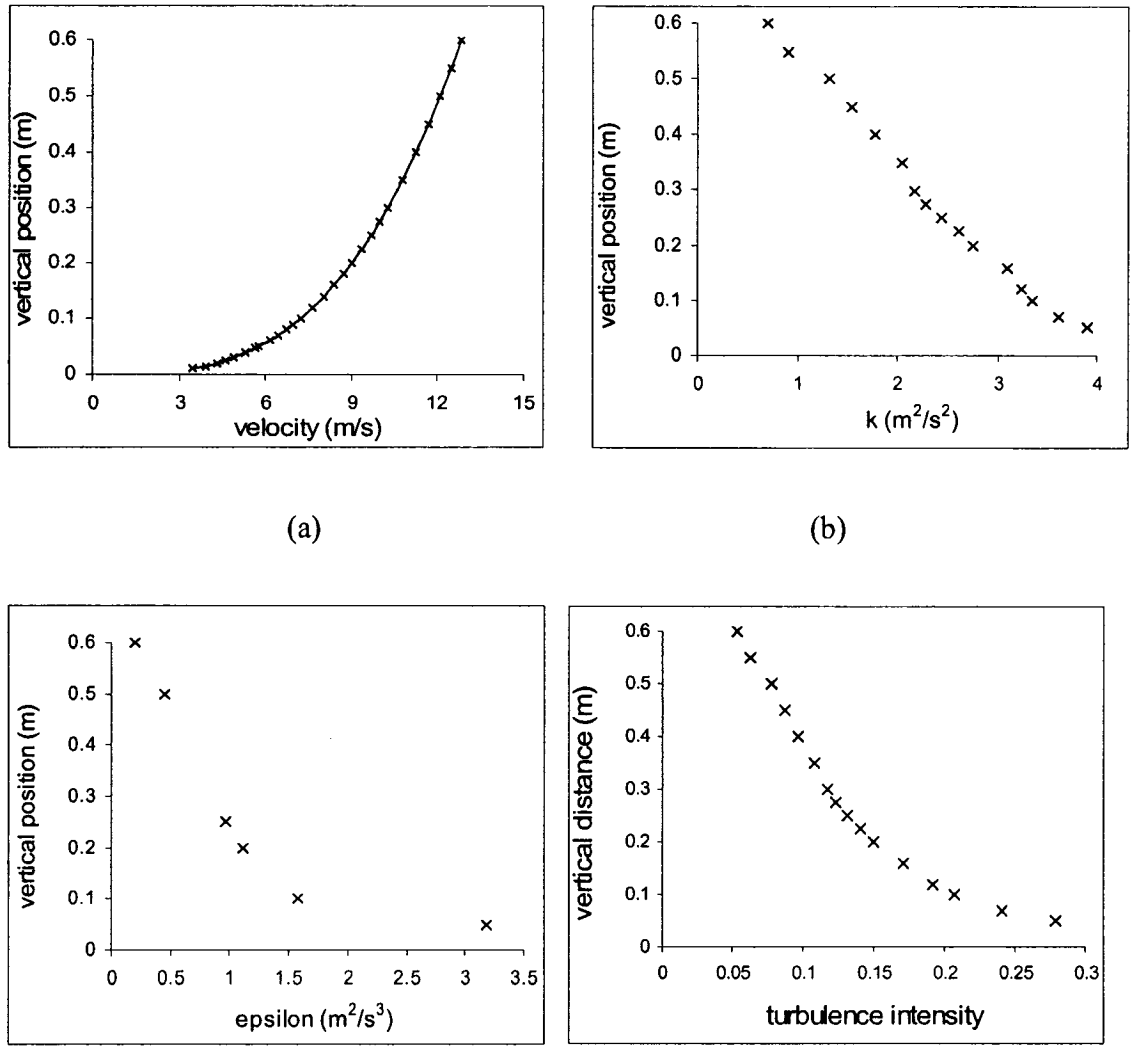

Figure 7.4 CFD Boundary Conditions (a) Velocity Profile (b) Turbulent Kinetic Energy Profile (c) Turbulent Dissipation Rate (d) Turbulence Intensity at the Velocity Inlet

7.2.2 Solver

A segregated solver (Fig. 2.1) was used in this case study. Some critical parameters are mentioned here:

1) The momentum equations were solved by the realizable $k-\varepsilon$ turbulence model with the enhanced wall treatment

2) Convection fluxes were discretized using QUICK

3) The SIMPLE method was used for coupling pressure and velocity

4) The convergence criteria were set to "scaled" residual of 10^{-4}

7.2.3 Post-processor

For comparison with experimental data, concentrations have been expressed in terms of the dimensionless concentration K (equation (6-1)) at the specified receptors. For comparison with the ASHRAE (2003) formula and Wilson-Lamb (1994) formula, the numerical solution is expressed in terms of the minimum dilution ratio.

Fig. 7.5 shows the receptor locations for emissions from the stack SL4. The coordinates of all receptor locations are listed in Appendix E.

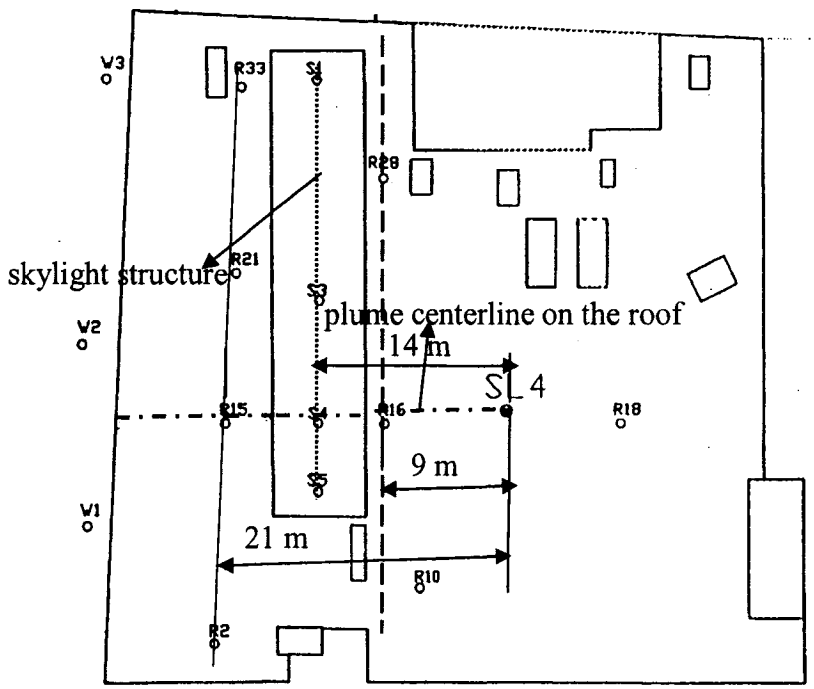

Figure 7.5 Receptor Locations for Case Study with Stack SL4

7.3 Results and Discussion

7.3.1 Parametric Studies

Table 7-1 shows 9 parametric studies of dispersion of emissions from stack SL4. The objective of these parametric studies is to find the effects of the wall treatment methods, turbulence models and some important parameters, such as turbulent Schmidt number, on the fluid field and concentration distribution around the building.

Test series	Mesh size	Turbulent Schmidt number	Turbulence model	Wall treatment	Residual level for concentration	Running time (hour)
1	537,350	0.7	Realizable $k-\varepsilon$	Enhanced wall treatment on the roof	10^{-4}	8
2	477,204	0.7	Realizable $k-\varepsilon$	Standard wall function for all the walls	10^{-4}	8
3	537,350	0.7	Standard $k-\varepsilon$	Enhanced wall treatment on the roof	10^{-4}	8
4	537,350	0.5	Realizable $k-\varepsilon$	Enhanced wall treatment on the roof	10^{-4}	8
5	537,350	0.9	Realizable $k-\varepsilon$	Enhanced wall treatment on the roof	10^{-4}	8
6	537,350	varied	Renormalizable (RNG) $k-\varepsilon$	Enhanced wall treatment on the roof	10^{-4}	8
7	477,204	0.7	Realizable $k-\varepsilon$	Non-equilibrium wall function for all the walls	10^{-5}	8
8	537,350	0.7	Reynold Stress Model	Enhanced wall treatment on the roof	Diverge	2
9	517,348	0.7	Realizable $k-\varepsilon$	Enhanced wall treatment on the roof	10^{-5}	8

Table 7-1 Parametric Studies of Dispersion of Emissions from the Stack SL4 (M = 10.5)

The effects of the enhanced wall treatment and wall function approaches were studied. In the enhanced wall treatment approach, fine meshes were used on the building roof and coarse meshes were used on the floor, walls of the building sides and rooftop structures. The total mesh size at this step is 537,350.

Fig. 7.6 shows the recirculation zones around the BE building and the skylight structure. The recirculation length (L_c) is calculated from the separation position to the attached position where fluid has 0 velocity magnitude in the x direction. The height of the recirculation zone is expressed as H_c.

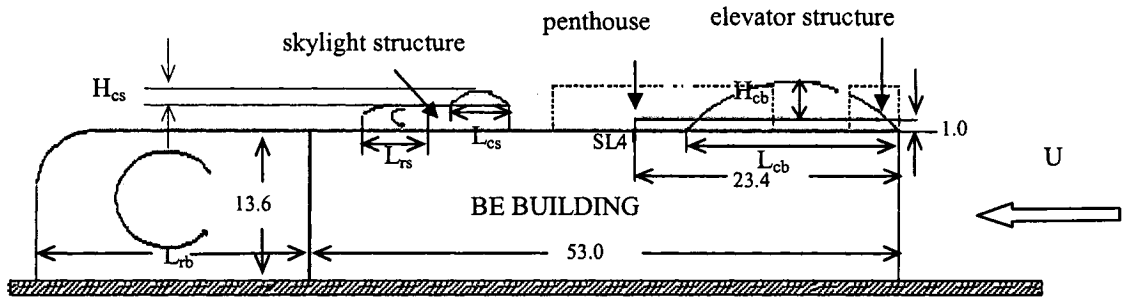

Figure 7.6 Recirculation Zones around the BE building and the Skylight Structure (L_{cb}, L_{cs} , H_{cb} and H_{cs} are the length and height of recirculation zones induced by roof edges of the BE building and the skylight structure, respectively; L_{rb} and L_{rs} are the length of wake zones behind the BE building and the skylight structure, respectively)

The effect of the wall treatments on the recirculation zones for the plane of y = 0 is shown in the Table 7-2. It can be seen the enhanced wall treatment can predict the recirculation zones near the windward edge of the BE building and the skylight. However, it underestimates both the length and height of the recirculation zones near the windward edge and overestimated the length of the recirculation zones in the wake of the building compared with ASHRAE (2003). No recirculation zones can be predicted by the

wall function method. For the recirculation zones in the near wake of the BE building and the skylight, the predicted size from the wall function methods is smaller than that from the enhanced wall treatment.

	L_{cb} (m)	L_{cs} (m)	L_{rs} (m)	L_{rb} (m)	H_{cb} (m)	H_{cs} (m)
Enhanced wall treatment	5.4	1	7.6	44	0.6	0.4
Standard wall function	0	0	5.6	35	0	0
Non-equilibrium wall function	0	0	4.8	38	0	0
ASHRAE (2003)	18.1	5.0	5.5	20.1	4.4	1.1

Table 7-2 Effect of the Realizable k - ε Model with Different Wall Treatments on the Length and Height of the Recirculation Zones (Fig. 7.6) for the Case of Emissions from Stack SL4

The effect of the realizable, standard, and RNG $k-\varepsilon$ models with the enhanced wall treatment on the recirculation zones for the plane of y = 0 is shown in the Table 7-3. The realizable $k-\varepsilon$ model can predict the recirculation zone near the windward edge of the skylight structure, while the standard and RNG $k-\varepsilon$ models could not. All the three turbulence models underestimated both the length and height of recirculation zones near the windward edge of the structures and overestimated the length of the recirculation zones in the wake of the structures compared with ASHRAE (2003). However, the predicted length of the recirculation zone in the wake of the building using the realizable $k-\varepsilon$ model with enhanced wall treatment is closer to that calculated from equation (4-5), which was developed by Hosker (1980).

	L_{cb} (m)	L_{cs} (m)	L_{rs} (m)	L_{rb} (m)	H_{cb} (m)	H_{cs} (m)
Realizable k-ε model	5.4	1	7.6	44	0.6	0.4
Standard k-ε model	6	0	7	42	0.4	0
RNG k-ε model	7.8	0	8	38	0.9	0
ASHRAE (2003)	18.1	5.0	5.5	20.1	4.4	1.1

Table 7-3 Effect of Different Turbulence Models with the Enhanced Wall Treatment on the Length and Height of the Recirculation Zones (Fig. 7.6) for the Case of Emissions from Stack SL4

Fig. 7.7 (a) shows the minimum dilution ratios, obtained from different turbulence models, on the roof for emissions with the momentum ratio 10.5 from the 1 m tall stack SL4. It is noted that there is no data for sampling points from 10 m to 16.8 m because the plume centerline at the roof level is interrupted by the skylight structure. There is little difference between the dilution results from the realizable k- ε model and standard k-ε model. Both models predict the similar trend of the dilution variation with x on the roof as that ASHRAE (2003) D_r model does. The high dilution ratio locates at the positions closer to the stack and then it decreases as the receptors are further away from the stack. That means, for points near the stack, the concentration is very low due to plume rise initially and then more plumes will deposit at the positions further away from the emission source SL4 along the longitudinal direction due to building downwash. However, the D_{min} model (Wilson-Lamb, 1994, B1= 0.059) predicts the opposite trend of the maximum concentration distribution on the roof. The differences between the ASHRAE (2003) and D_{min} (Wilson-Lamb, 1994) model decrease as the receptors become

further away from the stack. Numerical results are more conservative than the ASHRAE (2003) model, but less conservative than the D_{min} model.

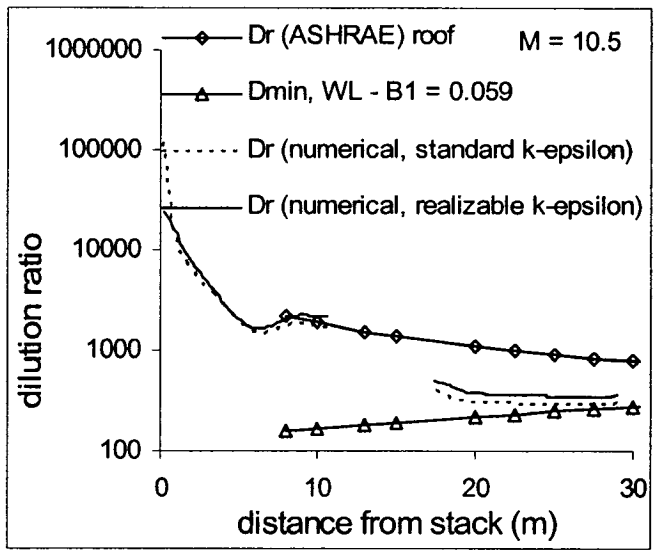

(a)

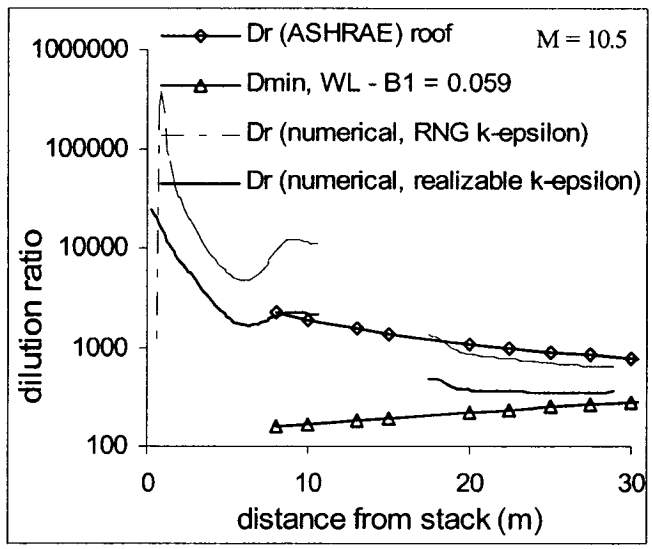

(b)

Figure 7.7 Minimum Dilution versus Distance from Stack SL4 (a) the Realizable k - ε Model and Standard k - ε Model (b) the Realizable k - ε Model and RNG k - ε Model (turbulent Schmidt number 0.7)

Fig. 7.7 (b) shows the effect of RNG $k-\varepsilon$ model on the D_{min} values on the roof. For receptors closer to the stack (distance less than 10 meters), the RNG $k-\varepsilon$ model overestimates the D_{min} values and is thus unconservative. For receptors more than 17 meters far away from the stack, the RNG $k-\varepsilon$ model gives the values closer to the field data and ASHRAE data.

The last test in Table 7-1 was conducted for a case study without three rooftop structures. The effect of rooftop structures, such as the skylight structure, on the dimensionless concentration (K) distributions on the rooftop is shown in Fig. 7.8. Comparing Fig. 7.8 (a) with (b), it can be found that the location and magnitude of the maximum K on the rooftop are not affected much by the skylight structure. However, the plume spread and concentrations in the wake of the skylight structure increases. Without the skylight structure, the plume shape is approximate Gaussian distribution. With the skylight structure, the recirculation zone is generated around the lateral side of the skylight structure. It changes the plume shape to non-Gaussian distribution. More plumes are pulled to the recirculation zone.

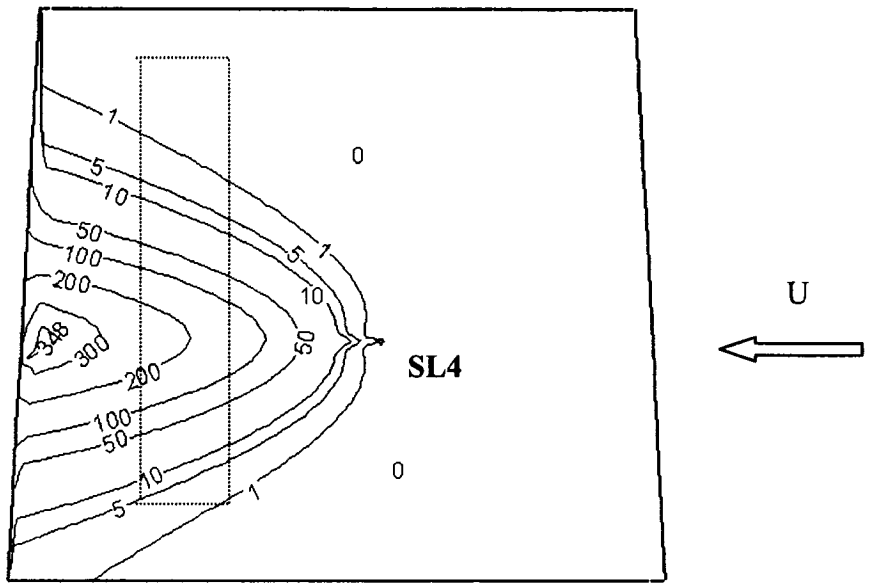

(a)

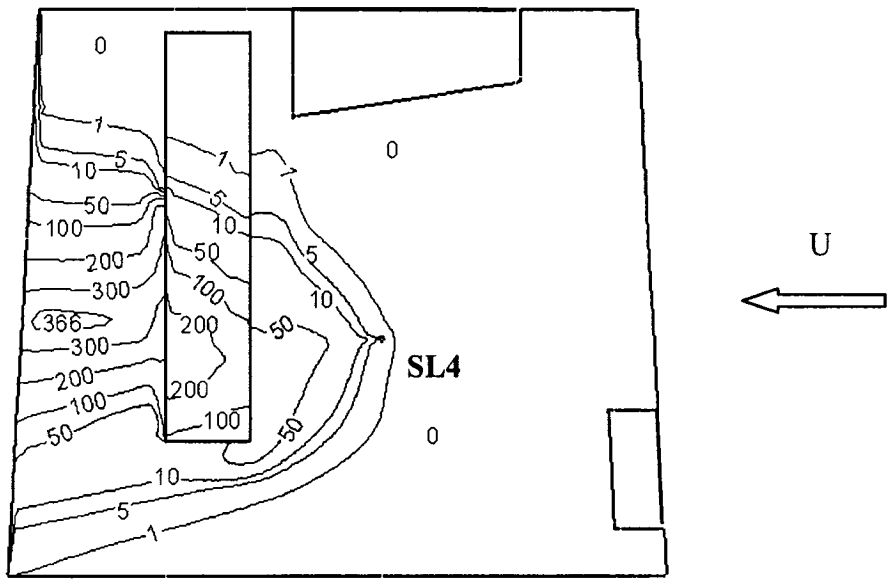

(b)

Figure 7.8 K Distributions on the Rooftop (a) Without the Skylight Structure (b) With the Skylight Structure Using the Realizable $k-\varepsilon$ Model for M = 10.5

Fig. 7.9 shows the effect of turbulent Schmidt number on the dilution ratio on the plume centerline (see Fig. 7.5). Dilution ratios calculated from empirical formulas, ASHRAE (2003) and Wilson-Lamb (1994) are also shown for comparison. The numerical simulation with turbulent Schmidt number 0.7 agrees reasonably well with the ASHRAE (2003) data, but not well with Wilson-Lamb (1994) data. For point R16 (10 m away from the stack), as turbulent Schmidt number increases from 0.7 to 0.9, the dilution ratio value increases from 2,219 to 6,234 and the relative error between the numerical results and ASHRAE (2003) data increases from +17% to +230%. As turbulent Schmidt number increases from 0.5 to 0.7, the dilution ratio value increases from 772 to 2,219 and the relative error between the numerical results and ASHRAE (2003) data increases from -60% to +17%. As the distance from the stack increases, the effect of this parameter decreases.

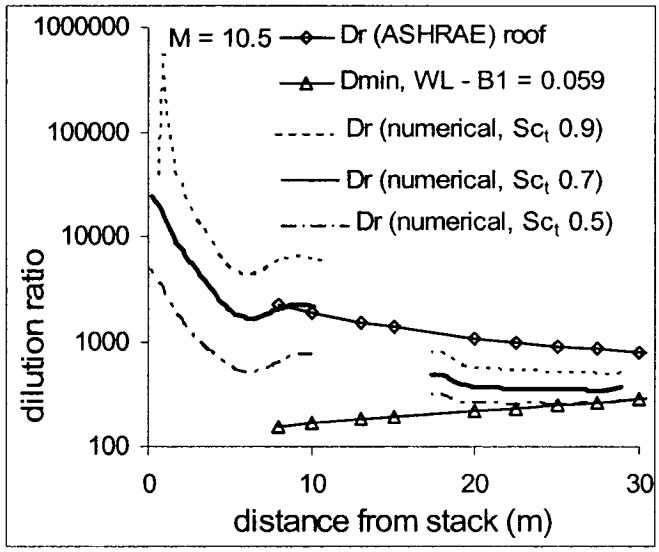

Figure 7.9 Effects of Turbulent Schmidt Number on the Dilution Ratio of Emissions from Stack SL4 Using the Realizable $k-\varepsilon$ Model

7.3.2 Longitudinal Dispersion Results on the Roof Centerline for Emissions from Stack SL4

Based on the above the parametric studies, the realizable $k-\varepsilon$ model with enhanced wall treatment and turbulent Schmidt number 0.7 predicted good minimum dilution ratios on the roof better than the other models. The results from this optimum simulation for the momentum ratio of 5.6, 8.7 and 10.5 are shown in Fig. 7.10. For the following discussion, all numerical results are based on this optimum numerical modeling.

From Fig. 7.10, it can be seen increasing the momentum ratio increases the effective height of the plume. Thus, the concentration on the rooftop decreases and the dilution ratio increases. However, increasing the momentum ratio does not cause the dilution ratio to increase greatly for receptors far away from the stack (distance larger than 17 m in this case).

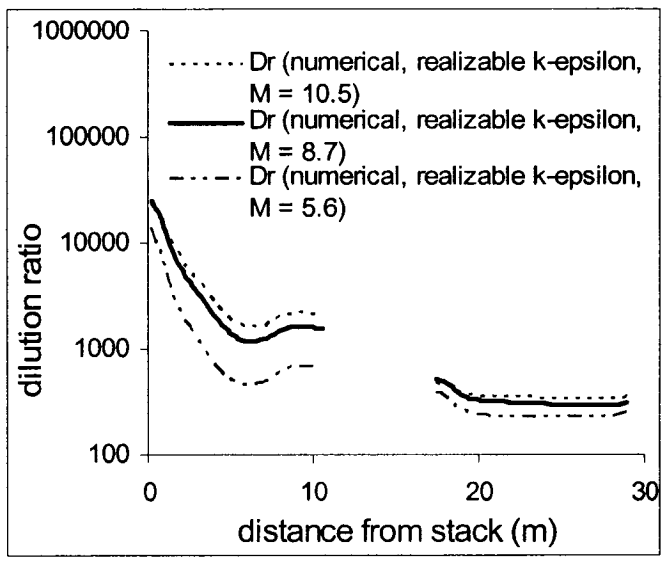

Figure 7.10 Comparisons of Dilution Ratios on the Plume Centerline Using the Realizable $k-\varepsilon$ Model with Enhanced Wall Treatment and Turbulent Schmidt Number 0.7 for M = 5.6, 8.7 and 10.5

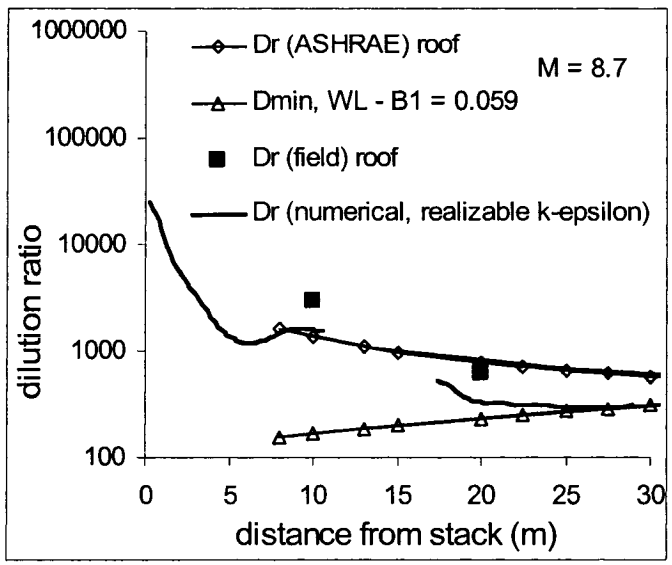

Figure 7.11 Comparisons of Dilution Ratios on the Plume Centerline between Numerical Model Using the Realizable $k-\varepsilon$ Model with Enhanced Wall Treatment and Turbulent Schmidt Number 0.7 and Empirical Formula for M = 8.7

The comparison of numerical results with field test data, ASHRAE (2003) and Wilson – Lamb (1994) models are shown in Fig. 7.11. The numerical model underestimates the dilution ratios for the receptors R15 and R16 by -45% compared with the field data.

7.3.3 Lateral and Vertical Dispersion Results for Emissions from Stack SL4

The numerical concentration distributions for M = 8.7 on the roof, back wall and skylight structure are shown in Fig. 7.12 and compared with field test data. The numerical results agree general well with the field test data along the plume centerline (R15, R16, S4, R18) at the roof level. Comparing the numerical values of R2 (1) and R21 (2) with the corresponding field test data of 135 and 129, it is found that plumes spread is less on the roof in the numerical simulation than that in the field test. The possible reason is from the isotropic numerical models used here.

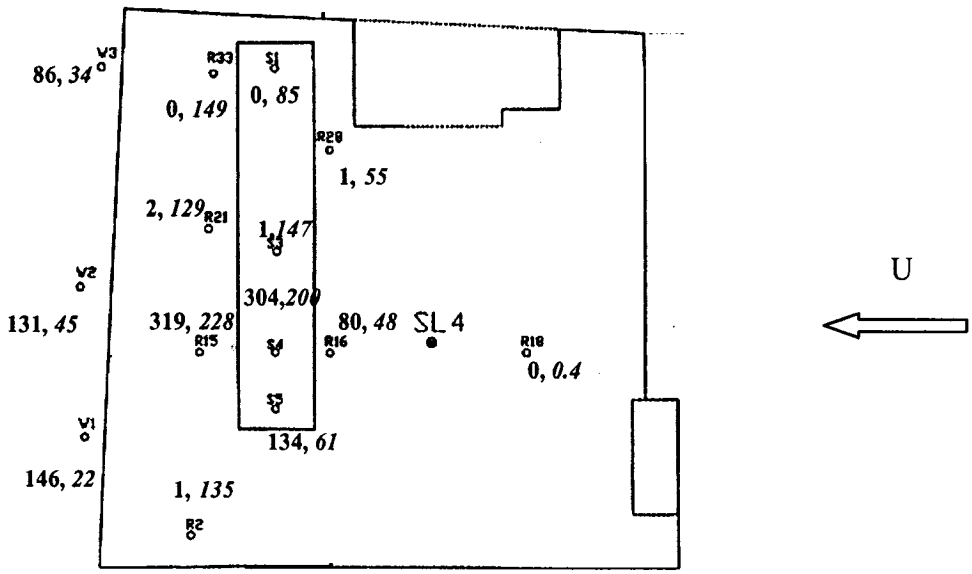

Figure 7.12 Comparison of Concentration Distribution of the Specified Receptors between Field Test (Italic) and Realizable $k-\varepsilon$ Model (Bold) for M = 8.7

It can be seen that the above numerical model overestimated the concentration on the back wall. Because of the lack of lateral spread of the plume above the roof, there is more material available to be captured in the near wake. The plume was evenly distributed by the recirculation zone behind of the building. Fig. 7.12 also shows that on the roof, more of the plume deposit further away from the stack.

Fig. 7.13 shows the vertical concentration distributions at the sampling receptors from the numerical simulation obtained with the realizable $k-\varepsilon$ model. Roof level concentration values obtained in the field test are also plotted in the figure for comparison. The effective stack heights for all the receptors are 21 m.

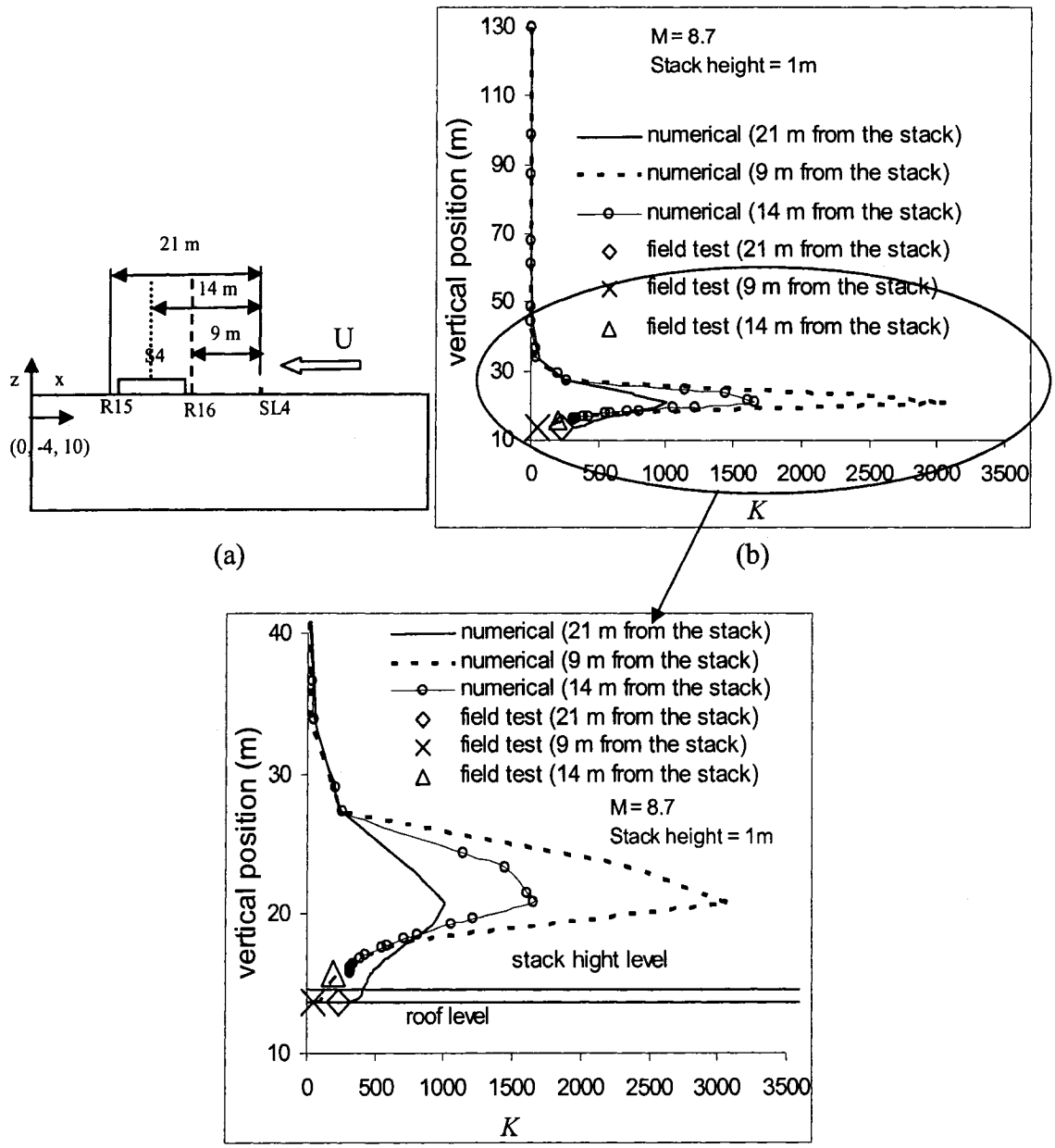

Figure 7.13 (a) Locations of the Specified Receptors (b) Comparisons of Vertical Concentration Distributions at the Specified Receptors between the Numerical Results and Field Test Data

Fig. 7.14 (a) shows the profiles of the crosswind concentration distribution (K) for two lines on the roof. One line is 9 m away from the stack and the other line is 21 m away from the stack (see Fig. 7.5). Crosswind distributions of K in the numerical simulation

do not show the Gaussian shape for the line 9 m away from the stack due to the effect of the skylight structure, as shown in Fig. 7.8. However, it shows the Gaussian shape for the line 21 m away from the stack. It is hard to say if field data show the Gaussian distribution for the two lines or not due to limited data points. Comparing the concentration data on the sampling line 21 m away from the stack, it is found numerical calculation underestimates the plume spread along the lateral direction.

Fig. 7.14 (b) shows the crosswind concentration distributions for the above two sampling lines and the skylight center line at the effective height of 21 m from the numerical simulation with the realizable $k-\varepsilon$ model. The skylight center line is through the points, S1, S3, S4 and S5. It is found that the concentration distributions are Gaussian-shaped. At the rooftop level, the concentration values on the sampling line 21 m away from the stack are larger than those on the sampling line 9 m away from the stack. On the other hand, at the effective height level, the concentration values on the sampling line 9 m away from the stack are larger than those on the sampling line 21 m away from the stack.

Fig. 7.15 shows the vertical concentration distribution in the wake of the building by the numerical method. Building downwash effects on the maximum concentration position can be seen clearly. More than 120 m away from the back wall, the maximum concentration occurs at ground level.

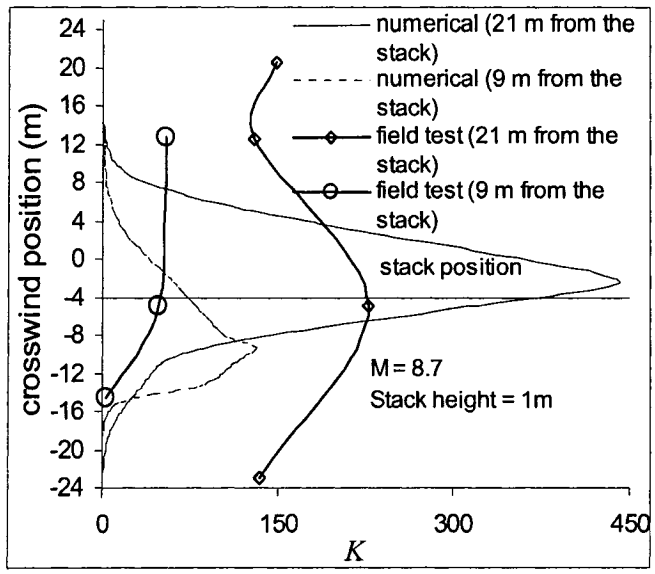

(a)

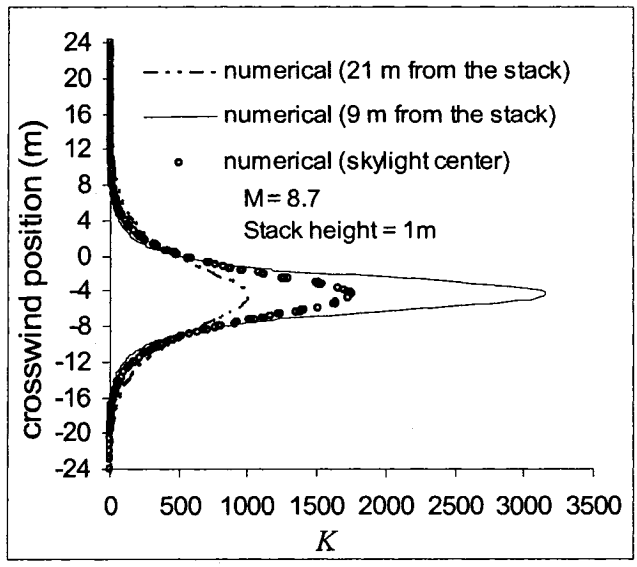

(b)

Figure 7.14 (a) Comparisons of Crosswind Concentration Distributions at the Specified Receptors (shown in Fig. 7.5) at the Rooftop Level between Numerical Results and Field Test Data (b) Profiles of Crosswind Concentration Distribution at the Effective Height of 21 m by the Numerical Method

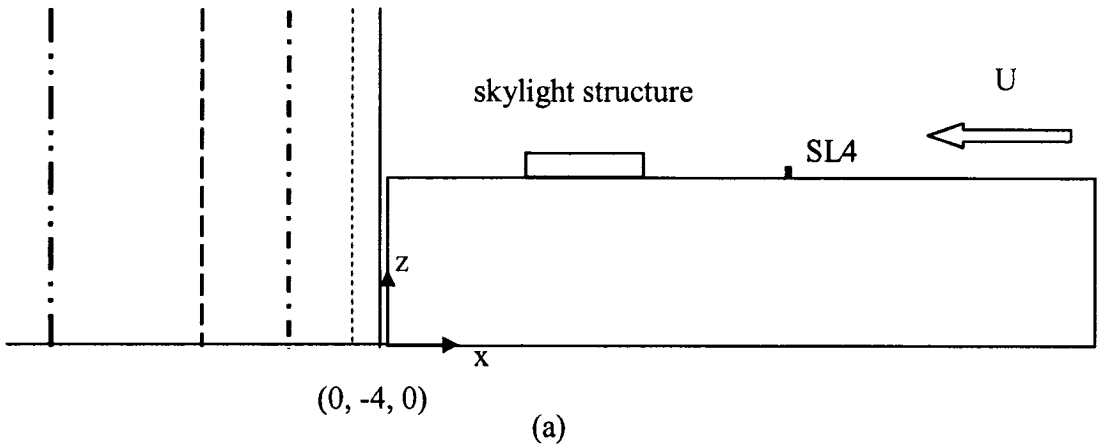

(a)

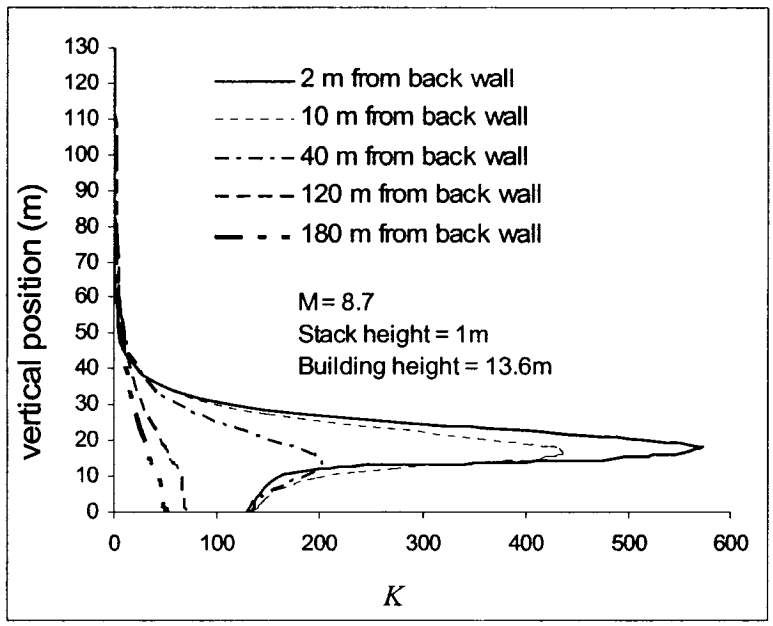

(b)

Figure 7.15 (a) Locations of Specified Receptors in the Wake of the Building (b) Vertical Concentration Distributions by the Realizable $k-\varepsilon$ Model

CHAPTER 8 CONCLUSIONS, CONTRIBUTIONS AND RECOMMENDATIONS

8.1 Conclusions

In the present study, wind-induced plume dispersion in the neutrally stable atmospheric boundary layer (ABL) was simulated using FLUENT 6.1, a commercial computational fluid dynamics (CFD) code. The study investigated three cases: 1) emissions from an isolated stack; 2) emissions from a flush stack on a cubical building; 3) emissions from a rooftop stack on a low-rise building.

1. This study demonstrates that homogenous profiles of velocity and dissipation rate (ε) in the ABL can be simulated by FLUENT 6.1 using an appropriate boundary condition for turbulent kinetic energy k. However, a homogenous profile of k could not be kept throughout the whole computational domain.

2. For plumes emitted from an isolated stack, the present numerical simulation can predict plume behavior using the standard $k-\varepsilon$ model with the standard wall function, except for plume rise. Setting turbulent Schmidt number to 0.7 gives best agreement with experimental data.

3. To accurately simulate the pollutant distribution around buildings, determination of the mean velocity field is not enough. Turbulence parameters, such as kinetic energy, Reynolds stresses, should also be accurately simulated.

4. It is shown in Chapter 6 that the realizable $k-\varepsilon$ model overestimated the kinetic energy around the front edge of a cubical building and underestimated the kinetic energy at the roof center. Due to the underestimation of the recirculation zone at

the windward edge, most of the plume was carried downwind of the rooftop stack, compared with experimental data. Use of the Reynolds stress model produces better results due to improved modeling of the recirculation zone at the windward edge. However, the Reynolds stress model is not easy to converge due to the required high quality meshes. Compared with $k-\varepsilon$ models, it needs more computational resources.

5. Enhanced wall treatment was found to be better than wall functions at predicting the recirculation zone at the windward edge. However, it needs more computational resources than wall functions do.

6. In FLUENT, the isotropic pollutant transportation equation is used to calculate pollutant distributions. This introduces errors since real flows are anisotropic. This may be one reason why the predicted plume spread was much less than that from the experimental tests.

8.2 Contributions

Contributions of the present study are listed below:

1. Three case studies, emissions from an isolated stack, a flush stack located on the rooftop of a cubic building, and a short stack located on the rooftop of a rectangular building, were conducted.

2. Four turbulence models, the standard $k-\varepsilon$ model, RNG $k-\varepsilon$ model, realizable $k-\varepsilon$ model and the Reynolds stress model, combined with three wall treatment methods, standard wall function, nonequilibrium wall function and enhanced wall treatment were tested.

3. The effects of stack height, momentum ratio, and turbulence parameters on the plume trajectory were studied.
4. Parametric study of turbulent Schmidt number was carried out for each case study, to examine the effect it may have on the dispersion.
5. The comparisons between numerical model, empirical model and experimental data are based on not only the predicted centerline concentration but also the lateral and vertical profiles.

8.3 Recommendations for Future Work

Due to time limitation for this program, the present study of wind-induced plume dispersion in the neutral atmospheric boundary layer could not cover all parameters. However, parametric studies provided by the present work are good guides for further studies, which could include the following:

1. One possible solution to the inconsistent k problem between the atmospheric boundary layer and log-law wall function is to add user defined program into FLUENT by following Blocken (2004).
2. The potential power of the Reynolds stress model could be extended to Chapter 7 by optimizing mesh quality and making the solution converged.
3. Anisotropic turbulent diffusivity may be tried to add into FLUENT 6.1 to improve the prediction of the plume lateral spread.
4. Unsteady state flow and dispersion around the building.

REFERENCES

1 Adams, E. W. & Johnston, J. P., Flow structure in the near wall zone of a turbulent separated flow, AIAA Journal, vol. 26, 1998, pp 932-939

2 Arya, S. P., Air Pollution Meteorology and Dispersion, Oxford University Press, New York, 1999

3 ASHRAE, Building air intake and exhaust design, *ASHRAE* Application Handbook, American Society of Heating, Refrigerating and Air-Conditioning Engineers, Atlanta, Chapter 43, 1999

4 ASHRAE, Airflow around buildings, ASHRAE Fundamentals Handbook, American Society of Heating, Refrigerating and Air-Conditioning Engineers, Atlanta, Chapter 16, 2001

5 ASHRAE, Building air intake and exhaust design, *ASHRAE* Application Handbook, American Society of Heating, Refrigerating and Air-Conditioning Engineers, Atlanta, Chapter 44, 2003

6 Banks, D., Meroney, R. N., Petersen, R. L. & Carter, J. J., Evaluation of FLUENT for predicting concentrations on buildings, Air and Waste Management Association Annual Conference, San Diego, CA, 2003, 11pp

7 Barad, M. L. (Editor), Project Prairie Grass. A field program in diffusion. Geophysical Research Paper, No. 59, Vols. I and II, Report AFCRC-TR-58-235, Air Force Cambridge Research Center, Bedford, MA, 1958

8 Becker, S., Ienhart, H. L., & Durst, F., Flow around three dimensional obstacles in boundary layers, Journal of Wind Engineering and Industrial Aerodynamics, Vol. 90, Issues 4-5, May 2002, pp 265-279

9 Blocken, B., Wind-driven rain on buildings, University: Katholieke Universiteit Leuven, Belgium, Ph. D thesis, 2004

10 Blocken, B., Carmeliet, J. & Stathopoulos, T., A numerical study of the wind speed conditions in passages between buildings and the Venturi-effect, 4th European and African Conference on Wind Engineering, Prague, 2005

11 Briggs, G. A., Diffusion estimation of small emissions, Contribution No. 79, Atmospheric Turbulence and Diffusion Laboratory, Oak Ridge, TN, 1973

12 Briggs, G. A., Plume rise, AEC Critical Review Series, Prepared for Nuclear Safety Information Center, 1969

13 Briggs, Plume rise and buoyancy affects, In Atmospheric Science and Power Production. Randerson, D., ed. U. S. Department of Energy DOE/TIC-27601 (DE84005177), Washington, D. C. 1984

14 Castro, I. P. & Robins, A. G., The flow around a surface-mounted cube in uniform and turbulent streams, Journal of Fluid Mechanics, Vol. 79,1977, pp 307-335

15 Castro, I. P. & Apsley, D. D., Flow and dispersion over topography: a comparison between numerical and laboratory data for two-dimensional flow, Atmospheric Environment, Vol. 31, No. 6, 1997, pp 839-850

16 Castro, I. P., CFD for external aerodynamics in the built environment, The QNET-CFD Network Newsletter, Vol. 2, No. 2-July 2003

17 Cebeci, T. & Bradshaw, P., Momentum transfer in boundary layers, Hemisphere Publishing Corporation, New York, 1977

18 Choudhury, D., Introduction to the renormalization group method and Turbulence Modeling, Fluent Inc. Technical Memorandum TM-107, 1993

19 Csanady, G. T., Turbulent diffusion in the environment, D. Reidel Pub. Co., Dordrecht, Holland, 1973

20 Deardorff, J. W., A numerical study of three dimensional turbulent channel flow at large Reyonlds number, J. Fluid Mech., 41, 1970, pp453-480

21 Deardorff, J. W., Three dimensional numerical study of turbulence in an entraining mixed layer, Bound – Layer Meteor., 7, 1974, pp199-226

22 Derardorff, J. W., Numerical integration of neutral and unstable planetary boundary layers, J. Atomos. Sci., 29, 1972, pp91-115

23 Dobrescu, M. A., Effect of mismatching model and boundary layer scales in estimating pollutant dispersion around buildings, M. A. Sc thesis, Concordia University, 1994

24 Dumitrescu-Brulotte, M., Wind pressures on buildings of intermediate height, M. Eng. Thesis, Concordia University, 1987

25 Ehrhard, J., Kunz, R. and Moussiopoulos, N., "On the performance and applicability of nonlinear two-equation turbulence models for urban air quality modeling", Environmental Monitoring and Assessment, Vol. 65, No. 1-2, 2000, pp201-209

26 English, E. C. & Fricke, F. R., The interference index and its prediction using a neural network analysis of wind tunnel data. Fourth Asia Pacific Symposium on Wind Engineering, APSOWE IV University of Queensland, 1997, pp363-366

27 EPA, A user's guide for the Industrial Source Complex (ISC3) dispersion model: Vol. 2-description of model algorithms, EPA-454/b-95-003, U.S. Environmental Protection Agency, Research Triangle Park, NC, 1995

28 Ferziger, J. H. & Peric, M., Computational methods for fluid dynamics, 2nd edition, Springer-Verlag Berlin Heidelberg, 1999

29 Fluent 6.1 User's Guide, Fluent Inc. 2003

30 Flesch, T. K., Turbulent Schmidt number from a tracer experiment, Agricultural and Forest Meteorology, 111, 2002, pp 299-307

31 Flowe, A. C., Development of improved Gaussian dispersion models for cases of downwash past wide buildings using three-dimensional fluid modeling, PH.D thesis, University of Toledo, 1997

32 Franke, J., Recommendations on the use of CFD in predicting pedestrian wind environment, Journal of Wind Engineering and Industrial Aerodynamics (submitted), 2005

33 Fu, S., Launder, B. E., & Leschziner, M. A., Modeling strongly swirling recirculating jet flow with Reynolds-stress transport closures, In Sixth Symposium on Turbulent Shear Flows, Toulouse, France, 1987

34 Gao, Y. & Chow, W. K., Numerical studies on air flow around a cube, Journal of Wind Engineering and Industrial Aerodynamics, 93, 2005, pp115-135

35 Gibson, M. M. & Launder, B. E., Ground effects on pressure fluctuations in the atmospheric boundary layer, J. Fluid Mech., 86, 1978, pp491-511

36 Glanville, M. J. & Al-Khalidy, N. A., Comparison of CFD predictions with wind tunnel & full scale measurements for bounded and unbounded wind flow scenarios, 5th International Colloquium on Bluff Body Aerodynamics and Applications, 2004, Ottawa, Canada

37 Goricsan, I., Balczo, M., Regert, T. & Suda, J. M., Comparison of wind tunnel measurement and numerical simulation of dispersion of pollutants in urban environment, C. OS. T, 2004

38 Guidelines for plume dispersion calculations, Standards and Approvals Div., Department of the Environment, Government of Alberta, 1987

39 Halitsky, J., Gas diffusion near buildings, ASHRAE Transaction 69, 1963, pp 464-485

40 Hall, R. C. (Ed.), Evaluation of modeling uncertainty. CFD modeling of near-field atmospheric dispersion. Project EMU final report, European Commission Diretorate – General XII Science, Research and Development Contract EV5V-CT94-0531, WS Atkins Consultants Ltd., Surrey, 1997

41 Hangan, H., Experimental, numerical and analytical models for a dispersion study, Journal of Aerospace Engineering, Vol. 12, No. 4, October 1999, pp161-167

42 Hanna, S., Briggs, G., & Hosker, R., Handbook on atmospheric diffusion, Jean S. Smith (Editor), 1982

43 Hanna, S., Hansen, O, & Dharmavaram, S., FLACS CFD air quality model performance evaluation with Kit Flox, MUST, Prairie Grass, and EMU observations, Atmospheric Environment, Vol. 38, pp 4675-4687, 2004

44 Haugen, D. A. (Ed), Project Prairie Grass: A field program in diffusion, Geophysical Research Papers, No. 59, Vol. III, Report AFCRC-TR-58-235, Air Force Cambridge Research Center, 1959

45 He, G., The effect of Schmidt number on turbulent scalar mixing in a jet-in-crossflow, International Journal of Heat and Mass Transfer, 42, 1999, pp3727-3738

46 Hinze, J. O., Turbulence, McGraw-Hill Publishing Co., New York, 1975

47 Hosker, R. P., Empirical estimation of wake cavity size behind block-type structures, in preprints of Fourth Symposium on Turbulence, Diffusion, and Air Pollution, Reno, Nev., Jan. 15-18, 1979,pp 603-609

48 Hosker, R. P., Practical application of air pollution deposition models-current status, data requirements, and research needs, in Proceedings of the International Conference on Air Pollutants and Their Effects on the Terrestrial Ecosystem, Banff, Alberta, Canada, May 10-17, John Wiley & Sons, New York, 1980

49 Hosker, R. P., Flow and diffusion near obstacles, Atmospheric science and power production, U. S. Department of Energy DOE/TIC-27601 (DE84005177), 1984

50 Hosker, R. P., Flow around isolated structures and building clusters: A review. ASHRAE Transactions 91 (2b), 1985, pp 1671-1692

51 Huber, A. H. & Snyder, W. H., Wind tunnel investigation of the effects of a rectangular shaped building on dispersion of effluent from short adjacent stacks, Atmospheric Environment, Vol. 16 (12), 1982, pp 2837-2848

52 Jayatilleke, C., The influence of Prandtl number and surface roughness on the resistance of the laminar sublayer to momentum and heat transfer, Prog. Heat Mass Transfer, 1:193-321, 1969

53 Kader, B., Temperature and concentration profiles in fully turbulent boundary layers, Int. J. Heat Mass Transfer, vol. 24(9), 1981, pp1541-1544

54 Kato, M. & Launder, B. E., The modeling of turbulent flow around stationary and vibrating square cylinders, Proc. 9th Symp. On Turbulence and Shear Flows, Kyoto, 1993

55 Kim, K. C., Ji, H. S., & Seung, H. S., Flow structure around a 3-D rectangular prism in a turbulent boundary layer, Journal of Wind Engineering and Industrial Aerodynamics, Vol. 91, Issues 5, April 2003, pp 653-669

56 Kim, S. & Boysan, F., Application of CFD to environmental flows, Journal of Wind Engineering and Industrial Aerodynamics, Vol. 81, 1999, pp145-158

57 Koeltzsch, K., The height dependence of the turbulent Schmidt number within the boundary layer, Atmospheric Environment, 34, 2000, pp1147-1151

58 Launder, B. E. & Spalding, D. B., Lectures in mathematical models of turbulence, Academic Press, London, England, 1972

59 Launder, B. E. & Spalding, D. B., The numerical computation of turbulent flows, Computer Methods in Applied Mechanics and Engineering, 3, 1974, pp269-289

60 Launder, B. E., Reece, G. J. & Rodi, W., Progress in the development of a Reynolds –stress turbulence closure, J. Fluid Mech., 68(3), April 1975, pp537-566

61 Launder, B. E., Second-moment closure and its use in modeling turbulent industrial flows, International Journal for Numerical Methods in Fluids, 9: 963-985, 1989

62 Launder, B. E., Second moment closure: present ... and future? Inter. J. Heat Fluid Flow, 10(4), 1989, pp282-300

63 Leitl, B. M., Kastner – Klein, P., Rau, M. & Meroney, R. N., Concentration and flow distributions in the vicinity of U-shaped buildings: Wind tunnel and computational data, Journal of Wind Engineering and Industrial Aerodynamics, Vol. 67-68, April – June 1997, pp 745- 755

64 Leonard, B. P. & Mokhtari, S., ULTRA-SHARP nonoscillatory convection Sshemes for high speed steady multidimensional flow, NASA TM 1-2568 (ICOMP-90-12), NASA Lewis Research Center, 1990

65 Li, W. & Meroney, R. N., Gas dispersion near a cubical model building, Part I, Mean concentration measurements, J. Wind Engrg, & Ind. Aerodyn. 12, 1983, pp15-33

66 Li, Y. & Stathopoulos, T., Numerical evaluation of wind induced dispersion of pollutants around a building, Journal of Wind Engineering and Industrial Aerodynamics, Vol. 67-68, 1997, pp757-766

67 Lien, F. S. & Leschziner, M. A., Assessment of turbulent transport models including non-linear RNG eddy-viscosity formulation and second-moment closure, Computers and Fluids, 23(8): 983-1004, 1994

68 Lien, F. S., Chen, W. L. & Leschziner, M. A., Low-Reynolds number eddy viscosity modeling based on nonlinear stress-strain/vorticity relations, in W. Rodi, editor, Engineering Turbulence Modelling and Experiments 3, Elsevier, Amsterdam, 1996

69 Martinuzzi, R. & Tropea, C., The flow around surface mounted, prismatic obstacles placed in a fully developed channel flow, Journal of Fluids Engineering, vol. 115, March 1993, pp 85-92

70 McElroy, J. L. & Pooler, F., The St. Louis dispersion study, U.S. Public Health Service, National Air Pollution Control Administration, 1968

71 Melbourne, W. H. Turbulence effects on maximum surface pressures; A mechanism and possibility of reduction. Proceedings of Fifth International Conference on Wind Engineering. J. E. Cermak, ed. Fort Collins, Colorado, 1979, pp541-551

72 Meroney, R. N., Leitl, B. M., Rafailidis, S. & Schatzmann, M., Wind tunnel and numerical modeling of flow and dispersion about several building shapes, Journal of of Wind Engineering and Industrial Aerodynamics, vol. 81, Issues 1-3, May 1999, pp 333- 345

73 Meroney, R. N., Wind tunnel and numerical simulation of pollutant dispersion: a hybrid approach, Invited Lecture, Colorado State University, 2004

74 Murakami, S. & Mochida, A., Three dimensional numerical simulation of turbulent flow around buildings using the $k-\varepsilon$ turbulence model, Building and Environment, vol 24, 1989, pp51-64

75 Murakami, S., Kato, S. & Kondo, Y., Examining $k-\varepsilon$ EVM by means of ASM for a 3-D horizontal buoyant jet in enclosed space, Engineering Turbulence Modelling and Experiments, Elsevier Science Publishing, 1990, pp205-214

76 Murakami, S., Mochida, A. & Hayashi, Y., Scrutinizing $k-\varepsilon$ EVM and ASM by means of LES and wind tunnel for flowfield around cube, 8th Symp. on Turbulent Shear Flows, 1991

77 Murakami, S., Mochida, A., Hayashi, Y., & Sakamoto, S., Numerical study on velocity – pressure field and wind forces for bluff bodies by k- epsilon, ASM, and LES, Journal of Wind Engineering and Industrial Aerodynamics, 41-44, 1992, pp2841-2852

78 Murakami, S., Overview of turbulence models applied in CWE-1997, 2nd European & African Conference on Wind Engineering, Genova, Italy, June 22-26, 1997

79 Norris, L. H. & Reynolds, W. C., Turbulent channel flow with a moving wavy boundary, Report No. FM-10, Stanford University, Department Mechanical Engineering, 1975

80 Nozawa, K., & Tamura, T., Large eddy simulation of the flow around a low-rise building immersed in a rough wall turbulent boundary layer, Journal of Wind Engineering and Industrial Aerodynamics, Vol. 90, Issues 10, June 2002, pp 1151-1162

81 Ogawa, Y., Oikawa, S. & Uehara, K., Field and wind tunnel study of the flow and diffusion around a model cube-II. Nearfield and cube surface flow and concentration patterns, Atmospheric Environment, Vol. 17, No. 6, pp 1161-1171

82 Pasquill, F., & Smith, F. B., Atmospheric Diffusion, 3rd ed. Ellis Horwood Ltd., Chichester, England, 1983

83 Patankar, S. V., Numerical heat transfer and fluid flow, Hemisphere, Washington, D. C., 1980

84 Reynolds, W. C., Fundamentals of turbulence for turbulence modeling and simulation, Lecture notes for Von Karman Institute Agard Report No. 755, 1987

85 Rhie, C. M. & Chow, W. L., Numerical Study of the Turbulent Flow Past an airfoil with Trailing Edge Separation, AIAA Journal, vol.21(11), November 1983, 001525-1532

86 Richards, P.J. & Hoxey, P. P., Appropriate boundary conditions for computational wind engineering models using $k-\varepsilon$ turbulent model, J. Wind. Eng. & Indust. Aero., 46-47, 1993

87 Riddle, A., Carruthers, D., Sharpe, A., McHugh, C. & Stocker, J., Comparisons between FLUENT and ADMS for atmospheric dispersion modeling, Atmospheric Environment, Vol. 38, 2004, pp1029-1038

88 Rodi, W., Applied Mathematical and Mechanics, T219 - T221, 1976

89 Saathoff, P. J., Stathopoulos, T. & Dobrescu, M., Effects of model scale in estimating pollutant dispersion near buildings, Journal of Wind Engineering and Industrial Aerodynamics, Vol. 54-55, February 1995, pp549-559

90 Sarkar, S. & Balakrishnan, L., Application of a Reynolds-stress turbulence model to the compressible shear layer, ICASE Report 90-18, NASA CR 182002, 1990

91 Schulman, L.L. & Hanna, S.R., Evaluation of downwash modifications to the industrial source complex model, J. Air Poll. Control Assoc., 36, 1986, pp 259-264

92 Shih, T.-H., Liou, W.W., Shabbir, A., Yang, Z. & Zhu, J., A new $k-\varepsilon$ eddy viscosity model for high Reynolds number turbulent flows – model development and validation, Computers Fluids, 24(3), 1995, pp 227-238

93 Smagorinsky, J., General circulation experiments with the primitive equations, Monthly Weather Review, Vol. 93, No. 3, 1963, pp99

94 Snyder, W. H., Wind tunnel simulation of building downwash from electric power generating stations, Part I: Boundary layer and concentration measurements, Fluid modeling facility internal Rpt., Code: EPR, Research Triangle Park, NC, 271 pages, 1992

95 Snyder, W. H. & Lawson, R. E., Wind tunnel measurements of flow fields in the vicinity of buildings, 8th Joint Conference on Applications of Air Pollution Meteorology, 1994, pp244-250

96 Snyder, W. H., Streamline patterns around buildings deduced from wind tunnel measurements, PHYSMOD 2005, PP10-11

97 Speziale, C. G., Sarkar, S., & Gatski, T. B., Modelling the pressure-strain correlation of turbulence: An invariant dynamical systems approach, J. Fluid Mech., 227, 1991, pp245-272

98 Stathopoulos, T., Surry, D. & Davenport, A.G., Effective wind loads on flat roofs, Journal of Struct. Div., ASCE, Vol. 107, No. ST2, 1981, Proc. Paper 16039, pp. 281-298

99 Stathopoulos, T. & Baskaran, A., Boundary treatment for the computation of 3-D wind flow conditions around a building, Journal of Wind Engineering and Industrial Aerodynamics, Vol. 35, 1990, pp 177-200

100 Stathopoulos, T. & Zhou, Y., Numerical simulation of wind induced pressures on buildings of various geometries, Journal of Wind Engineering and Industrial Aerodynamics, Vol. 46 & 47, 1993, pp 419-430

101 Stathopoulos, T., Saathoff, P. & Gupta, A., The effect of stack height, stack location and rooftop structures on air intake contamination: A laboratory and full-scale study, IRSST, Quebec, 2003

102 Tang, W., Huber, A., Bell, B., Kuehlert, K. & Schwarz, W., Example application of CFD simulations for short-range atmospheric dispersion over the open fields of Project Prairie Grass, Paper # 1243, A& WMA Conference, 2005

103 Turner, D. B., Workbook of atmospheric dispersion estimates, CRC Press, Inc. 1994,

104 U. S. Environmental Protection Agency, AERMOD: Description of model formulation, EPA-454/R-03-004, 2004

105 Versteeg, H. K. & Malalasekera, W., An introduction to computational fluid dynamics, the finite volume method, Longman Scientific and Technical, 1995

106 White, F. M., Fluid mechanics, McGraw-Hill, United States of America, 1999

107 Wilson, D. J. Flow patterns over flat roofed buildings and application to exhaust stack design, ASHRAE Transactions 85, 1979, pp 284-295

108 Wilson, D. J. & Winkel, G., The effect of varying exhaust stack height on contaminant concentration at roof level, ASHRAE Transactions, 88 (1), 1982, pp 513-533

109 Wilson, D. J., Fabris, I., Chen, J. & Acherman, M. Y., Adjacent building effects on laboratory fume hood exhaust stack design, Final Report, ASHRAE, RP-897, 1986b

110 Wilson, D.J. & Chui, E. H., Effects of turbulence from upwind building on dilution of exhaust gases, ASHRAE Transactions 93(2), 1987, pp2186-2197

111 Wilson, D. J. & Lamb, B. K., Dispersion of exhaust gases from roof level stacks and vents on a laboratory building, Atmospheric Environment, 28, 1994, pp3099-3111

112 Wolfstein, M., The velocity and temperature distribution of one dimensional flow with turbulence augmentation and pressure gradient, Int. J. Heat Mass Transfer, Vol. 12, 1969, pp301-318

113 Yakhot, V. & Orszag, S. A., Renormalization group analysis of turbulence: I. Basic theory. Journal of Scientific Computing 1 (1), 1986, pp1-51

114 Zhang, Y. Q., Arya, S. P. & Snyder, W. H., A comparison of numerical and physical modeling of stable atmospheric flow and dispersion around a cubical building, Atmospheric Environment, Vol 30, No. 8, 1996, pp1327-1345

115 Zhou, Y., Numerical evaluation of wind effects on buildings, PH.D thesis, Concordia University, 1995

APPENDIX A

This appendix gives more details about some parameters adopted in the standard wall function and non-equilibrium wall function. It is an additional part to the section 2.3

A1: Roughness Effects in the Standard Wall Function

The wall function uses semi-empirical algebraic formulae to solve the velocity and turbulent quantities in the viscosity-affected regions between the wall and the fully turbulent region. The standard wall function is based on the proposal of Launder & Spalding (1974). The general formula for mean velocity is:

$$U^* = \frac{1}{k}\ln(Ey^*) - \Delta B \qquad \text{(A-1)}$$

where

$$U^* = \frac{U_p C_\mu^{1/4} k_p^{1/2}}{\tau_w / \rho} \qquad y^* \equiv \frac{\rho C_\mu^{1/4} k_p^{1/2} y_p}{\mu} \qquad \Delta B = \frac{1}{\kappa}\ln f_r$$

and U^* is the dimensionless velocity;

y^* is the dimensionless height;

κ is the von Karman's constant (=0.42);

E is the empirical constant for smooth wall (=9.81);

P is the center point of the wall adjacent cell;

U_p is the mean velocity of the fluid at point P;

k_p is the turbulent kinetic energy at point P;

y_p is the distance from point P to the wall;

τ_w is the shear stress on the wall;

μ is the dynamic viscosity of the fluid;

ΔB is the roughness function;

f_r is a function of roughness that quantifies the shift of the intercept due to roughness.

ΔB depends on the type (uniform sand, rivets, ribs, etc.) and size of the roughness. There is no universal roughness function that is valid for all types of roughness. For a sand-grain roughness and similar types of uniform roughness elements, ΔB is well-correlated with the non-dimensional physical roughness height, K_s^+. ($K_s^+ = \rho K_s C_\mu^{\frac{1}{4}} k^{\frac{1}{2}} / \mu$, where K_s is the physical roughness height, Cebeci & Bradshaw, 1977)

- For the hydrodynamically smooth regime ($K_s^+ \leq 2.25$),

$$\Delta B = 0 \tag{A-2}$$

- For the transitional regime ($2.25 \leq K_s^+ \leq 90$),

$$\Delta B = \frac{1}{\kappa} \ln\left[\frac{K_s^+ - 2.25}{87.75} + C_s K_s^+\right] \times \sin\left\{0.4285(\ln K_s^+ - 0.811)\right\} \tag{A-3}$$

where C_s is a roughness constant that depends on the type of the roughness. The default value is 0.5 in FLUENT 6.1.

- In the fully rough regime ($K_s^+ > 90$),

$$\Delta B = \frac{1}{\kappa} \ln(1 + C_s K_s^+) \tag{A-4}$$

A2: Nonequilibrium Wall Function

Non-equilibrium wall functions are based on the proposal of Kim & Choudhury (1995). The log-law for mean velocity sensitized to pressure gradients is as follows:

$$\frac{\tilde{U} C_{\mu}^{\frac{1}{4}} k^{\frac{1}{2}}}{\tau_w / \rho} = \frac{1}{\kappa} ln(E \frac{\rho C_{\mu}^{\frac{1}{4}} k^{\frac{1}{2}} y}{\mu}) \tag{A-5}$$

where

$\tilde{U} = U - \frac{1}{2}\frac{dp}{dx}[\frac{y_v}{\rho\kappa\sqrt{k}}\ln(\frac{y}{y_v}) + \frac{y - y_v}{\rho\kappa\sqrt{k}} + \frac{y_v^2}{\mu}]$; y_v is the physical viscous sublayer thickness, and is computed from $y_v \equiv \frac{\mu y_v^*}{\rho C_{\mu}^{\frac{1}{4}} k_p^{\frac{1}{2}}}$ (y_v^*=11.25)

The non-equilibrium wall function employs the two-layer concept in computing the budget of turbulent kinetic energy at the wall-adjacent cells. The wall-adjacent cells are assumed to consist of a viscous sublayer and a fully turbulent layer. The profile for turbulence quantities are as follows:

$$\tau_t = \begin{cases} 0 & y < y_v \\ \tau_w & y > y_v \end{cases}, \quad k = \begin{cases} \left(\frac{y}{y_v}\right)^2 k_p & y < y_v \\ k_p & y > y_v \end{cases}, \quad \varepsilon = \begin{cases} \frac{2\nu k}{y^2} & y < y_v \\ \frac{k^{3/2}}{C_l y} & y > y_v \end{cases} \tag{A-6}$$

where $C_l = \kappa C_{\mu}^{-\frac{3}{4}}$.

For quadrilateral and hexahedral cells, the volume average for production of k and dissipation rate $\bar{\varepsilon}$ can be calculated as follows:

$$\overline{G_k} \equiv \frac{1}{y_n}\int_0^{y_n} \tau_t \frac{\partial U}{\partial y} dy = \frac{1}{\kappa y_n}\frac{\tau_w{}^2}{\rho C_\mu{}^{1/4} k_p{}^{1/2}} \ln(\frac{y_n}{y_v}) \tag{A-7}$$

and

$$\bar{\varepsilon} \equiv \frac{1}{y_n}\int_0^{y_n} \varepsilon \, dy = \frac{1}{y_n}[\frac{2\nu}{y_v} + \frac{k_p{}^{1/2}}{C_l} \ln(\frac{y_n}{y_v})] \, k_p \tag{A-8}$$

where y_n is the height of the cell ($y_n = 2y_p$).

For cells with other shapes (e.g., triangular and tetrahedral grids), the appropriate volume averages are used.

In equations (A-7) and (A-8), the turbulent kinetic energy budget for the wall-adjacent cells is effectively sensitized to the proportions of the viscous sublayer and the fully turbulent layer, which varies widely form cell to cell in highly non-equilibrium flows. It effectively relaxes the local equilibrium assumption (production=dissipation) that is adopted by the standard wall function.

APPENDIX B

This appendix describes Pasquill stability categories according to the weather condition. Also the curves of Pasquill – Gifford horizontal and vertical dispersion parameters for Pasquill neutral condition are given.

Insolation				Night	
Surface wind speed (at 10 m) m/s	Strong	Moderate	Slight	Thinly overcast or > 4/8 low cloudiness	<3/8
<2	A	A-B	B	----------	----------
2-3	A-B	B	C	E	F
3-5	B	B-C	D	D	E
5-6	C	C-D	D	D	D
>6	C	D	D	D	D

Table B-1 Pasquill Stability Categories (after Pasquill, 1961)

Note:

1. The degree of cloudiness is defined as that fraction of sky above the local apparent horizon that is covered by clouds
2. Insolation is the rate of radiation from the sun received per unit of earth's surface
3. Strong Insolation corresponds to sunny midday in midsummer in England; slight insolation to similar conditions in midwinter
4. Night refers to the period from 1 hour before sunset to 1 hour after sunrise
5. The neutral category D should also be used, regardless of wind speed, for overcast conditions during day or night and for any sky conditions during the hour preceding or following night as defined above.

6. A - extremely unstable; B - moderately unstable; C - slightly unstable; D - neutral; E - slightly stable; F - moderately stable

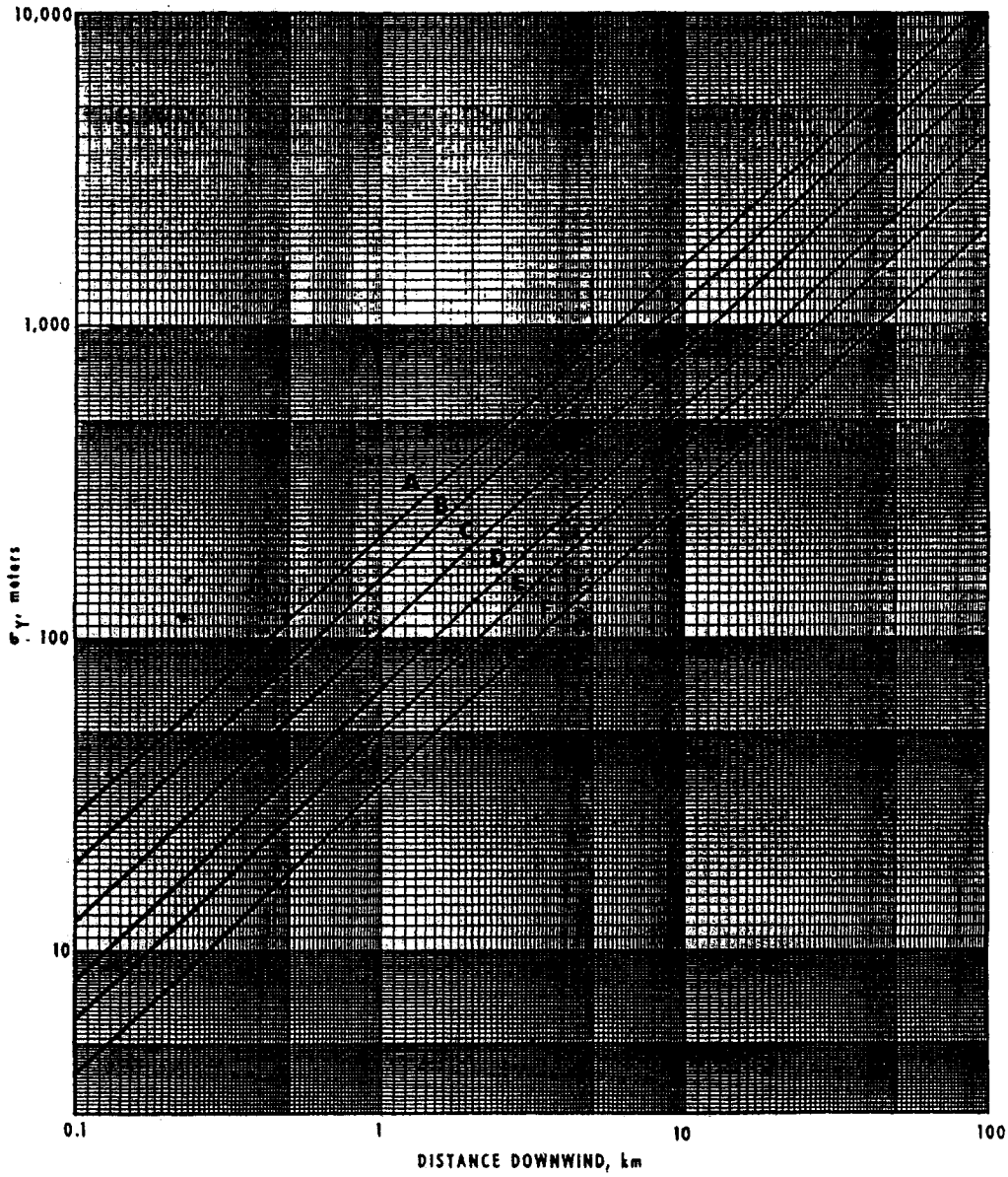

(a)

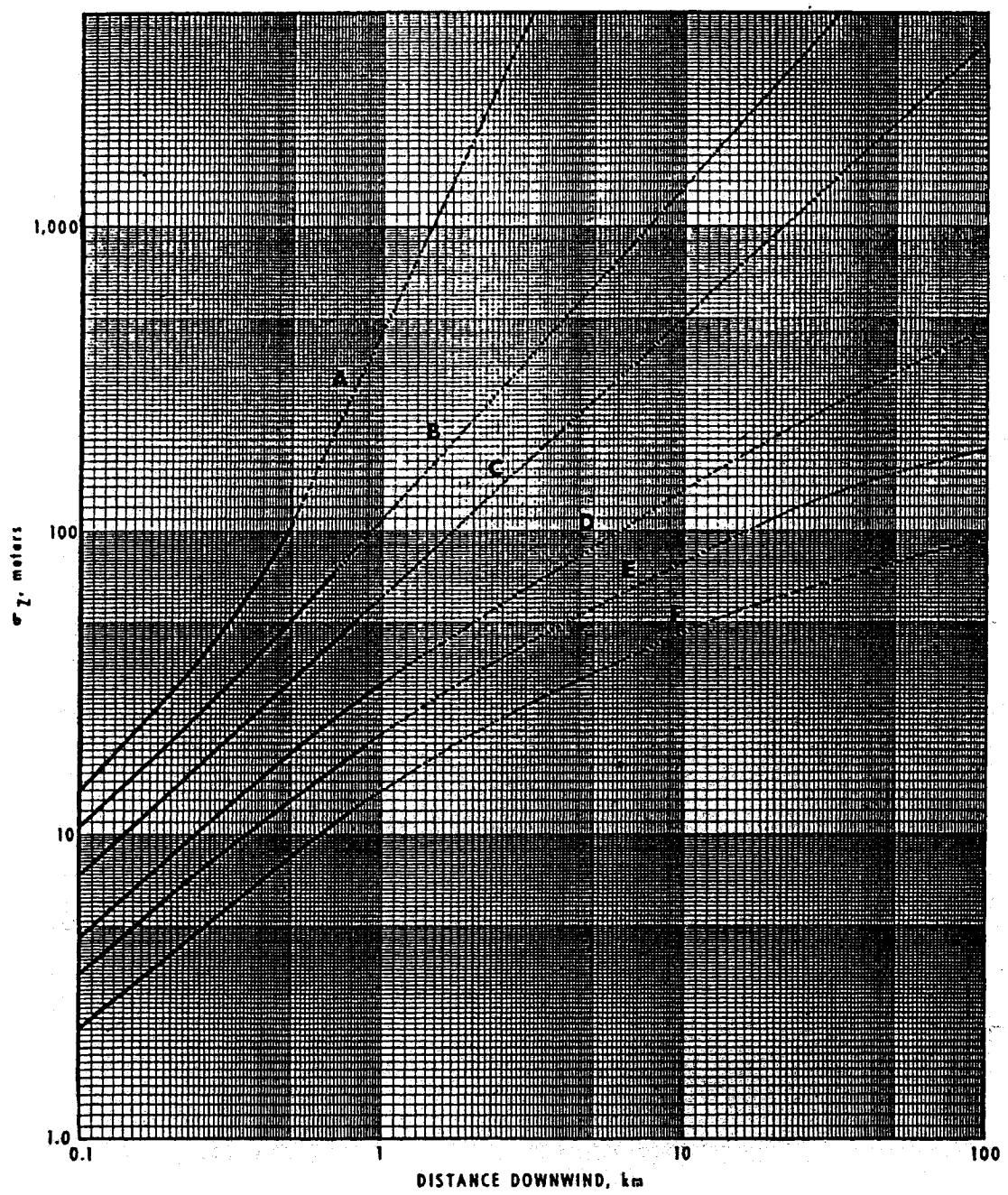

(b)

Figure B.1 Pasquill – Gifford Dispersion Parameters (a) Horizontal (b) Vertical (for neutral stability D condition, after Turner, 1994)

APPENDIX C

This part gives mesh resolution distributions for the case study of plume dispersion from an isolated stack. The definitions of the mesh grading schemes are shown in Fig. C. 1 and Fig. C. 2.

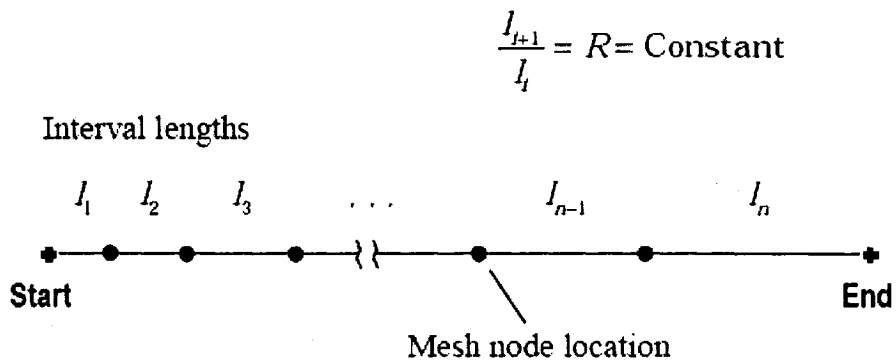

Figure C.1 Edge Mesh Grading Parameters for Single-sided Grading (Gambit 2.0)

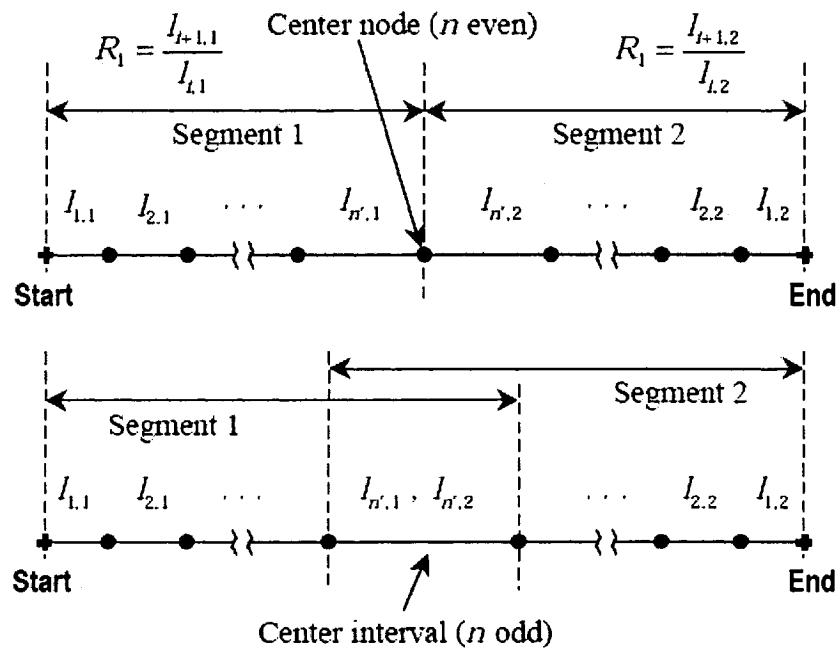

Figure C.2 Edge Mesh Grading Parameters for Double-sided Grading (Gambit 2.0)

Location	Length of the first interval (I_1)	Ratio (R)	Length of the last interval (I_n)
Upwind of the stack	5.1	1.02	24.6

(a)

Location	Length of the first interval (I_1)	Double ratio (R_1)	Length of the last interval (I_n)
Spaces between the stack center and the computational domain	4.5	1.02	7.8

(b)

Location	Length of the first interval (I_1)	Ratio (R)	Length of the last interval (I_n)
From ground to the top of the computational domain	0.4	1.08	15.1

(c)

Table C-1 Mesh Resolution Distribution for the Computational Domain along the (a) +x (b) +y (c) +z Direction (Stack Height: 16 m; Unit: Meter)

Note: Two edge mesh grading schemes are used here: (1) single-sided grading in which the mesh nodes are located along the edge such that the ratio of two succeeding interval lengths are constant (Fig. C.1) (2) double-sided grading in which the edge are divided into two segments and then the mesh nodes are located along each segment according to the ratio specified for each segment (Fig. C.2). If n is even, a mesh node is located at the center of grading. If n is odd, a mesh interval is located at the center of grading.

Location	Length of the first interval (I_1)	Ratio (R)	Length of the last interval (I_n)
Upwind of the stack	1.1	1.02	20.7

(a)

Location	Length of the first interval (I_1)	Double ratio (R_1)	Length of the last interval (I_n)
Spaces between the stack center and the computational domain	4.1	1.02	6.0

(b)

Location	Length of the first interval (I_1)	Ratio (R)	Length of the last interval (I_n)
From ground to the top of the computational domain	0.3	1.10	4.8

(c)

Table C-2 Mesh Resolution Distribution for the Computational Domain along the (a) +x (b) +y (c) +z Direction (Stack Height: 2 m; Unit: Meter)

APPENDIX D

This part gives mesh resolution distributions for the case study of plume dispersion from a flush stack mounted on the top of a cubic building.

Location	Length of the first interval (I_1)	Ratio (R) / double ratio (R_1)	Length of the last interval (I_n)
Upwind of the building	0.01	0.98	0.0037
Along the building	0.0027	1.02 (double)	0.003
Downwind of the building	0.0048	1.05	0.05

(a)

Location	Length of the first interval (I_1)	Ratio (R) / double ratio (R_1)	Length of the last interval (I_n)
Spaces between sides of the building and the computational domain	0.0032	1.08	0.03
Along the building	0.0027	1.02 (double)	0.003

(b)

Location	Length of the first interval (I_1)	Ratio (R) / double ratio (R_1)	Length of the last interval (I_n)
From ground to top of the building	0.0039	1.1 (double)	0.006
From top of the building to the end of the computational domain	0.0027	1.2	0.06

(c)

Table D-1 Mesh Resolution Distribution for the Computational Domain along the (a) +x (b) +y (c) +z Direction (Unit: Meter)

APPENDIX E

This part includes the mesh resolution distributions and the photo with upstream terrain for the case study of plume dispersion from a stack SL4 located over the top of a rectangular building. Also the coordinate locations for some receptors are listed.

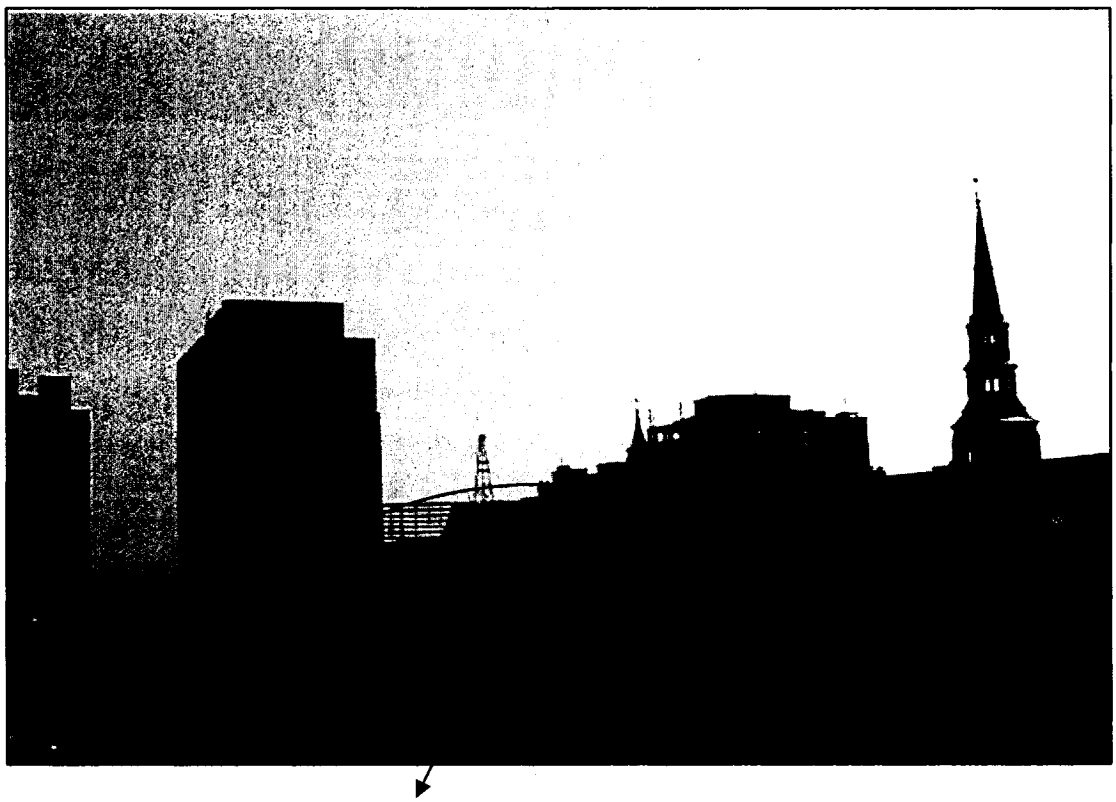

Figure E.1 Photos Showing Upstream Terrain for the BE Building (from southeast view) in the Present Study

Location	Length of the first interval (I_1)	Ratio (R) / double ratio (R_1)	Length of the last interval (I_n)
Upwind of the building	20	0.77	0.138
Along the building	0.144	1.15 (double)	3.58
Downwind of the building	0.0249	1.4	57.2

(a)

Location	Length of the first interval (I_1)	Ratio (R) / double ratio (R_1)	Length of the last interval (I_n)
Spaces between sides of the building and the computational domain	0.198	1.5	43
Along the building	0.162	1.1 (double)	2.33

(b)

Location	Length of the first interval (I_1)	Ratio (R) / double ratio (R_1)	Length of the last interval (I_n)
From ground to the top of the building	0.43	1.6 (double)	2.82
From top of the building to the top of the skylight structure	0.284	1.6 (double)	0.46
From top of the skylight structure to the top of the penthouse	0.2685	1.6	0.72
From top of the penthouse to the end of the computational domain	0.75	1.6	44

(c)

Table E-1 Mesh Resolution Distribution for the Computational Domain along the (a) +x (b) +y (c) +z Direction (Unit: Meter)

Name	R2	R15	R33	R21	R16	R18	S5	S4	S3	S1	R28	W1	W2	W3
x coordinate	8.0	8.6	9.6	9.6	21	38.0	16.0	16.0	16.0	16.0	21.0	0.5	1.1	2.3
y coordinate	-23	-5.0	20.5	12.5	-5.0	-5.0	-11	-5.4	12.5	19.0	13.5	-9.1	3.6	22.5
z coordinate	13.6	13.6	13.6	13.6	13.6	13.6	15.8	15.8	15.8	15.8	13.6	10.2	10.2	10.2

Table E-2 Receptor Coordinates for Case Study with Stack SL4 (Unit: Meter, Full Scale)

APPENDIX F

This appendix defines the velocity inlet boundary condition for each case study using the user defined function (UDF)

F1: Velocity Inlet Boundary Condition for an Isolated Stack with Stack Height 2 m and 16 m

```
#include "udf.h"
DEFINE_PROFILE(inlet_x_velocity, thread, index)
{
cell_t c;
real x[ND_ND]; real z;

begin_c_loop(c, thread)
{
C_CENTROID(x,c,thread);
z=x[2];
F_PROFILE(c, thread, index) = 5*pow(0.0036*z,0.14);
}
end_c_loop(c, thread)
}

DEFINE_PROFILE(inlet_intensity, thread, index)
{
cell_t c;
real x[ND_ND];
real z;

begin_c_loop(c, thread)
{
C_CENTROID(x,c,thread);
z=x[2];
F_PROFILE(c, thread, index) = 0.2976/z;
}
end_c_loop(c, thread)
}
```

F2: Velocity Inlet Boundary Condition for Airflow around an Isolated Cubic Building

```
#include "udf.h"
DEFINE_PROFILE(inlet_x_velocity, thread, index)
{
cell_t c;
real x[ND_ND]; real z;

begin_c_loop(c, thread)
{
C_CENTROID(x,c,thread);
z=x[2];
F_PROFILE(c, thread, index) = 4.73*pow(z,0.13);
}
end_c_loop(c, thread)
}



DEFINE_PROFILE(inlet_k, thread, index)
{
cell_t c;
real x[ND_ND]; real z;

begin_c_loop(c, thread)
{
C_CENTROID(x,c,thread);
z=x[2];
F_PROFILE(c, thread, index) = -114.92*pow(z,4.0)+103.85*pow(z,3.0)-
28.538*pow(z,2.0)+1.6857*pow(z,1.0)+0.2135;
}
end_c_loop(c, thread)
}


DEFINE_PROFILE(inlet_eppisilon, thread, index)
{
cell_t c;
real x[ND_ND];
real z;

begin_c_loop(c, thread)
{
C_CENTROID(x,c,thread);
z=x[2];
F_PROFILE(c, thread, index) = 0.026/z;
}
end_c_loop(c, thread)
}
```

F3: Velocity Inlet Boundary Condition for Airflow around an Isolated Rectangular Building

```
#include "udf.h"
DEFINE_PROFILE(inlet_x_velocity, thread, index)
{
cell_t c;
real x[ND_ND];
real z;

begin_c_loop(c, thread)
{
C_CENTROID(x,c,thread);
z=x[2];
F_PROFILE(c, thread, index) = 87.2*pow(z*0.0042,0.32);
}
end_c_loop(c, thread)
}

DEFINE_PROFILE(inlet_k, thread, index)
{
cell_t c;
real x[ND_ND];
real z;

begin_c_loop(c, thread)
{
C_CENTROID(x,c,thread);
z=x[2];
F_PROFILE(c, thread, index) = 3990.1*pow(z,6.0)-
7642.4*pow(z,5.0)+5653.4*pow(z,4.0)-
2046.6*pow(z,3.0)+382.28*pow(z,2.0)-41.028*pow(z,1.0)+5.213;
}
end_c_loop(c, thread)
}

DEFINE_PROFILE(inlet_eppisilon, thread, index)
{
cell_t c;
real x[ND_ND]; real z;

begin_c_loop(c, thread)
{
C_CENTROID(x,c,thread);
z=x[2];
F_PROFILE(c, thread, index) = 0.1857*pow(z,-0.9844);
}
end_c_loop(c, thread)
}
```